INVESTIGATION OF GEOMETRIC AND THERMAL SCALING EFFECTS ON A SIMULATED TURBINE VANE LEADING EDGE MODEL

THESIS

James G. Tewaheftewa, Captain, USAF

AFIT-ENY-MS-18-M-297

DEPARTMENT OF THE AIR FORCE
AIR UNIVERSITY

AIR FORCE INSTITUTE OF TECHNOLOGY

Wright-Patterson Air Force Base, Ohio

AFIT-ENY-MS-18-M-297

INVESTIGATION OF GEOMETRIC AND THERMAL SCALING EFFECTS ON A SIMULATED TURBINE VANE LEADING EDGE MODEL

THESIS

Presented to the Faculty

Department of Aeronautics and Astronautics

Graduate School of Engineering and Management

Air Force Institute of Technology

Air University

Air Education and Training Command

In Partial Fulfillment of the Requirements for the

Degree of Master of Science in Aeronautical Engineering

James G. Tewaheftewa, BS

Captain, USAF

March 2018

AFIT-ENY-MS-18-M-297

INVESTIGATION OF GEOMETRIC AND THERMAL SCALING EFFECTS ON A SIMULATED TURBINE VANE LEADING EDGE MODEL

James G. Tewaheftewa, BS

Captain, USAF

Committee Membership:

Dr. Marc. D. Polanka
Chair

Dr. Mark F. Reeder
Member

Lt Col James. L. Rutledge, PhD
Member

AFIT-ENY-MS-18-M-297

Abstract

Film cooling is still a bustling research topic, especially with burgeoning manufacturing techniques on the horizon that will open the design space. However, despite the number of years that have gone into gas turbine design and research, evaluating cooling performance on components still presents challenges. This task becomes especially difficult and dangerous if trying to do so in realistic engine conditions. Therefore, the majority of film cooling research is performed at conditions far from realistic engine conditions, often using materials that would never hold up to turbine inlet temperature, and scaled to predict results at engine conditions. Previous film cooling investigations at the Air Force Institute of Technology have been conducted on both large and small scale experimental rigs. This thesis sought to investigate the effect that the geometric size differences had an overall effectiveness. To enable a comparison, the small scale rig performed experiments on a $1/9^{th}$ scaled leading edge model. Slight differences in the coolant delivery method highlighted the importance of internal cooling and caused the results to match poorly. Additionally, this thesis also continued to investigate the relative importance of nondimensional parameters that relate film cooling performance within different temperature regimes. Tests were conducted to understand how temperature, Reynolds number, blowing ratio, and internal cooling configuration impacted the overall effectiveness. Thermal measurements were made through IR thermography on the Inconel 718 semi-cylinder leading edge model to support the research objectives.

Acknowledgments

I would like to thank Carl Pickl and Nathan Clark for all of their assistance with designing, building, operating, and the list goes on. Your help was truly invaluable. I would also like to thank Lieutenant Vorgert and Lieutenant Bryant for putting up with all my questions about their work. Additionally, I'd like to also thank Lieutenant Bryant for collecting data to support my work. Thank you to Dr. Polanka for your guidance, support, and patience as my advisor. I'd also like to thank Lt Col Rutledge and Dr. Reeder for the guidance inside of the classroom and for your valuable insights that improved this thesis further. Thanks to both the AFIT and AFRL model shops for all their help with getting the new rig built and running. Thank you to Mike, Keith, Jaime, and Josh for your help around the lab and for fixing things when they broke. Thank you to my lab mates for all your help and friendship. Thank you to my family and all my friends for your support. Finally, thank you to B for all you do for me.

James G. Tewaheftewa

Nomenclature

A	=	area
b	=	slot width
B	=	calibration coefficient
Bi	=	Biot number
c	=	constant
d	=	hole diameter
D	=	diameter
DR	=	density ratio
F	=	calibration constant
g	=	gap distance
h	=	convective heat transfer coefficient
H	=	gap height
I	=	momentum flux ratio
$\mathcal{J}$	=	radiative intensity
k	=	thermal conductivity
L	=	length
$\dot{m}$	=	mass flow rate
M	=	mass flux ratio
Nu	=	Nusselt number
$NHFR$	=	net heat flux reduction
P	=	pressure or pitch
Pr	=	Prandtl number
q''	=	heat flux
R	=	gas constant or calibration constant
Re	=	Reynolds number
S	=	place holder
t	=	thickness
T	=	temperature
U	=	velocity
V	=	velocity
VR	=	velocity ratio
W	=	width
x	=	length scale or axial position
Z	=	distance from curved surface

Subscripts

0	=	without film cooling
aw	=	adiabatic wall
b	=	blackbody
c	=	coolant
ce	=	coolant hole exit
ci	=	coolant hole entrance
cond	=	conduction
conv	=	convection
ext	=	external
f	=	with film cooling
g	=	gas or real body behavior
h	=	coolant hole
imp	=	impingement plate
int	=	internal
LE	=	leading edge
p	=	plenum
r	=	relative nozzle
rad	=	radiation
TS	=	test section
w	=	wall
∞	=	freestream property

Superscripts

$\overline{(...)}$	=	spanwise or streamwise average
$\overline{\overline{(...)}}$	=	area average

Greek

α_R	=	thermal coefficient of resistivity
β	=	angular spacing
γ	=	injection angle
ε	=	emissivity
η	=	adiabatic (film cooling) effectiveness
θ	=	nondimensional wall temperature
λ	=	wavelength

μ	=	dynamic viscosity
ρ	=	density
ϕ	=	overall effectiveness
χ	=	coolant warming factor

Table of Contents

Page

List of Figures

Page

List of Tables

Page

INVESTIGATION OF GEOMETRIC AND THERMAL SCALING EFFECTS ON A SIMULATED TURBINE VANE LEADING EDGE MODEL

1. Introduction

With ever increasing power and efficiency demands on gas turbine engines, there is also increasing demand for improved and efficient cooling methods driven by rising hot section temperatures. To that end, component designers strive to manage time and resources to create the most cost and operationally effective solutions. Generally, this process is long and iterative. Improvement in the design and testing phase could lead to large cost savings or performance gains. This investigation sought to improve the capability of the Air Force Institute of Technology's (AFIT) Film Cooling Rig's (FCR) to test high fidelity models and reduce the influence of the lab environment has on heat transfer investigations.

1.1. Film Cooling Motivation

While jet engines have consistently progressed for the better half of a century, there remains a need for better and more efficient designs. An enabling technology that has helped propulsion systems take a large leap forward was the development of component cooling. The first breakthrough for this technology was the use of internal cooling schemes around the 1960s that allowed turbine components to operate in gas temperatures higher than that of the melting points of their constituent materials [1]. Cooling schemes evolved to incorporate film cooling to address heating issues directly by protecting turbine components externally from the hot freestream gases expelled by the combustor. Since the genesis of these cooling techniques, the benefits of cooling have been well documented; included are allowances for

higher temperature combustion, increased efficiencies, and prolonged turbine component life [1,2].

Although cooling technology has the ability to greatly enhance component performance and survivability, some designs could prove to be detrimental (i.e. producing large thermal gradients leading to enhanced thermal strain). Therefore, it is important to have the means to accurately and quickly assess the performance of a given cooling scheme. With this ability, designers have the capability to examine a large variety of schemes and to confidently choose the best performing scheme for use in actual components

1.2. Overall Objectives

There were three overall objectives in this investigation. The first objective was to redesign the FCR to enable a geometric scaling investigation with an existing large scale rig. The second overall objective was to continue investigating the impact of different nondimensional parameters on the scaling of film cooling effectiveness. The third overall objective was to specifically examine the thermal scaling behavior of Inconel 718, a representaive gas turbine component material.

1.2.1. Geometric Scaling Investigation

There are advantages to large scale testing such as increased safety, model manufacturing benefits, and instrumentation advantages. However, there are still concerns with how accurate results produced on a large scale matched Biot number model are to real components. With the two distinctly different scaled setups at AFIT, there is an opportunity to investigate how well film cooling results compare between the two setups. Despite the two

setups co-existing for a number of years, any comparisons between the results of the rigs were overshadowed by the fact the setups differed significantly.

To support future comparisons of data between the two rigs, work was begun to make the necessary changes on the engine scale rig to better match the experimental setup of the large scale rig. This included the integration of a scaled version of the semi-cylinder leading edge model used by the large scale rig, which forced the redesign of the test section to include a bypass path that allowed part of the freestream to pass underneath the model. In the process of the rig design, an understanding that testing at the same conditions of the large scale rig would be difficult due to a mass flow limitation. In response to this issue, changes were made to the support equipment to enable an increased freestream flow capacity. Despite increasing the flow capacity, the rig's capability to match the freestream conditions still fell short. To enable a comparison of results, the large scale rig performed tests at conditions that the small scale could reach.

1.2.2. Impact of Nondimensional Parameters on Overall Effectiveness

With the redesigned FCR, work on investigating the relative impact that nondimensional parameters have on overall effectiveness was continued. Changes from the first objective increased the flow capacity of the rig enabling higher Reynolds numbers to be achieved; however, this change also prohibited the use of the well-stirred reactor, decreasing the maximum achievable freestream temperature. Tests were performed using electric heaters to generate two freestream. Specifically, tests were designed to understand the impact the freestream Reynolds number and the blowing ratio on the overall effectiveness.

Additionally, the impact of the freestream temperature regime and the internal cooling configuration were investigated.

1.2.3. Investigation of Thermal Scaling Capability of Inconel 718

Recent thermal scaling research using Inconel 718 [3] showed great promise that results obtained in one temperature regime could be used to predict the performance of the same model in another temperature regime. However, the study was limited in scope and could use additional data to paint a better picture. If true, experiments could be conducted safely at laboratory conditions and produce results that are applicable at dangerous engine conditions. Additionally, this could significantly cut research costs and time leading to increased savings and performance. To further understanding of the results produced by Stewart and Dyson [3], this investigation sought to use data collected on an Inconel 718 leading edge model to perform a similar analysis.

1.3. Thesis Chapter Layout

To accomplish these thesis goals, Chapter 2 explores the literature related topics such as film cooling performance and measurement ofconjugate heat transfer. Chapter 3 contains the experimental setup used to accomplish these research objectives. Chapter 4 outlines the results of the work accomplished. First, the results of the geometric scaling work accomplished is examined, including a discussion on how the freestream flow conditions were affected and another discussion on the ability to set the stagnation point. This is followed by the results of the small scale testing. This includes examining the effect of tests conducted in different temperature regimes, the effect of the Reynolds number, and the effect of internal cooling configuration.

2. Literature Review

A history of desire for increased efficiency and power output has continued to push the limits of gas turbine engine technology. For about a half century, improvements in the engine cycle have led to hotter combustions which stresses the ability of the engine's components to operate reliably, and even to survive becomes difficult. This continuous cycle of improvement has spurred researchers to investigate methods which provide protection for hot gas path components. Historically, internal cooling methods comprised the bulk of the research and became the primary means for cooling components, improving performance and reliability until combustor technology improved further. However, improved combustion sections led to higher turbine inlet temperatures leading researches to seek additional means for cooling. Eventually, researchers would turn to protecting hot gas path components more directly through the injection of "colder" gas that would provide a buffer between the hot mainstream gasses and the component's wall. Though this idea is simplistic in description, proper execution of the technique is quite complex. There are a myriad of factors that affect film cooling performance and a great number of ways to provide that cooling.

The research performed at the Air Force Institute of Technology's (AFIT) Film Cooling Rig (FCR) seeks to accurately and reliably investigate film cooling performance of various schemes. Previous research conducted in the FCR includes reactive film cooling experiments; investigation of several film cooling hole configurations and shapes; and most recently, an experiment to investigate the scaling of film cooling performance between ambient and near engine temperatures. The focus of the current research is to improve the reliability of film cooling performance measurements in the FCR in addition to implementing the coolant delivery system used by a sister project.

The purpose of this chapter is to provide background on film cooling basics (Section 2.1), explain how cooling scheme performance is quantified (Section 2.2), discuss important characteristic parameters used in film cooling experiments (Section 2.3), explore how different conditions affect the performance of a scheme (Section 2.4), and discuss the measurement techniques used in the current research (Section 2.5).

2.1. Film Cooling Basics

Over the last half-century, gas turbine engine technology has improved immensely and one of the major contributors for this improvement is the advent of cooling technology. In gas turbine design, the aim has always been to increase cycle efficiencies, increase jet performance, and improve durability of components reducing the likelihood of catastrophic failure. According to a 2013 report by the US Department of Energy's National Energy Technology Laboratory [4], the turbine inlet temperature of future class engines is expected to be in excess of 1700 ˚C, much higher than the melting points of most metals. Additionally, if a component is able to withstand these temperatures, the component is still susceptible to severe thermal stresses due to large non-uniformities in temperature that exist in the part. Thus, there is a clear need for component cooling that protects the component from melting and reducing the thermal gradients that would exist otherwise.

The purpose of film cooling is to provide a "cool" film of gas over a component in order to reduce the heat transferred to the component from the hot freestream gases. In situations without film cooling, the heat flux into the component is calculated by Newton's Law of cooling (Equation 1):

$$q"_0 = h_0(T_\infty - T_w) \quad (1)$$

where h_0 is the convective heat transfer coefficient without film cooling, T_∞ is the freestream temperature, and T_w is the component's wall temperature. In this situation, h_0 is a function of geometry and the freestream flowfield properties. In the presence of film cooling, however, determining h becomes much more complicated due to the interaction of the coolant jet and freestream flow.

To provide coolant to hot gas path components, engine designers use bleed air from the compressor. A general rule of thumb is that about 20-30% of the total flow through the engine will be used for component cooling [1]. From a combustion perspective, this is a significant amount of "unused" air that would otherwise be used for combustion. Coupled with the fact that it takes work to compress the air that seemingly goes unused, component cooling can appear to be an energy sink. However, Han et al. [5] suggest that reducing a component's temperature by 30 K can increase part life by a factor of two. These factors combined create a design space for engine designers to work within where component durability and work required to provide coolant must be balanced.

Figure 1 shows a simplified example of a film cooling scenario with an external freestream flow and coolant flow that travels through the component and exits at discrete holes in component's wall. When film cooling is present, like shown in Figure 1, there are three temperatures of concern: the temperature of the freestream gas, T_g; the component's wall, T_w; and the coolant, T_c. Although the heat flux with film cooling, q_f'', can still be modeled with Newton's Law of cooling (Equation 2), it is no longer directly a function of the difference of the freestream temperature and the wall temperature like is the case without cooling. Instead, the difference in the adiabatic wall temperature, T_{aw}, and the wall temperature is used. In film cooling, the adiabatic wall temperature can be described as the

temperature of the fluid immediately above the component's wall and is the driving temperature for convective heat transfer in this scenario. Additionally, due to the complex interactions of the coolant jet and the freestream, the convective heat transfer coefficient is no longer just dependent on the freestream properties and specimen's geometry. Thus, the external convective heat flux is calculated using the convective heat transfer coefficient due to film cooling, h_f.

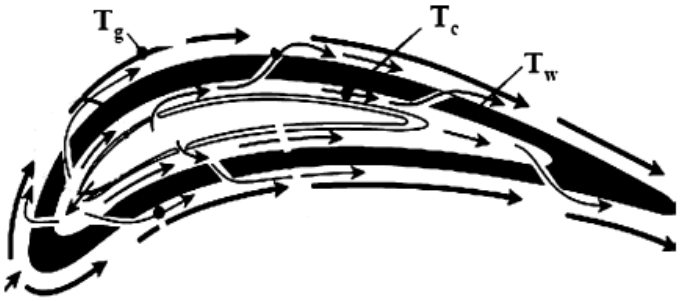

Figure 1. Film Cooled Turbine Airfoil adapted from Bogard and Thole. [1]

$$q''_f = h_f(T_{aw} - T_w) \tag{2}$$

2.2. Performance Metrics

Ultimately, there must be a way to quantify the performance of a cooling scheme. In contemporary film cooling experiments, there exist multiple metrics to measure performance, however, this section will focus on two primary metrics: adiabatic effectiveness and overall effectiveness. In general, adiabatic effectiveness, or film effectiveness, only quantifies the cooling performance due to film cooling while overall effectiveness quantifies the cooling performance of the whole cooling scheme implemented, including external cooling due to film cooling as well as internal cooling. More discussion to follow on each metric. Furthermore, there will be additional discussions on two related

differential measures, net heat flux reduction and delta phi. Delta phi will be used during this investigation.

2.2.1. Adiabatic Effectiveness

Adiabatic effectiveness (Equation 3) is a tool used to understand the individual effects of external cooling configurations. This parameter quantifies the local cooling effectiveness of a film cooling scheme in the special case of an adiabatic (non-conducting) wall. That is, it is a measure of the difference of the adiabatic wall temperature, T_{aw}, and the freestream temperature, T_{∞}, as a result of the implemented film cooling scheme. Additionally, the difference between the two temperatures is normalized by the difference in the freestream temperature and the coolant hole exit temperature, T_{ce}, which bounds the value of adiabatic effectiveness between 0 and 1.

$$\eta = \frac{T_{\infty} - T_{aw}}{T_{\infty} - T_{ce}} \tag{3}$$

In practice, however, no model can expect to have truly adiabatic surfaces. To approximate adiabatic effectiveness on a given geometry, the use of very low thermal conductivity material for construction of test articles is often employed. [6–8] With adequately small thermal conductivity, the resulting surface temperature distribution on a test article is deemed close to the truly adiabatic (non-conducting) case. Although conduction of heat through low conductivity models is reduced, conduction still occurs which must be taken into account. Williams et al. [9] applied a conduction correction to their results whereby the effect of film cooling was isolated by subtracting out other mechanisms of cooling. This was accomplished by measuring the resulting surface temperature distributions when their film cooling holes were blocked while coolant was flowed through their model. Although they

did not report conduction correction values, Dees et al. [7] performed a similar correction process that resulted in typical conduction correction values of 5 to 8% of the total heat flux which resulted in an estimated uncertainty of ±0.02 for η.

2.2.2. Overall Effectiveness

While useful for measuring the effectiveness due to external coolant flow, adiabatic film cooling effectiveness does not accurately characterize the performance of cooling configurations on real, metallic components. This is because real components have other paths of cooling (and heating) available, including through conduction and internal convection as seen in Figure 2. Equation 4 represents one-dimensional conductive heat flux through a component where k_w is the thermal conductivity of the component's wall and dT/dx is the temperature gradient in the part. Equation 5 represents the convective heat flux on the internal surface of a component where h_i is the internal convective heat transfer coefficient, T_{w2} is the internal surface wall temperature, and T_c is the coolant temperature.

$$q''_{cond} = -k_w \frac{dT}{dx} \tag{4}$$

$$q''_{conv,int} = h_i(T_{w2} - T_c) \tag{5}$$

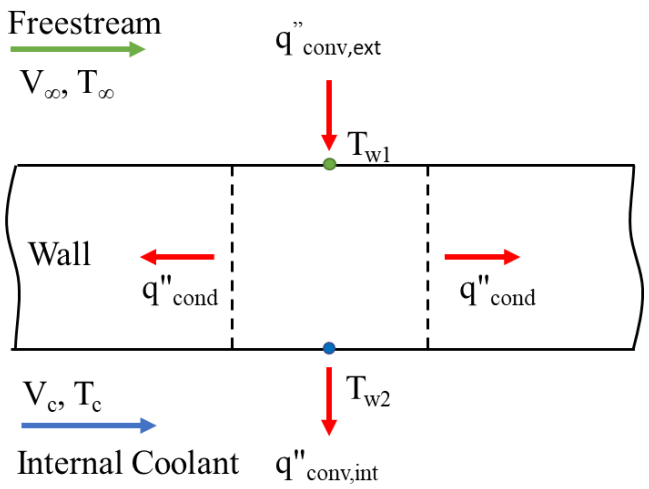

Figure 2. Basic modes of heat transfer in component wall including external/internal convection and conduction.

To characterize the performance of a cooling configuration on a real turbomachinery component, the overall cooling effectiveness, ϕ, is a preferred nondimensionalized parameter (Equation 6). The overall cooling effectiveness, which has a similar form to that of adiabatic effectiveness, is comprised of the component's wall temperature, T_w; the freestream temperature, T_∞; and the internal coolant temperature, T_{ci}. Because hot gas path components are typically manufactured out of metals with relatively high thermal conductivities, an adiabatic wall condition does not exist and the resulting wall temperature when the part is heated is due to conjugate heat transfer. Additionally, the difference in the freestream temperature and the internal coolant temperature, rather than the external coolant temperature, is used to normalize the difference between the metal wall and freestream temperatures.

$$\phi = \frac{T_\infty - T_w}{T_\infty - T_{ci}} \tag{6}$$

Rutledge et al. [10] showed the development of another way to represent the overall effectiveness in a way that enables the relevant factors to be understood. This alternative

form of the overall cooling effectiveness, shown in Equation 7, introduces three additional terms: the coolant warming factor (Equation 8), χ; the Biot number (Equation 9), Bi; and the ratio of external to internal heat transfer coefficients, h_f/h_i. In this new form, the thermodynamic parameters that are important to scaling overall effectiveness results obtained through experimentation are clear.

$$\phi = \frac{T_\infty - T_w}{T_\infty - T_{ci}} = \frac{\chi\eta\left(Bi + \frac{h_f}{h_i}\right) + 1}{\frac{h_f}{h_i} + Bi + 1} \tag{7}$$

$$\chi = \frac{T_\infty - T_{ce}}{T_\infty - T_{ci}} \tag{8}$$

$$Bi = \frac{h_f L}{k_w} \tag{9}$$

The coolant warming factor represents the change in the coolant temperature as it travels through the component to the exit of the film cooling hole. The coolant warming factor is calculated using the temperature of the freestream; the temperature of the coolant as it exits the coolant hole, T_{ce}; and the temperature of the coolant inside of the component, T_{ci}. In a study evaluating overall effectiveness on the leading edge region of turbine vane model, Bryant [11] further decomposed χ in an attempt to better understand where coolant is actually warmed as it traveled through her model. The resulting components were the coolant plenum warming factor, χ_p, and the coolant hole warming factor, χ_h, shown in Equations 10 and 11, respectively.

$$\chi_p = \frac{T_\infty - T_{ci}}{T_\infty - T_{cp}} \tag{10}$$

$$\chi_h = \frac{T_\infty - T_{ce}}{T_\infty - T_{ci}} \tag{11}$$

χ_p quantifies the relative temperature increases as the coolant passes through the plenum to the entrance of the film cooling hole. The relevant temperatures involved are the coolant temperature in the plenum, T_{cp}; the coolant temperature at the entrance of the coolant hole, T_{ci} (different than temperature in Equation 8); and the freestream temperature. χ_h quantifies the temperature increase as the coolant passes through the coolant hole. The relevant temperatures involved in this parameter are the coolant temperature at the entrance of the coolant hole; the coolant temperature at the exit of the hole, T_{ce}; and the freestream temperature. The closer to unity that the parameters are means the less warming that occurs. Another property of the subcomponents is that when multiplied together, the product equals the warming factor as shown in Equation 12. Bryant [11] investigated the warming factor at three blowing ratios (M = 0.25, 0.5, and 0.9) on a leading edge model where freestream was ingested in two of the cases. In the worst case of ingestion (M = 0.25), the plenum warming factor was 0.63 and the hole warming factor was 0.66 indicating that the coolant warmed most in the plenum. In the case that experienced no ingestion (M = 0.9), the plenum warming factor was 0.95 and the hole warming factor was 0.85 indicating that coolant was warmed most while traveling through the coolant hole.

$$\chi = \chi_p \chi_h \tag{12}$$

Continuing the examination of the factors relevant to overall effectiveness, the ratio heat transfer coefficients is dependent on both the internal and external Reynolds and Prandtl numbers through the Nusselt numbers correlations, which in turn are generally functions of geometry and flowfield properties [12]. With that in mind, experimental models are usually

designed such that existing correlations can be used to aid in prediction of the heat transfer coefficients or else the values must be experimentally determined.

In experimentation, the Biot number is a nondimensional parameter that relates the conductive thermal resistance to the convective thermal resistance where h_f is the external convective heat transfer coefficient, L is a reference length, and k_w is still the thermal conductivity of the metal wall. *Bi* is important because it scales the relative importance of convection and conduction in a given scenario. For instance, if *Bi* is determined to be much less than unity, the thermal gradients in the wall will be small at steady state conditions due to the low conductive resistance of the wall [13]. According to Lawson et al. [4], typical engine *Bi* ranges from as low as 0.3 to as high as 0.6 and depends on the scale, material composition, and operating conditions of the component.

The advantage of using the ϕ formulation provided by Rutledge et al. [10] is that when all the parameters just discussed are matched between lab and engine conditions, the resulting ϕ measured at lab conditions will be the same at engine conditions. This fact is powerful, and as Williams et al. [9] highlights, this allows experimenters to use data obtained at scaled conditions to determine the temperature distribution on the component at actual conditions, which enables identification of any potential "hot spots". This ability could be extremely useful during the design and testing phase of new turbomachinery components. In recent literature, overall film cooling effectiveness has seen increased usage to evaluate prospective hot gas path component cooling configurations [3,6,7,9,14–17]. According to Polanka et al. [12], typical values of ϕ range from 0.4 to 0.7 or higher.

In a recent conjugate heat transfer investigation, Stewart and Dyson [3] examined the scaling behavior of thermal conductivities of air and Inconel 718, a nickel alloy, between

experimental and engine temperatures and how they affect heat transfer results of matched *Bi* experiments. This work was motivated by the results of an analytical examination that they performed where they determined that matching *Bi* and *Nu* (discussed further in Section 2.3) between two conditions depends on matching the ratio of the thermal conductivity of air to the thermal conductivity of the model's wall, k_{air}/k_{wall}. They first performed a hypothetical analysis where they determined how the thermal conductivities of the freestream and the Inconel 718 wall varied between two different conditions, engine conditions and experimental rig conditions. The engine conditions were presumed to be T_∞ = 2000K and T_c = 1000K and when assuming ϕ = 0.6 resulted in T_w = 1400K. The hypothetical rig conditions were presumed to be T_∞ = 500K and T_c = 250K and, again, when assuming ϕ = 0.6 resulted in T_w = 350K. Evaluating the thermal conductivities of the freestream and the wall at each of these temperatures, they found that the thermal conductivity of the freestream air scaled by a factor of 2.61 and the thermal conductivity of the Inconel 718 wall scaled by a factor of 2.37 from the rig to the engine conditions. Therefore, according to their previous analytical work, this discrepancy in scaling of the thermal conductivities between the two conditions would result in a mismatch of *Bi* by around 10% between rig and engine conditions.

Next, lab experiments were performed at two different conditions, "cold" and "hot", to try to confirm the results of the hypothetical analysis. Stewart and Dyson [3] presented data that showed the two conditions produced data that differed around 0.025 in ϕ, which was within their experimental uncertainty, while the Biot numbers were matched within 11-12%. Assuming the factors in an equation equivalent to Equation 7 were constant, except the Biot number, they propagated this error through the overall effectiveness equation and determined that the resulting departure in the value of ϕ would be 0.005, which was a much

smaller value than they could resolve with their experimental setup. Despite the differences in overall effectiveness, they felt that the differences were small enough to consider Inconel 718 a good candidate for conjugate heat transfer experiments that could provide thermally scaled results with a relatively degree of uncertainty.

2.2.3. Additional Performance Metrics

As previously mentioned, the objective of film cooling is to reduce heat flux from the freestream to the surface. To understand if a film cooling scheme is beneficial, it may be useful to compare heat flux results produced by a film cooling scheme (Equation 2) against the heat flux obtained when no film cooling is present (Equation 1). The Net Heat Flux Reduction parameter, or *NHFR*, combines $q_f^{"}$ and $q_0^{"}$ as shown in Equation 13. which allows users to easily determine whether a film cooling scheme is beneficial. If the scheme positively impacts cooling, *NHFR* will have a value greater than 0. If the scheme is detrimental, *NHFR* will have a value less than 0.

$$NHFR = 1 - \frac{q_f^{"}}{q_0^{"}} = 1 - \frac{h_f}{h_0}\left(1 - \frac{\eta}{1-\theta_w}\right) \tag{13}$$

Additionally, Greiner et al. [18] showed that *NHFR* could be rewritten in terms of η and the ratio of convective heat transfer coefficients with and without film cooling, h_f/h_0. This form of the equation also uses the nondimensionalized wall temperature, θ_w, defined in Equation 14 as:

$$\theta_w = \frac{T_w - T_{c,e}}{T_\infty - T_{c,e}} \tag{14}$$

Further, Polanka [19] showed that at near ambient temperatures the $1-\theta_w$ term can replaced with ϕ due to the fact that the expected coolant warming is small in this temperature regime (i.e. $T_{c,i} \approx T_{c,e}$). This form is most common in the literature; however, it must be recognized that the $1-\theta_w$ term must remain when high coolant warming is experienced.

Another alternative performance measuring method found in the literature is the delta phi method developed by Rutledge et al. [10]. As described by Rutledge et al., this method can be used as a method to differentiate the impact of two different cooling configurations on the resulting wall temperature, assuming the same freestream and coolant temperatures. Employing this method still requires first quantifying the overall effectiveness produced by the cooling schemes in question as described in Section 2.2.2. Once this is accomplished, the resulting overall effectiveness distributions may be subtracted from one another to determine $\Delta\phi$ as shown in Equation 15 where the different cooling schemes are denoted by subscripts *a* and *b*. This method offers a way to predict the nondimensional reduction or increase in surface temperature when changing from one scheme to another. This parameter is similar to NHFR except that it more directly quantifies the impact of changing film schemes has on the resulting external wall temperature. Even more important, it is conceivable that this method could be used to compare many film cooling schemes to aid in determining the best cooling configuration for a given component. Rutledge et al.[10] used the method to evaluate film cooling performance on a leading edge model. By applying the method, they determined the optimum mass flux ratio to use with their model and predicted a decrease in external wall temperature of approximately 62 K when compared to another cooling configuration.

$$\Delta\phi = \phi_b - \phi_a \tag{15}$$

2.3. Characteristic Parameters

To understand component cooling, it is important to understand the various parameters relevant to the film cooling process. The first set of parameters characterize the fluidics and the thermodynamics of the problem being examined. The most basic and commonly used nondimensional parameters in any heat transfer problem involving fluid flow are the Reynolds number, *Re*, and the Prandtl number, Pr, shown in Equations 16 and 17, respectively. These parameters ensure that the nondimensional Momentum and Energy equations are satisfied guaranteeing like conditions between independent observations for a given experimental setup. A common goal in many film cooling experiments is to collect data in less strenuous laboratory conditions that would translate to engine conditions, otherwise known as scaling of results. Therefore, matching the experimental Reynolds numbers to the expected engine conditions Reynolds numbers is important to ensure flow field conditions are comparable.

$$Re = \frac{\rho V L}{\mu} \tag{16}$$

$$Pr = \frac{\nu}{\alpha} \tag{17}$$

Greiner et al. [20] performed a numerical study examining the effect of several nondimensional parameters, including both the freestream and coolant Reynolds numbers, Re_∞ and Re_c respectively, on the scaling of film cooling performance from ambient conditions to engine conditions. In the study, baseline results were obtained at engine conditions and then selected parameters were matched at ambient conditions. The resulting film cooling performance was then compared against the baseline. Due to non-linear scaling of the fluid properties with respect to temperature, this resulted in unmatched parameters in

all of the ambient simulations. Through this analysis, it was confirmed that both parameters, Re_∞ and Re_c, are important to producing scalable results. Specifically, it was found that the cases where these parameters matched produced the closest results to the baseline. Further examination also showed that matching Re_c produced a better match to cooling performance at engine temperatures vice matching Re_∞. However, they found that performing two experiments while matching Re_∞ or Re_c and averaging their results for adiabatic effectiveness increased the accuracy of the scaled results.

It is also important that thermodynamic nondimensional parameters are matched. This fact was very apparent in the results obtained by Greiner et al. [20] when the freestream and coolant Prandtl numbers were allowed to go unmatched with the baseline case. Ultimately, these particular cases resulted in the worst case of scaling between the low and high temperature solutions confirming that matching the Prandtl number is important to scaling. The study found that a change of Pr from 0.7 to 2.4 was indicative of changing from gas to liquid flows and resulted in errors in η of up to 0.27. Fortunately for real world experiments conducted with gasses, Pr is unlikely to vary significantly over the temperature range of interest.

Another important nondimensional heat transfer parameter is the Nusselt number, Nu, shown in Equation 18. The Nusselt number is the ratio of convection to pure conduction heat transfer:

$$Nu = \frac{hL}{k_f} \tag{18}$$

where h is the convection heat transfer coefficient at the surface, L is a reference length, and k_f is the thermal conductivity of the fluid. While many correlations exist to analytically

predict *Nu* for simple geometries and mainstream flow conditions [13], introducing coolant flow complicates the matter and has forced researchers to obtain *Nu* using experimental means [7].

Additionally, there are several other flow parameters used with regularity during film cooling investigations. The first of which is the coolant to freestream velocity ratio, *VR* (Equation 19). In practice, this parameter is used to scale the shear layer formed by the interaction of the mainstream and coolant flows. [20] The density ratio, *DR*, is another parameter that is important for film cooling (Equation 20). Eberly et al. [21] showed that higher density ratios increased the adiabatic film cooling effectiveness which would tend to increase the overall effectiveness. The mass flux ratio, *M*, or the "blowing ratio is the most commonly used parameter in scaling film cooling results (Equation 21). According to Bogard and Thole [1], the blowing ratio scales the thermal transport capacity of the coolant. Finally, the momentum ratio, *I*, is another parameter used for scaling film cooling performance (Equation 22). In particular, many studies have noted *I*'s ability to predict coolant film separation [6,20].

$$VR = \frac{V_c}{V_\infty} \tag{19}$$

$$DR = \frac{\rho_c}{\rho_\infty} \tag{20}$$

$$M = \frac{\rho_c V_c}{\rho_\infty V_\infty} \tag{21}$$

$$I = \frac{\rho_c V_c^2}{\rho_\infty V_\infty^2} \tag{22}$$

In Rutledge et al.'s study [10], it was determined that the optimal overall cooling performance for their semi-cylinder leading edge model, using a single coolant hole 21.5˚

off of the stagnation line, was achieved at M = 0.5. Degradation in cooling performance was observed at M's below and above this point. On the same semi-cylinder leading edge model, but with a full coverage showerhead film cooling scheme, Bryant observed different results [11]. Results from this test are shown in Figure 3. Three values of M were tested, M = 0.25, 0.5, and 0.9. For M = 0.25 and 0.5, Bryant found that the area around the stagnation line experienced high heating due to ingestion of the freestream. At M = 0.9, ingestion did not appear to be an issue causing this flow configuration to perform the best of the three tested flow configurations.

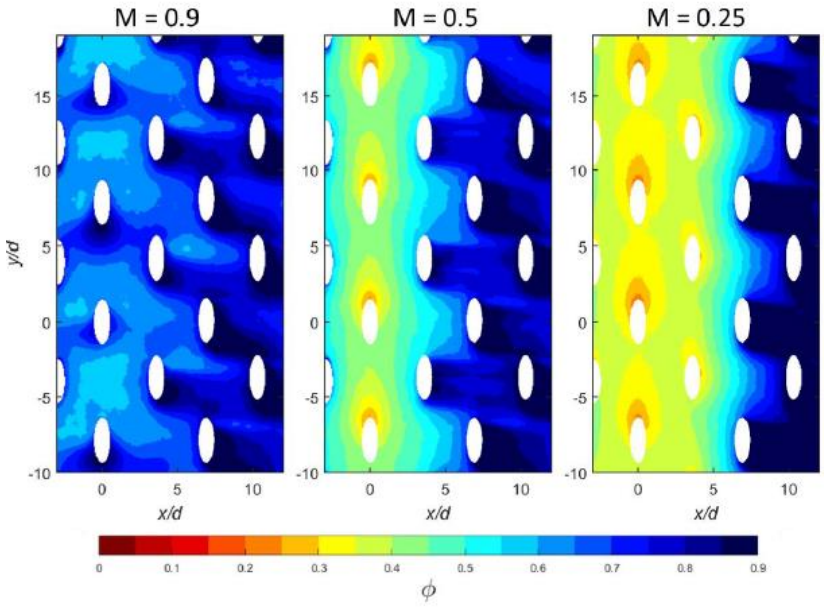

Figure 3. Overall effectiveness for showerhead film cooling configuration (M = 0.25, 0.5, 0.9). [11]

In the work performed by Williams et al. [9], adiabatic and overall effectiveness values were measured for a single row of film cooling holes on the suction side of a turbine vane model for varying momentum flux ratios. In their study, they found that adiabatic effectiveness, and overall effectiveness to some extent, was adversely affected by increasing momentum flux ratios. In their results, shown in Figure 4, it is evident that the coolant jets separate with increasing I resulting in lower effectiveness values downstream of the coolant

holes. For adiabatic effectiveness, the increased I clearly led to decreased η; however, there is a case to be made that the increased I led to improved ϕ. Although ϕ performance downstream decreased slightly, Williams et al. determined that spanwise averaged overall effectiveness, $\bar{\phi}$, increased with I up to I = 1.69, particularly near and between the coolant holes. It was believed that despite losing film performance, the higher I's led to increased internal cooling which led to increased overall performance.

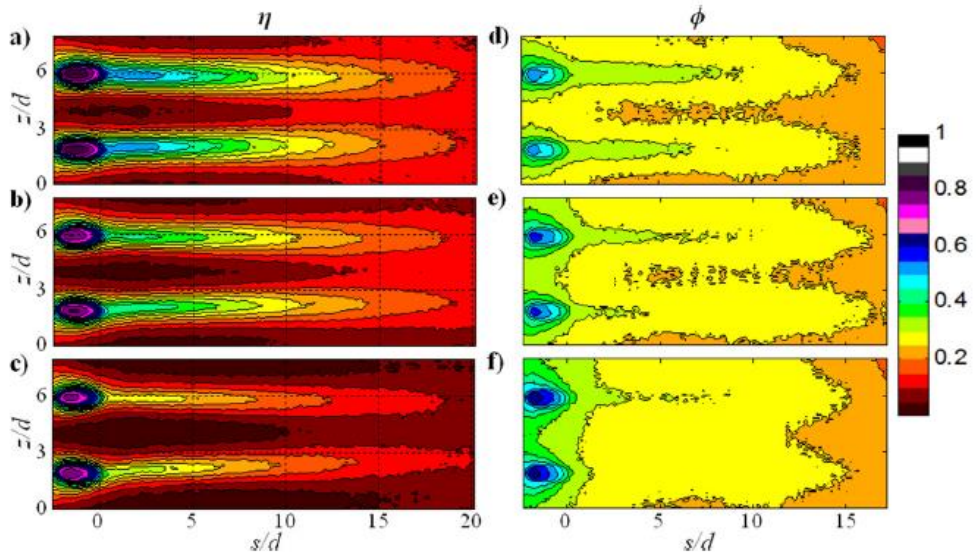

Figure 4. Contours of η and ϕ for approx. values of I = 0.38 (a,d), I = 0.62 (b,e), and I = 1.09 (c,f). Adapted from [9]

2.4. Factors Affecting Cooling Performance

In the literature, there are numerous studies investigating the many factors that affect cooling performance. The following discussions will explore some of the factors that affect cooling performance including geometry (Section 2.4.1) and flowfield effects. (Section 2.4.2)

2.4.1. Model Geometry Effects

In the literature, the geometries used in film cooling experiments are vast. Of great importance to cooling performance are the model's geometry, including the coolant hole geometry. The following will focus on these features and their effect on cooling performance.

While many film cooling experiments have been conducted on flat plate geometries, the results from these experiments do not necessarily translate to turbine blade geometries, particularly in the leading edge region and on the suction side of the blade. Because the leading edge of turbine blades are convex, it is important to understand the effect curvature has on film cooling performance. According to Bogard and Thole's [1] film cooling review, for a convex surface, the ratio of the coolant to freestream momentum, *I*, determines whether the jet will experience liftoff. If the coolant jet momentum is less than the freestream momentum, the resulting radius of curvature for the jet will be less than the surface's radius of curvature leading the jet to be pushed against the surface. Alternatively, if the coolant jet momentum is greater than the freestream momentum, the resulting radius of curvature will be greater than the surface's radius of curvature and the coolant jet will tend to move away from the surface.

Ito et al. [8] examined curvature effects on adiabatic effectiveness. Figure 5 shows the laterally averaged adiabatic effectiveness achieved on a convex surface across a range of *M*. The largest effectiveness occurred at $M = 0.5$. Lower *M*'s achieved higher effectiveness values while increasing past $M = 0.5$ decreased effectiveness because of penetration of jets through the boundary layer. Figure 6 shows a comparison of adiabatic effectiveness values achieved at $M = 0.5$ and varying values of *I* on flat, convex, and concave walls. In general, the convex configuration performed the best followed by the flat and concave configurations,

respectively. It is also apparent that the convex and concave configurations display opposite trends with respect to *I* where the effectiveness on the convex surface increases with increasing *I* while the concave surface effectiveness decreases.

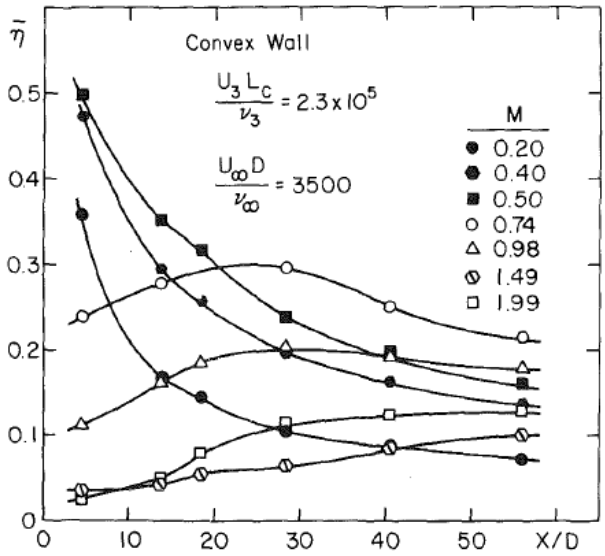

Figure 5. Laterally averaged effectiveness on convex surface [8]

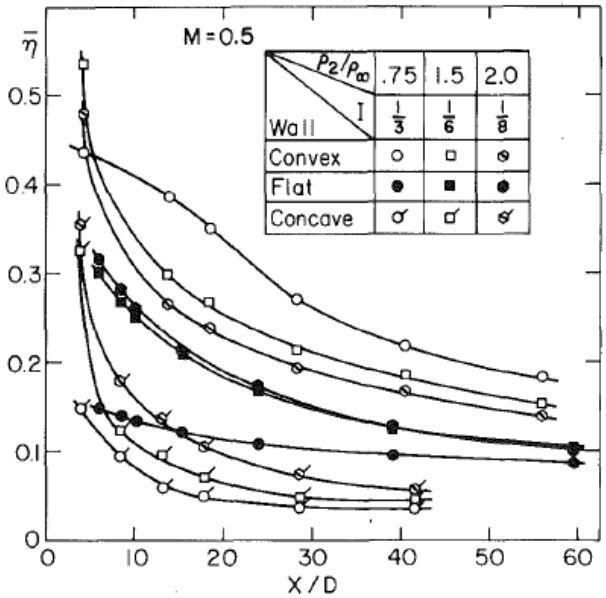

Figure 6. Comparison of laterally averaged effectiveness for convex, flat, and concave walls. [8]

Cooling hole geometry and configuration can also have an impact on film cooling performance. One parameter of interest is the cooling hole spacing, also known as the pitch

(P). Bogard and Thole [1] note that greater film coverage can be achieved as the cooling hole spacing is decreased. Sweeney and Rhodes [14] did a limited examination of how hole spacing affected film cooling performance on their double-wall film-cooled flat plate test specimen. Two different hole spacing configurations were tested. They determined that the closer spaced hole configuration produced significantly higher overall effectiveness compared to the farther spaced hole configuration.

In addition to investigating hole spacing effects, Sweeney and Rhodes [14] also investigated the effect of coolant jet injection angle on overall effectiveness. They tested two different injection angles: 90˚ and 30˚ to the surface. They found that the 30˚ cooling holes outperformed 90˚ film cooling holes. They observed up to 10% improvement in spanwise-averaged effectiveness for the 30˚ holes over the 90˚ holes. Bogard and Thole [1] note that most coolant holes are angled at 25˚ to 35˚ because these angles aid in keeping the coolant attached to the surface. Due to geometric constraints on a component, however, angled holes are not always viable and shallower holes are not able to be incorporated into a turbine wall.

Another important parameter is the compound angle. The compound angle is defined as the angle formed by the direction of the coolant jet ejection and the direction of the freestream flow. For instance, when the coolant hole is oriented in the streamwise direction, the compound angle is 0˚ and is 90˚ when the coolant hole is perpendicularly oriented to the streamwise direction. Holes with a 90˚ compound angle are typically reserved for use in the leading edge region of turbine vanes and blades.

Finally, hole shape also has an effect on film cooling effectiveness. The common shapes used are shown in Figure 7. The first hole shown is a standard straight cylindrical. The second hole shown expands laterally as it exits the wall and referred to as a fan-shaped

hole. The third hole shown expands laterally as it exits, too, but it also expands into the streamwise direction changing the angle of the hole exit.

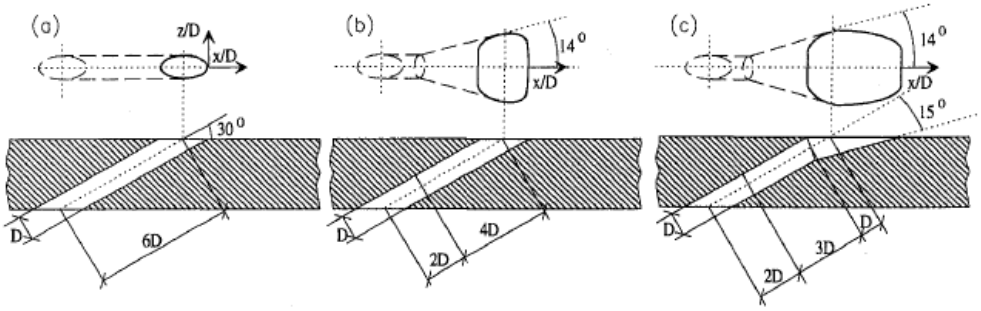

Figure 7. Different hole shapes: (a) cylindrical, (b) fan-shaped, (c) laidback fan-shaped. Adapted from Suamweber et al. [22]

Gritsch et al. [23] examined the effect of shaped holes on the film effectiveness over a flat-plate geometry. Their results are shown in Figure 8. Both fan-shaped holes significantly outperformed the cylindrical holes. They also found that the laidback fan-shaped hole was better able to spread the coolant laterally resulting in higher laterally averaged film cooling effectiveness compared to the other two holes.

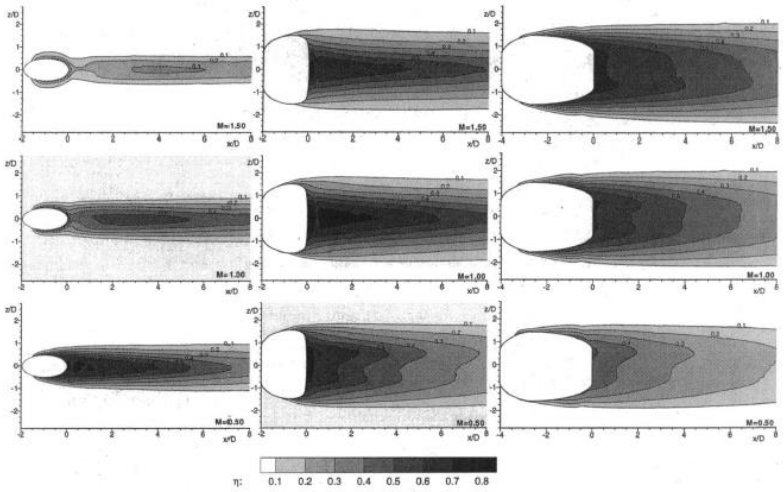

Figure 8. Film effectiveness for cylindrical and fan-shaped holes (w/ and w/out laid-back). [23]

2.4.2. Flow Effects

Per Bogard and Thole [1] when a coolant jet is injected into the freestream flow, the shear layers formed by the interaction of the two flows generate turbulence within the boundary layer. Turbulence can have a couple of effects. High turbulence can increase coolant mixing with the hotter freestream fluid leading to a film temperature which could degrade film cooling performance. Turbulence also has the ability to impact the heat transfer coefficient. The turbulence created by film cooling generally leads to undesirable higher *h*'s than cases without film cooling.

Internal flow effects are also important to understand component cooling. Specifically, impingement heat transfer has been investigated by Gau and Chung [24] on both convex and concave surfaces using varied jet widths. In the case of an impingement jet on a concave surface, they found that the centripetal force due to the curvature of the surface makes the flow unstable and produces a series of Taylor-Görtler vortices. According to Mayle et al. [25] and Thomann [25], these phenomena can significantly increase the momentum and energy exchange in the flow and enhance the heat transfer on the wall. The work performed by Gau and Chung [24] examined singular jets of varying slot widths, *b*, placed at varying distances, *Z*, from a curved surface. Local heat transfer results from impingement on a concave surface can be seen in Figure 9. In general, they found that *Nu* increased with increasing surface curvature.

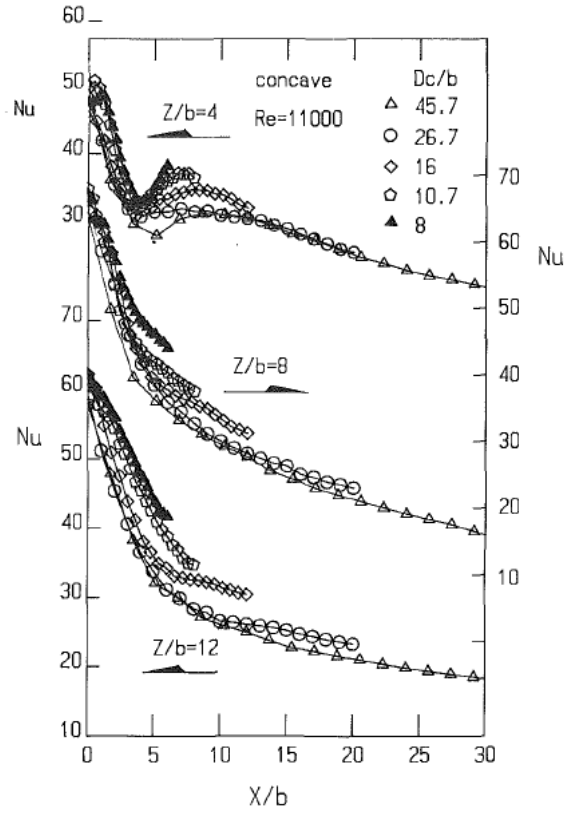

Figure 9. Effect of concave surface curvature on local heat transfer *Nu* for *Re* = 11,000 and *Z/b* = 4, 8, and 12. [24]

Ravelli et al. [26] computationally investigated the effect of internal impingement cooling configurations on the overall effectiveness of a film cooled leading edge model. The leading edge used three rows of coolant holes positioned along the stagnation line and at ±25˚. The internal cooling was provided using three different impingement plate configurations. A case without an impingement plate was also simulated. Conditions investigated were *DR* = 1.5 and *M* = 1.0 or 2.0. Result showed that overall effectiveness was only slightly improved by impingement cooling and was consistent with the experimental results of Mouzon et al. [27]

Chandran and Prasad [28] performed both computational and experimental studies to determine the impact of the blowing ratio and the freestream Reynolds number on a leading

edge model that employed both internal impingement cooling and a showerhead film cooling scheme. For their examination, they used three different Reynolds numbers (Re_1 = 4.8 x 10^5, Re_2 = 9.6 x 10^5, Re_3 = 14.4 x 10^5) along with three different blowing ratios (M = 1, 1.5, and 2). They performed experiments on two models of the same geometry but that had different thermal conductivities: k_A = 0.2 W/m-K and k_B = 14.9 W/m-K. The high thermal conductivity material displayed a more uniform overall effectiveness distribution in both the streamwise and spanwise directions compared to the lower thermal conductivity material. A key finding was that increased Reynolds number led to decreased effectiveness for both materials at all blowing ratios. The high conductivity model experienced a 6% reduction in effectiveness by tripling the Reynolds number from 4.8 x 10^5 to 14.4 x 10^5.

Dees et al. [7] made experimental measurements and computational predictions of cooling performance produced by internal cooling channels on a scaled up simulated turbine vane. The test airfoil's overall internal layout is shown in Figure 10, however, the experiment involved installing rib turbulators at various locations in the channel to augment the heat transfer coefficient. Rib turbulators placed on the suction side wall of both the second leg of the U-bend channel, which has a stream-wise location of 0.41 < s/C < 0.61, and the radial channel, which has a stream-wise location of 0.64 < s/C < 1.0. Tests were with run with internal Re flows between 10,000 and 40,000.

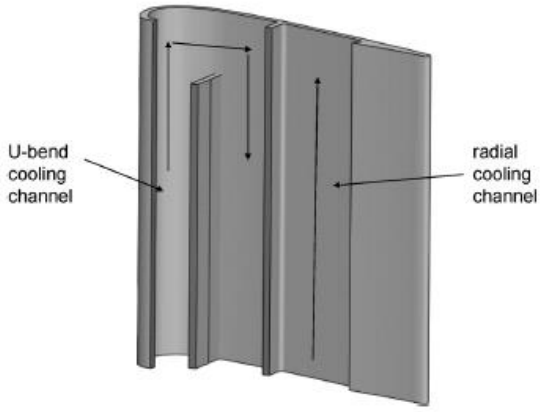

Figure 10. Internal Convective Cooling scheme used by Dees et al. [7]

Spanwise averaged overall effectiveness results from this experiment [7] and a previous experiment conducted with smooth channel walls [29] are shown in Figure 11. From these results, they showed that the overall effectiveness improved due to enhancement of the internal heat transfer caused by the rib turbulators. Additionally, they found that internal heat transfer increased with increasing *Re* leading to improved overall effectiveness at the higher *Re*'s.

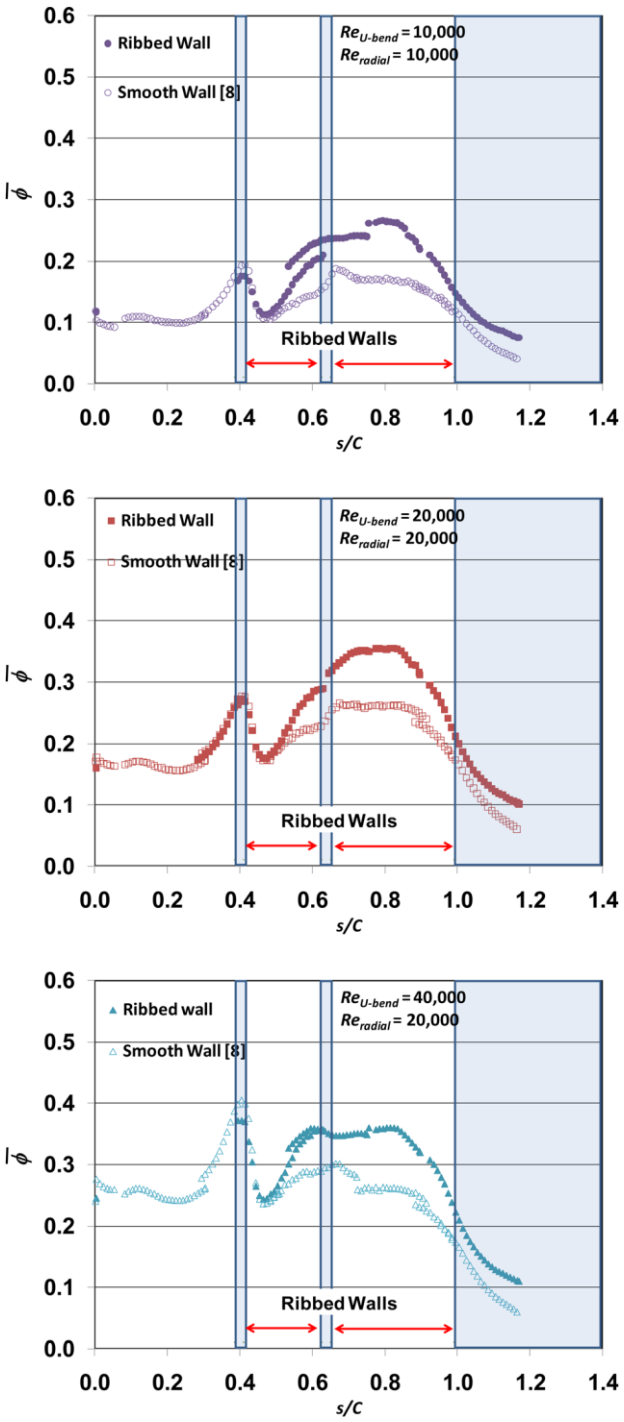

Figure 11. Spanwise overall effectiveness results by Dees et al. [7]

2.5. Measurement Techniques

This section discusses a few of the thermal measurement methods that have been used to find h, η, ϕ, and other related parameters. In the literature, a large variety of thermal

methods have been developed and employed including thermocouples [24], thermochromic liquid crystals (TLCs) [8], infrared (IR) thermography [14], and heat flux gauges [12]. To determine which method to use, several factors must first be considered. Among the most important considerations are what parameters are being measured; required spatial resolution; required measured quantity accuracy; instrumentation access; and the flow/temperature regime.

The first and simplest temperature measuring method is using thermocouples. Using thermocouples provides accurate temperature measurements at discrete locations. Thermocouples can be calibrated to make measurements within a high degree of accuracy over a wide range of temperatures. For example, Omega® k-type thermocouples have a temperature operating range of -200 ˚C to 1250 ˚C with standard limits of error of ±2.2 ˚C or ±0.75% of the reading, whichever quantity is larger [30]. Unfortunately, thermocouples usually offer the lowest spatial resolution compared to the other measurement methods. Another potential issue when using thermocouples is the uncertainty in actual placement which can severely impact heat flux measurements. Finally, because thermocouples are placed on the surface of test articles, they can disrupt the flow and can be intrusive, especially in space constrained environments like those experience in true-scale testing.

Another method to measure surface temperature is with thermochromic liquid crystals, or TLCs. In contrast to thermocouples, TLCs can provide a high resolution, two-dimensional temperature map. TLCs are deemed to be fairly non-intrusive; however, some the drawbacks of using TLCs include their limited operating temperature range (max 100 deg C) [31] and the high amount of surface preparation required to use them.

As mentioned earlier, there are numerous tools available for thermal measurement. In addition to thermocouples, this research will use both infrared thermography and heat flux gauges to make thermal measurements that will enable the determination of values like overall effectiveness, local convective heat transfer coefficient, and the Biot number. Section 2.5.1 reviews infrared thermography in more detail while Section 2.5.2 reviews heat flux gauges in more detail.

2.5.1. Infrared Thermography

Infrared (IR) thermography relies on detecting the radiation emitted by the object being measured. Radiation emitted by a black body emits according to the Stefan-Boltzmann Law shown in Equation 23 where σ is the Stefan-Boltzmann coefficient and T_w is the object's surface temperature. In theory, if one could measure the emitted radiation of an object, then a wall temperature could be backed out using Equation 23.

$$q"_{rad,b} = \sigma T_w^4 \tag{23}$$

Real objects do not display blackbody behavior, however, and radiate at a value lower than the black body value. Instead, the true value is determined partially by the surface emissivity, ε, which has a value bounded between 0 and 1. Equation 24 represents the surface radiation of a real object.

$$q"_{rad,b} = \varepsilon\sigma T_w^4 \tag{24}$$

IR thermography uses an IR detector to record values of surface radiation that can be used, in conjunction with a known surface emissivity, to determine the temperature of an object's wall. This method of measuring temperature is advantageous because it is non-intrusive and, just as in the case of TLCs, can produce a two-dimensional surface temperature

map while reducing the amount of equipment needed [14]. To obtain reliably known surface emissivities, test surfaces are usually painted with a heat resistant flat black paint [14]. A drawback of IR thermography is that the method requires optical access. This is usually achieved by making use of an IR-transparent window, usually made of quartz [4], zinc selenide [14], sodium chloride [6], or sapphire [16]. Additionally, IR thermography has been used for both steady [16] and transient [31] heat transfer tests. However, knowing the emissivity of an object does not guarantee that an object's temperature can be accurately backed out using measured surface radiation values. That is because there exist other sources of radiation that can pollute the values of radiation detected by the detector. These other sources of radiation must be accounted for and this is usually accomplished by performing an in-situ calibration using embedded thermocouples to provide reference temperatures for the calibration.

There appear to be two primary methods of performing in-situ calibrations. The first employed by Martiny et al. [32] and Ochs et al. [33] begin with observing how spectral infrared radiation is related to the temperature of a black body through Planck's law, shown in Equation 25:

$$q"_b(\lambda) = \frac{c_1 \lambda^{-5}}{e^{\frac{c_2}{\lambda T}} - 1} \tag{25}$$

where λ is the wavelength and c_1 and c_2 are physical constants. However, real objects radiate below their black body values which is determined by their emissivity as shown in Equation 26:

$$q"_g(\lambda) = \varepsilon(\lambda) * q"_b(\lambda) = \varepsilon(\lambda) * \frac{c_1 \lambda^{-5}}{e^{\frac{c_2}{\lambda T}} - 1} \tag{26}$$

Using this relation and solving for *T*, the temperature of an object could theoretically be determined by measuring the spectral irradiance assuming that the emissivity of the object is known as shown in Equation 27:

$$T = \frac{c_2/\lambda}{\ln\left(\frac{\varepsilon(\lambda) * c_1 * \lambda^{-5}}{q"_g} + 1\right)} \tag{27}$$

Using this same logic, Martiny et al. [32] suggested using a semi-empirical relation based on the relation demonstrated by Planck's law. The relation, shown in Equation 28, relates the radiation detected, *I*, to the temperature of the object, *T*, using three new parameters: *R*, *B*, and *F*.

$$I = \frac{R}{e^{B/T} - F} \tag{28}$$

Again, temperature can be solved for by rearranging the equations like:

$$T = \frac{B}{\ln\left(R/I + F\right)} \tag{29}$$

In this new form, known pairs of temperatures and detected radiation values could be used to determine the remaining three coefficients, *R*, *B*, and *F*, using a nonlinear least square fit described further in Martiny et al. [32] Figure 12 demonstrates the improved temperature measurement capability after performing the in-situ calibration as just described versus using the factory calibration.

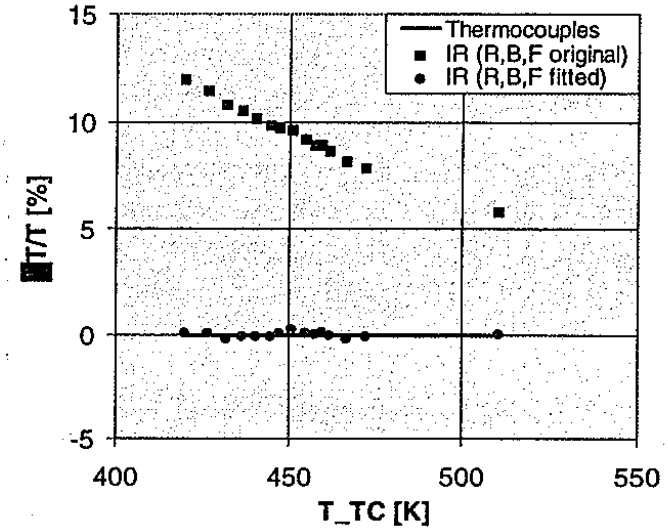

Figure 12. Resulting errors of thermal measurements using original and new calibration coefficients[7]

The alternative in-situ calibration has been used in several experiments conducted with AFIT's small scale film cooling rig [16,34] and uses the established relationship between temperature and radiative heat flux characterized by the Stefan-Boltzmann law discussed earlier. This technique uses an IR imager and thermocouples, like the previous technique, to measure the emitted radiation intensity and temperature of a test surface. Recognizing that radiative heat transfer exhibits fourth-order behavior, a relationship between temperature and radiative intensity can be setup, as shown in Equation 30.

$$T = a\mathcal{J}_{rad}^{1/4} + b \tag{30}$$

where $\mathcal{J}_{rad}$ is a count of photons striking the IR imager's sensor and a and b are constants determined by a curve fit. The curve fit is produced from data collected at different surface temperatures. An example from Vorgert [34] is shown in Figure 13.

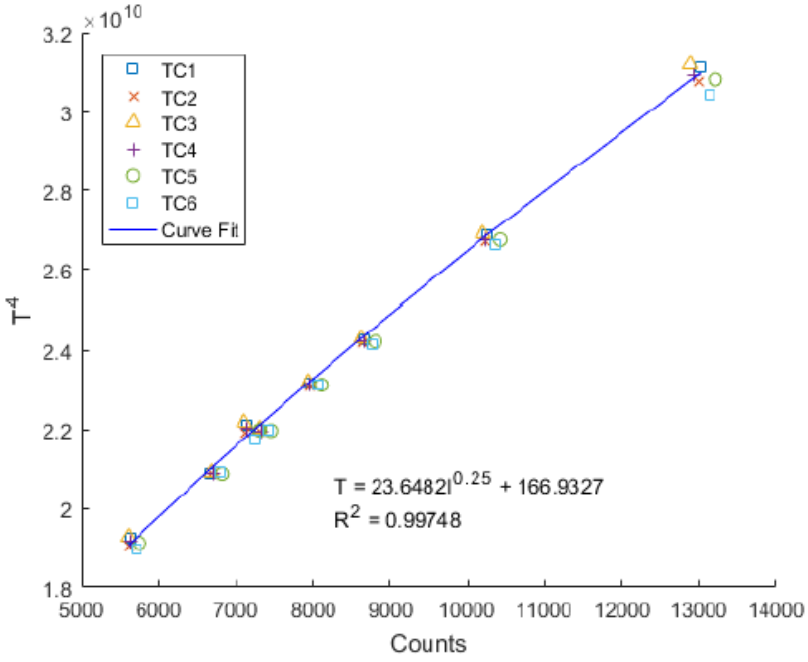

Figure 13. Vorgert in-situ IR calibration example. [34]

Additionally, Ashby [16] showed that the relationship can be modified to capture relationships that may not be present in other testing environments. FCR experiments appear to have stuck with this technique because its relative ease of use and the adaptability that it has shown.

2.5.2. Heat Flux Gauge

Thin film heat flux gauges are used to measure the heat flux imparted on a surface. In the 1960s, these devices first found use in short duration tests measuring the heat flux on re-entry vehicle models [35]. At the time, there existed only one-sided gauges which relied on the semi-infinite solid assumption, meaning that it was assumed that the thermal pulse into the model and gauge did not fully penetrate to the other side during the test. This assumption, as noted by Jones [35], is important because it allows users to assume one-dimensional, unsteady heat transfer. A way of ensuring that the semi-infinite solid

assumption holds is by performing short duration tests. Typically, short duration can last on the order of milliseconds up to 100 seconds [35].

However, because true-scale film cooling models are usually thin-walled and metallic, this assumption does not usually hold. In response to this issue, double-sided heat flux gauges were developed as explained by Piccini et al. [36]. Figure 14 shows an example of a double-sided heat flux gauge as installed on a model's surface. It can be used in both steady and unsteady experiments. In the steady case, it is adequate to use the one-dimensional Fourier's Law (Equation 4) to determine the heat flux. If unsteady, users will need to use the same methodology of the one-sided gauges to determine the heat flux.

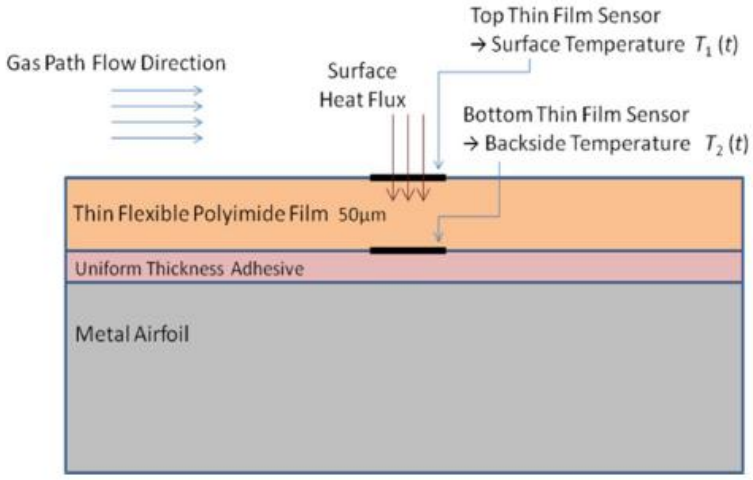

Figure 14. Double-sided heat flux gauge. [37]

As part of their gas turbine research, the Air Force Research Laboratory (AFRL) had developed flexible double-sided heat flux gauges to make measurements on their Research Turbine test rig, a full scale, single stage turbine rotor [37]. Their platinum thin film sensor acted as a resistance thermometer which changed resistance with changes in temperature. The change in resistance would lead to a change in voltage drop across the sensor. The

relationship between temperature change and the change in voltage across the sensor is shown in Equation 31.

$$\Delta V = V_0 \alpha_R (T - T_0) \tag{31}$$

where α_R is the thermal coefficient of resistivity of the film for which they had to perform a calibration to determine. The calibration process used by AFRL involved using temperature controlled baths to heat and cool the sensors to change their resistance. Both temperature and resistance values were recorded throughout the process. The data could then be used to create a calibration curve where the slope was equal α_R. Once calibrated, the sensors on either side of the film could simultaneously measure temperatures at high collection rates with a fairly low degree of uncertainty. Figure 15 demonstrates how heat flux measurements, along some additional temperature measurements, can be used to determine other parameters of interest such as the adiabatic effectiveness and the convective heat transfer coefficient.

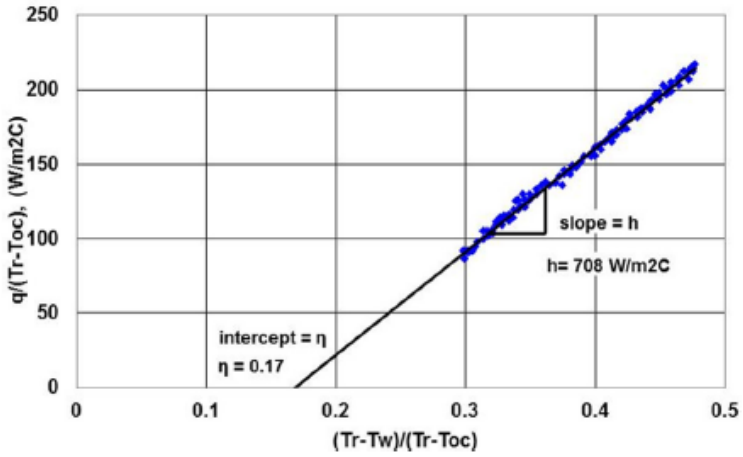

Figure 15. Heat flux data from Popp et al. [38] **reproduced by Polanka et al.** [12]

3. Experimental Methodology

This investigation called for the modification of the Film Cooling Rig (FCR) located in the Combustion Optimization and Analysis Laser Laboratory (COAL Lab) located at the Air Force Institute of Technology (AFIT). The FCR, originally designed and built for reactive film cooling investigations [39], has undergone many incremental changes over its lifespan to accommodate new investigations. For this particular study, the rig needed a considerable amount of changes to enable a comparison of Bryant's large scale results [11] to engine scale results produced in this study. A cutaway view of the final overall redesign of the FCR is shown in Figure 16. The figure highlights new support components such as the toroid bypass and mounting assembly that will be discussed in Section 3.1 as well as new and modified test section components that will be discussed in Sections 3.2 and 3.3.

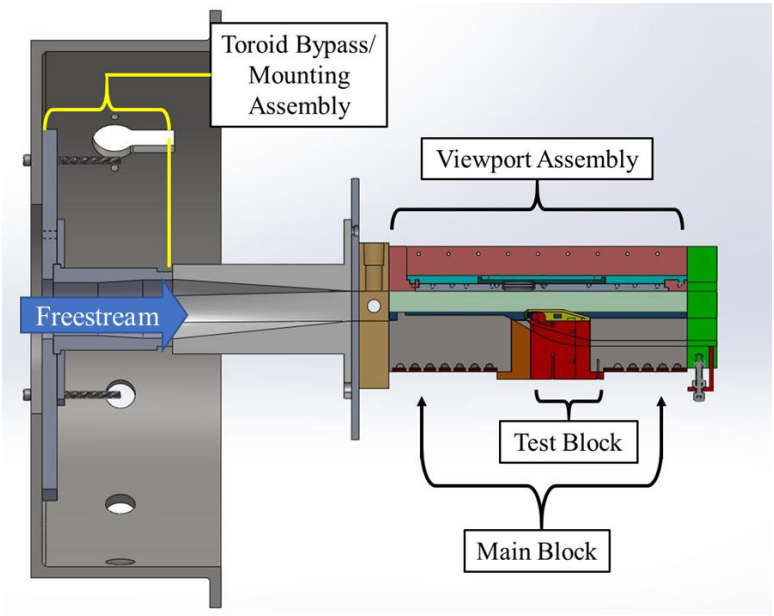

Figure 16. AFIT Film Cooling Rig cross section.

Despite the large overhaul of the test section, most of the support equipment required for this investigation was already available. Details of the facility and support equipment used for this work will be reviewed in Section 3.1. The new design work that led to the new

composition of the FCR and implemented changes are discussed in detail in Section 3.2. The new measurement equipment and procedures used to characterize the FCR are outlined in Section 3.3. The chapter closes with an uncertainty analysis in Section 3.4.

3.1. Support Equipment

Previous investigations in the COAL lab have developed the infrastructure for the Film Cooling Rig. In previous research, the primary means for supplying air to the FCR were through both an 0.75" and 3/8" lines for the freestream and coolant flows, respectively. Through some preliminary testing with the 0.75" supply line, it was found that this system could provide a freestream flow in excess of 1700 SLPM. However, the target flow rate planned for these experiments, based on achieving a freestream *Re* of 20,000 using the leading edge diameter at a nominal freestream temperature of 600 K, was estimated to be 2960 SLPM. In order to reach the desired flow conditions, the freestream supply line needed to be increased. Within the COAL lab, a 1.5" supply line existed which was primarily used for other research [40] but required some additional plumbing to route the air supply line to the FCR. Upon completing the new plumbing, preliminary testing with the new line showed that a flow rate of around 2750 SLPM could be sustainably maintained which was inadequate to achieve the initial target condition. For this reason, the new max target flow, based on achieving a *Re* of 15,000 at a nominal freestream temperature of 600 K, was reduced to 2225 SLPM. Figure 17 provides a simplistic view of the air flow path for this work.

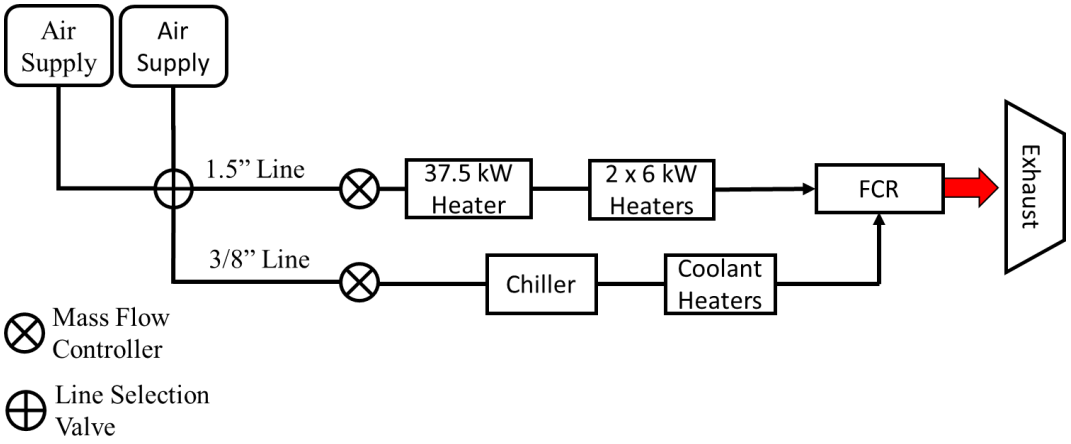

Figure 17. FCR air flow diagram.

For this research, the air was provided by one of two systems. Initially, testing, including the preliminary flow capacity testing, was conducted using freestream and coolant air provided by two Kaeser BSD-50 air compressors which are shared assets for other AFIT labs surrounding the COAL lab. On several occasions, testing was interrupted due to large fluctuating flows where massive flow drop-offs were experienced. During these events, the rig was shutdown and re-initialized to attempt to recover functionality but the root cause was never discovered. One possible cause was thought to be high demand on the AFIT air supply during these times. For this reason, it was decided to switch the air supply source to the COAL lab air compressors which was an asset only available to the COAL lab. This system uses an Ingersoll Rand H50A-SD compressor installed by Parks [40] and was used mainly in the Ultra Compact Combustor (UCC) research conducted in the same lab. According to previous work with the Ingersoll compressor [40], it can provide up to 1 kg/s of atmospheric pressure air or a maximum of 0.1 kg/s at 862 kPa. This work only required atmospheric pressure air and was not projected to exceed to 1 kg/s. The system also used two Ingersoll Rand vertical dryers to remove moisture from the compressed air. As the test matrix was already set, the maximum flow rate was never investigated with this source.

Whether using the AFIT air supply or the COAL lab air supply, both supply lines fed to the main air flow manifold shown in Figure 18. During this work, there were four air supply lines available. The 3” line was exclusively used by the Ultra Compact Combustor (UCC) research group while the 0.75” and the 0.375” supply lines were used exclusively with the film cooling research. The 1.5” supply line was previously used primarily by the UCC research group; however, the flow demands for this research required that we begin using the 1.5” supply line as previously discussed.

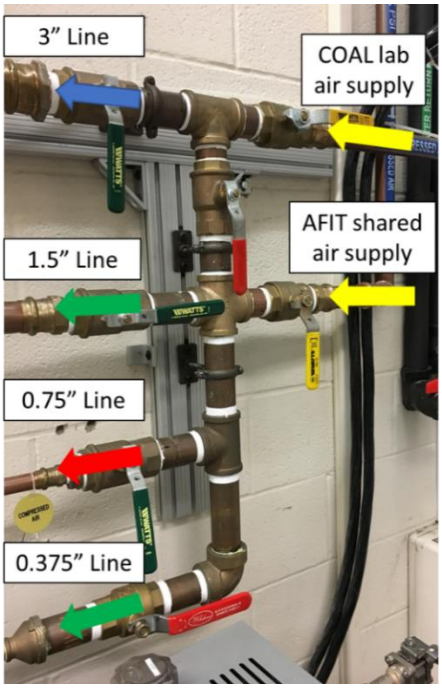

Figure 18. Main air flow manifold.

Each flow line was outfitted with the same flow control equipment sized appropriately for each line size. For the 1.5” line, this equipment included an air-powered solenoid valve, pressure regulator, flow meter, and flow control valve as depicted in Figure 19. The UCI solenoid valve was controlled via the modified LabVIEW program used by Vorgert [34] to open and close the line from the control station. After passing the solenoid valve, a Fisher 299h pressure regulator ensured that the line pressure needed to support the

desired mass flow rate was achieved. As described by Damele [40], this regulator steps down the pressure from the chosen air supply source to the pressures required for the desired mass flow rates. The freestream flow rate is then measured by a Fox Thermal Instrument, Inc. FT2 flow meter and was controlled via a Eurotherm 2404 process controller in conjunction with a FlowServe MaxFlo 3 control valve which is rated to a maximum flow rate of 0.3 kg/s.

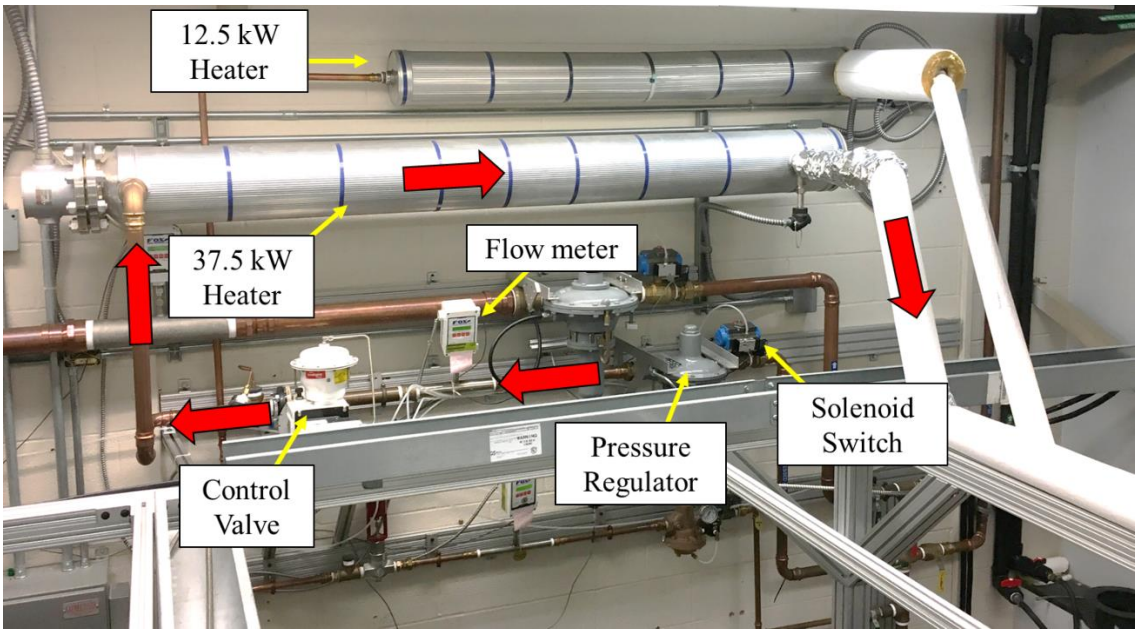

Figure 19. Freestream support equipment and flow path of 1.5" supply line.

Previous experiments conducted with the FCR tended to experiment in two mainstream temperature regimes, "cold" and "hot". Cold flow tests conducted by Vorgert [34] used a Gaumer Process 12.5 kW electric heater, shown in Figure 19, to reach freestream temperatures up to 420 K. Hot flow experiments, including those performed by Vorgert, were conducted at temperatures between 1100 K and 1600 K [16,34,39]. Temperatures in this regime were achieved with the help of a well-stirred reactor (WSR), which Vorgert describes in his work. While the WSR enabled more realistic engine testing temperatures, previous studies determined that the WSR was limited to operating with flow rates less than 700 SLPM. It was found that operating beyond this flow rate could result in blowout, where

combustion would migrate into the test section. However, as previously discussed, the max target flow rate was 2225 SLPM which greatly exceeded the blowout rate of the WSR and meant that the WSR could not be used for this work. While the WSR was no longer available as a source of heat, switching to the 1.5” supply line meant that the pre-existing 37.5 kW Gaumer Process heater, shown in Figure 19, could be used to heat freestream flow. According to Anderson [41], this heater has the ability to heat the freestream flow up to 810 K; however, he warned that operating the heater beyond 670 K could melt the Teflon pipe dope used in the plumbing which poses a safety concern. For this reason and in anticipation of the heat loss expected to occur as the air travels from the heater to the rig, it was decided to seek out a supplemental heat source.

After some initial surveying of potential solutions, it was discovered that Osram Sylvania had inline electric heaters that could possibly fill the need. The main requirements for the supplemental heat source were that it had to be compatible with the 1.5” line, it must be leak proof, and it must be capable of producing and maintaining freestream temperatures of 600 K. Figure 20 is the performance map provided by Osram for several of their threaded inline electric heaters. Using this performance map, it was determined that two 6.0 kW heaters could be used to achieve freestream temperatures of 600 K when used in conjunction with the Gaumer process heater for freestream flows near 2260 SLPM. The assumptions made for this assessment was that each heater would see half of the flow, 1130 SLPM, and that the upstream heater could warm the freestream to 420 K before hitting the new heaters. Using the chart and finding the performance line for the 6 kW heater, the map shows that heaters could warm air supplied at room temperature up to a maximum temperature of around 250 ˚C, or 523 K. Assuming comparable heating performance when supplied with air already

heated by the existing upstream heater, the projected maximum freestream temperature was predicted to be around 650 K.

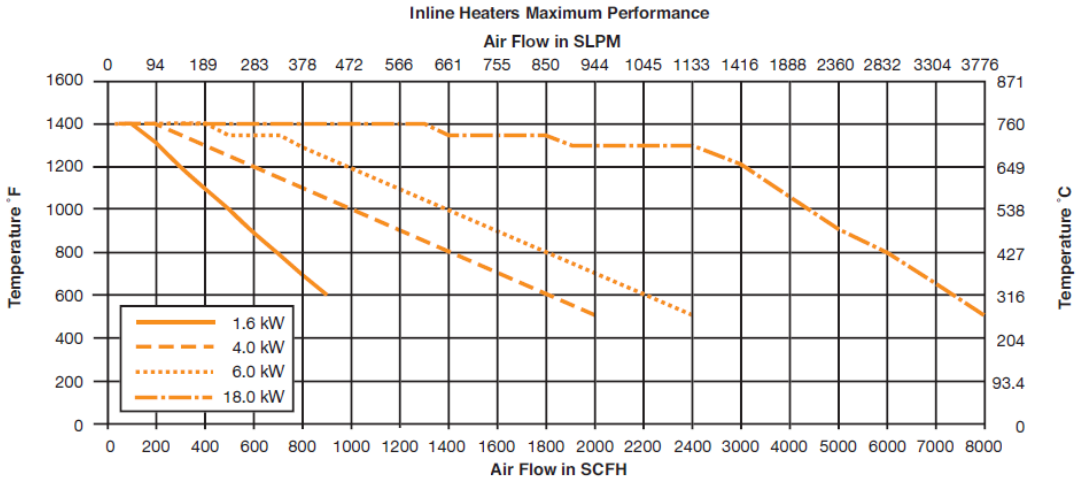

Figure 20. OSRAM Heat Performance map [42].

The Osram heaters purchased were 6 kW inline electric heaters with 1.25" MNPT threaded ends. The heaters are of the "Style A" variety which means that they are leak proof and rated to operate at a maximum inlet pressure of 150 PSI and a maximum inlet air temperature of 755 K. One of the heaters is shown in Figure 21. Also shown in Figure 21, is the "heater loop" design. In this design, the heaters have a common inlet and common outlet and are placed in parallel, rather than in series, in an attempt to reduce the velocity through each heater to warm the freestream to the target temperature of 600 K. Because the heaters' threading was smaller than what was being used prior, several 1.5"-to-1.25" reducer couplings were used to connect the heaters to the rest of the plumbing. To support closed loop operation of the heaters and to monitor heater performance, the reducer couplings on the exit side of the heater were modified to enable insertion of a 0.062" diameter k-type thermocouple behind both heaters and a 0.125" diameter thermocouple behind one heater to provide a reference temperature to the heaters' controller. An additional complication

encountered while attempting to assemble the heater loop was the inability to complete the loop using regular pipe fittings. The issue was that all of the fittings were right-handed fittings. When attempting to make the last connection in the loop using regular fittings, the fitting would tighten while another loosened. The solution to this problem was to use union fittings on one half of the loop which enabled tightening of the fitting without loosening another. As mentioned earlier, there was some concern with melting our pipe sealer while testing at high temperatures so the plumbing was sealed using high temperature PFTE tape rated for use up to 1255 K.

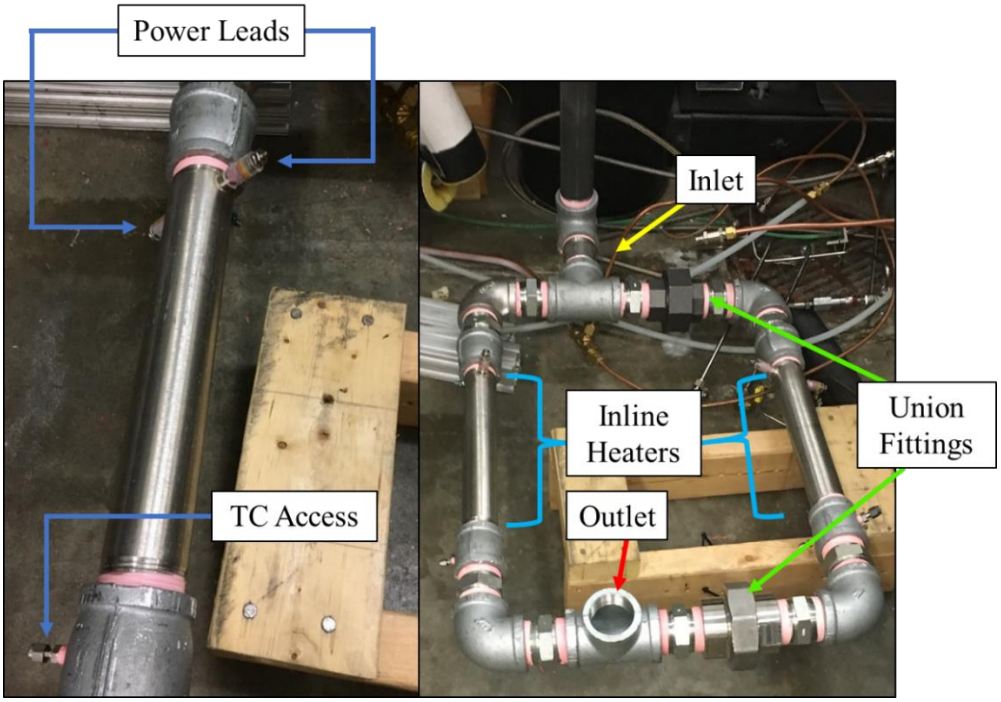

Figure 21. Individual OSRAM 6 kW Inline Heater (Left) and assembled heater loop (Right).

The heater loop exit was then connected to the rig using a 18" long flexline purchased from Main Line Supply. The flexline was used in place of a rigid line to accommodate thermal expansion as the line was heated. The flexline connected to the rig through a new fitting created for this work. In previous work with the FCR, the WSR was not only used to heat the flow but also served as the entry for air into the rig and also as a base for which the

FCR test section to rest upon. However, because this experiment switched air supply lines and new heating sources were added, the WSR was no longer needed and was removed leaving a void. To fill this void, a new fitting dubbed the toroid bypass, shown in Figure 22. The design requirements for the toroid bypass fitting dictated that one end could receive a 1.5”MNPT fitting from the air supply line and the other end could fit into an existing transition stack used in experiments performed by Ashby [16]. The toroid bypass, in conjunction with a new mounting assembly, also served as the new base supporting the FCR test section within the protection well previously used to shield the lab surroundings from the WSR as shown in Figure 22. The toroid bypass was mounted to the bottom of the well through a clamping design.

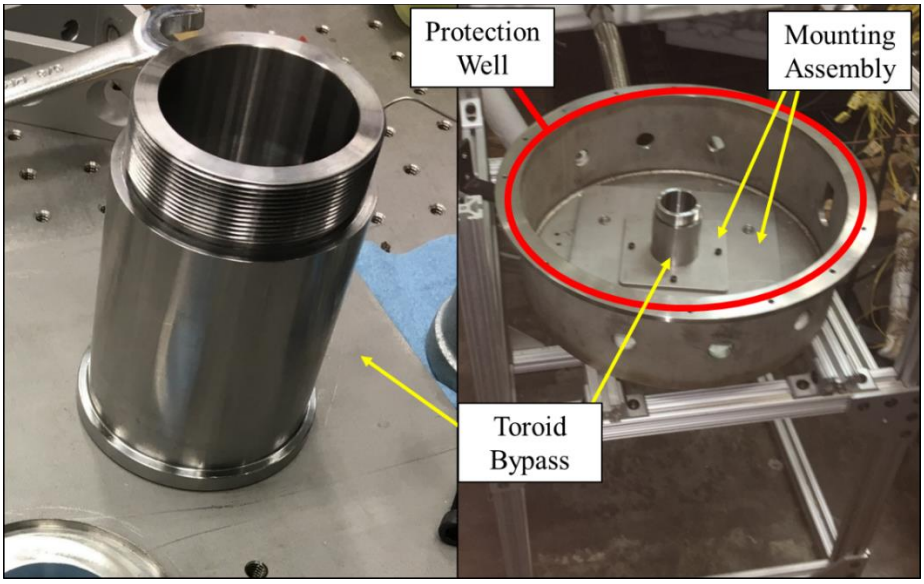

Figure 22. Toroid bypass (left) and mounting assembly (right).

Before entering the FCR test section, the flow passes through the transition stack. There are two versions of the stack used in previous research. The first stack combined a steel chimney outer shell and a ceramic inner core that changed the shape of the duct from a circular duct at the entrance to a rectangular duct at the exit that feeds the test section. The

second stack serves the same purpose but is made entirely of aluminum. For this investigation, the aluminum stack, shown in Figure 23, was used. The inner diameter through the lower stack to the entrance of the upper stack matched the exit diameter of the toroid bypass at 49.5mm. From the entrance to the exit of the upper stack, the duct shape changes from a circular duct to a rectangular duct. The exit duct measures at 50.8 mm wide by 25.4 mm tall which matches with the entrance of the test section.

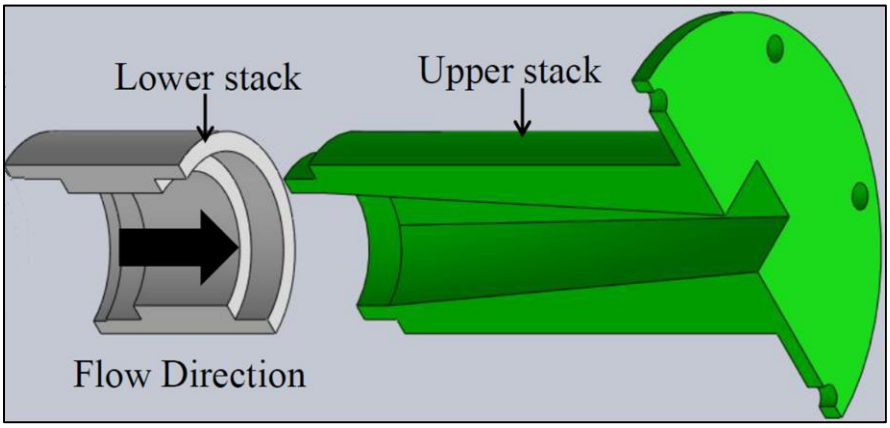

Figure 23. Aluminum transition stack adapted from Ashby [16]**.**

For each test, the coolant flow was supplied by the same source as the freestream through the 0.375" line discussed earlier. For this line, a Valtek pressure regulator was used to step down the pressures before continuing through the line. The coolant flow rate was controlled by a MKS MC20A mass flow controller, which could command up to 50 SLPMs, and was managed by a MKS Model 647 C multi gas controller. Before reaching the rig, the coolant temperature could be adjusted using a combination of two inline electric heaters, a 1200 W OMEGALUX AHPF-121 and a 400 W OMEGALUX AHPF-061, and a Cole-Parmer 1C6 cooling/heating circulating bath. The electric heaters, shown in Figure 24, could be independently controlled via two Dart power controllers while the chiller was standalone unit. A maximum coolant temperature of 600 K was reached in previous experiments using

only the 1200 W heater [16]; however, a maximum temperature obtained using both heaters was never determined. The maximum coolant temperature needed for this work was only 410 K which was well within the heaters' capability. The chiller had the ability to produce cooling fluid temperatures as low as 253 K; however, the lowest air temperatures observed at the entrance of the rig was no lower than 283 K. During experiments, it was also observed that the coolant temperature was also affected by the coolant flow rate and the temperature regime.

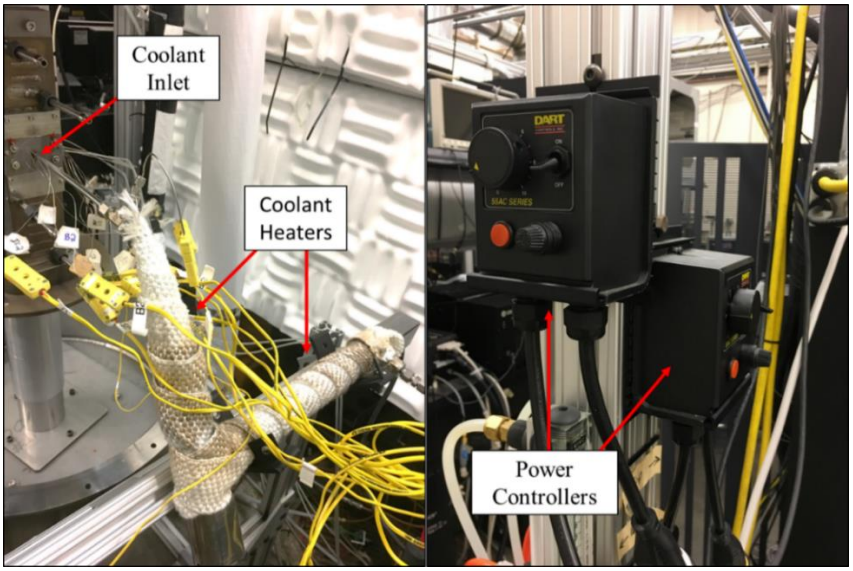

Figure 24. OMEGALUX heaters (left) and power controllers (right).

3.2. Film Cooling Rig Test Section and Changes

The FCR is an engine scale rig that is able to perform both high and low temperature testing and is capable of using different gases to achieve different flows through the test section. The rig was designed and built with modularity to allow easy changes of which many have occurred throughout its lifespan. To achieve the objectives of this thesis work, as well as to address issues observed in previous work, the FCR test section, shown in Figure 25, underwent changes that can be grouped into three categories: changes to the mainstream

components, changes to the test block, and changes to the viewport assembly. Changes made to the mainstream components, include modifications to the main block, creation of a transition wedge, and creation of a blockage adjustment component which will be discussed in Section 3.2.1. Changes to the test block include a redesign of the test airfoil, a redesign of the coolant delivery block, and implementing a new impingement plate component which will all be discussed in Section 3.2.2. Finally, the updates to the viewport will be discussed in Section 3.2.3.

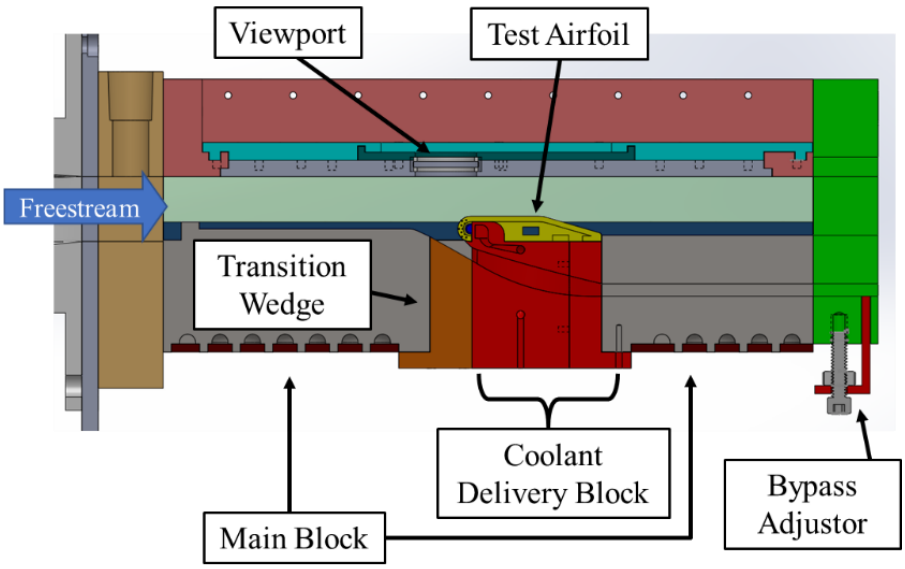

Figure 25. FCR test section.

3.2.1. Main Flow Components

Changes to main flow components were motivated by two issues. The first motive was to support the first thesis objective which required matching Bryant's [11] experimental setup. The second motive was to address a potential errant conduction path in the previous rig design. Notable differences in overall effectiveness were observed in previous tests performed with matched nondimensional parameters at different temperatures. Figure 26 shows the overall composition of the previous FCR test section design used in the work

completed by Ashby [16] and Vorgert [34]. The following will discuss the details of the main flow path components from previous work and then discuss how they were modified or replaced.

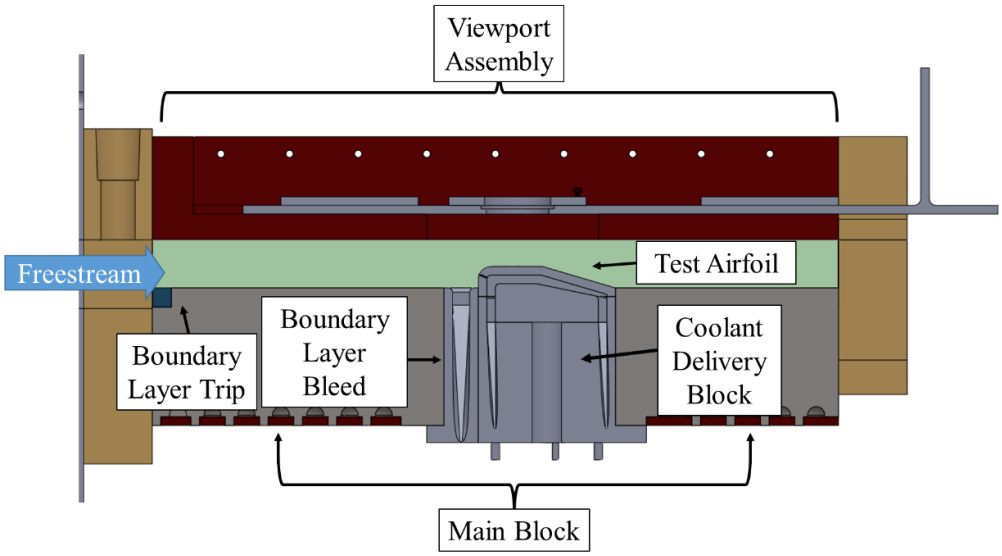

Figure 26. Previous FCR test section design.

As shown in Figure 26, the main flow path was formed between the mainblock and the viewport assembly. The main block was designed to support interchangeable test articles. In the experiments conducted by Ashby [16] and Vorgert [34], they used half airfoil test articles mounted to the floor of the test section. It was in this configuration that Vorgert examined the resulting overall effectiveness on the flat portion of the test airfoil in two different temperature regimes. In his examination, he found that while using similar blowing ratios, density ratios, and freestream Reynolds numbers the overall effectiveness results measured in the higher temperature regime were consistently higher than the low temperature results. While he offered some possible reasons for these results such as unmatched *Bi* or unmatched advective capacity ratio (ACR), the prevailing theory for this occurrence was that an unaccounted for conduction path existed between the model and the laboratory

surrounding. Since the model was part of a large test block, a conduction path existed through this block that would not exist in a true engine experiment. At the higher temperatures, more heat was lost via this route resulting in lower surface temperatures and thus higher overall effectiveness.

To address the conduction issue and to bring the configuration of the FCR closer to Bryant's [11] experimental setup, a bypass channel was introduced to the rig. This decision was made for two primary reasons. First, a bypass channel would enable improved control over the location of the stagnation point. While it would be ideal to simply create a full wind tunnel test section to stick the model into, that would double the required freestream mass flow to reach the target freestream conditions. The bypass channel avoided the need to double the flow rate while still utilizing a pseudo full wind tunnel configuration. The second reason for introducing the bypass channel was that it would physically separate the model from the bottom wall reducing the paths of conduction available. By allowing the freestream to pass beneath the model symmetric heating would occur. The following will discuss the design changes to implement the bypass channel and other related changes to the main flow components.

Before simply creating a channel below the model, there were other design issues to consider. During his investigation, Vorgert compared the flow geometries of the FCR and Bryant's rig [34]. Through his examination, he found that the FCR test airfoil occupied a larger portion of the flow path compared to Bryant's setup. Invoking continuity, he reasoned that the acceleration of the flow over the model would be different between the two rigs. To mitigate this possibility, an additional design goal was to match the flow area contraction ratio, *CR*, of Bryant's rig determined by the ratio of the minimum flow area that occurs in

the test section, A_{TS}, to the flow area of the wind tunnel before the test article, A_{WT}. Figure 27 shows the head on views of the flow areas and the model for each rig. For the large scale rig, the wind tunnel test cross-sectional area was constant and based on the height, h_{WT}, and width, W, shown in Figure 27. A_{WT} for the large scale rig was equal to 1494.1 cm^2. The minimum test section cross-sectional area is considered to be the sum of the areas shaded in white for the large scale rig. A_{TS} was equal to 1133.1 cm^2 for the large scale rig which resulted in a CR of 0.76. Since the small scale rig previously employed a half-wind tunnel scheme, the original contraction ratio (dimensions not shown in Figure 27) was based on the area above the test airfoil compared to the area of the channel ahead of the model and was calculated to be 0.44. To improve the situation, the height above the model needed to increase. In practice it was easier to lower the position of the model in the test section and maintain the upper wall. Figure 28 shows the positioning of the test airfoil in both the old and the new configuration.

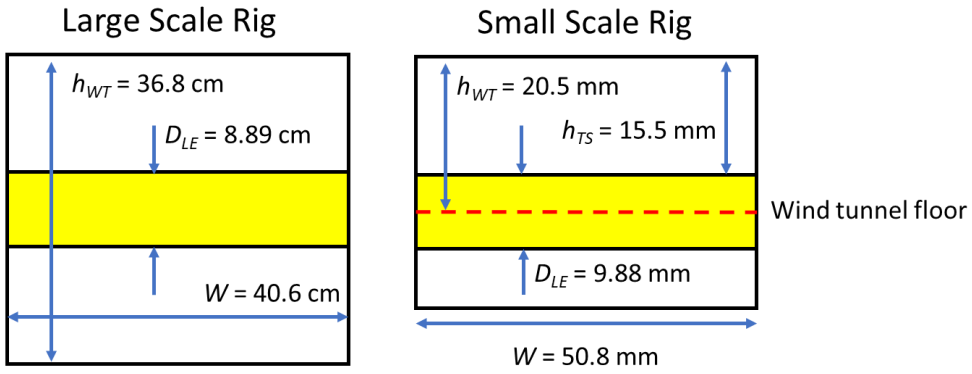

Figure 27. Head on view of rig flow areas.

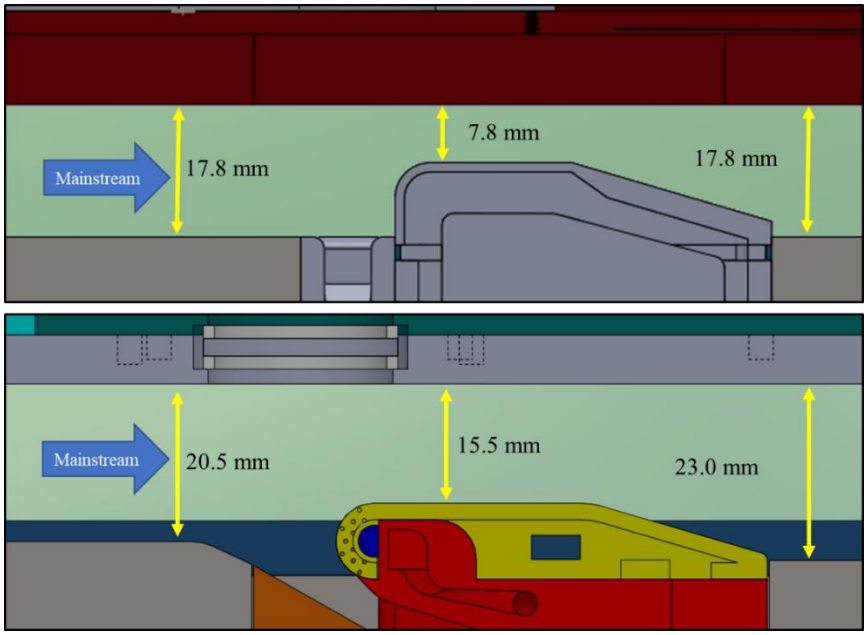

Figure 28. Previous (top) and current (bottom) test section side views.

Simply lowering the model, however, created an additional issue. Without also adjusting the channel height ahead of the model, the desired stagnation point on the leading would fall below the approaching wall. Therefore, the approaching channel height had to be reduced as well. After going through some design iterations, the final approach channel height chosen was 20.5 mm, which lined the bottom wall up with the height of the stagnation row, and resulted in an A_{WT} of 1041.4 mm^2. The height above the model was chosen to be 15.5 mm, as shown in Figure 28, and resulted in an A_{TS} of 787.4 mm^2, based on achieving a *CR* of 0.76. Since the new configuration includes a bypass channel, 0.76 is the minimum achievable *CR* and assumes that no flow passes through the bypass channel. The bypass channel will be discussed in more detail further in this section.

Of course, increasing the approach channel height, or lowering the test section floor, was not without its own issues. By lowering the test section floor, the boundary layer trip, introduced first by Shewhart [39] and highlighted in Figure 26, would be reduced from 7.0

mm high step to a 4.3 mm high step. The boundary layer trip was an important feature to ensure a consistent turbulent flow regime. This enabled previous students to predict the boundary layer growth on the approach using turbulent boundary layer correlations and the freestream Reynolds number based on the distance traveled from the trip. As shown in Figure 29, it was decided to leave a portion of the trip intact to ensure turbulent conditions in the test section. The final trip remained the original height but was reduced to 7 mm long with an additional step afterwards. In this configuration, the approach boundary layer was expected to trip the turbulent flow while enabling a larger channel width downstream.

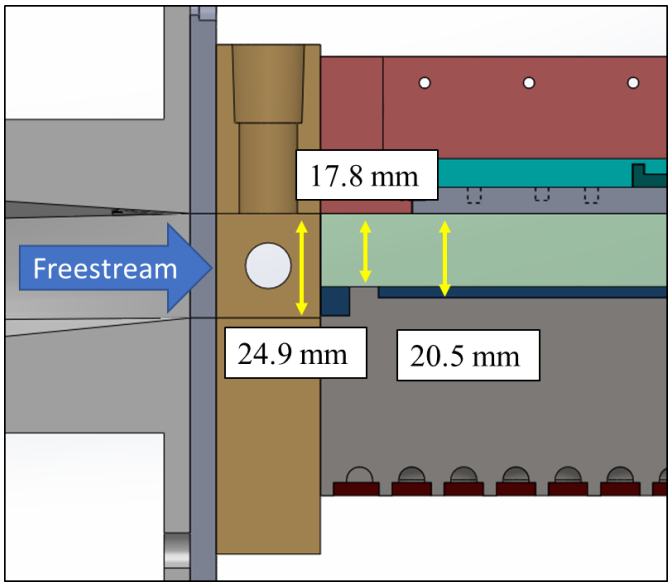

Figure 29. Entry of freestream into test section.

Additional changes to the upstream portion of the main block can also be seen in Figure 25. Since the goal was to introduce a bypass channel to divert flow below the model, the boundary layer bleed component was replaced with a transition wedge component, shown in Figure 30, to provide a transition from the main flow path to the bypass channel in the coolant delivery block (more discussion to follow in Section 3.2.2). The wedge had a slightly larger form factor compared to the boundary layer bleed component requiring some material

to be removed from the approach side of the main block to accommodate the new component. Finally, the end of the approach was beveled at 25˚ to match the slope of the transition wedge.

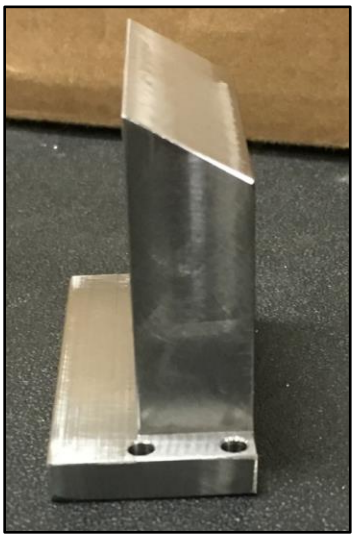

Figure 30. Transition Wedge

The remaining modification to main block was the creation of the bypass channel in the aft portion of the main block. The bypass channel was designed with a constant area equal to about one-fourth of the area over the test airfoil, which was about 217 mm^2. To produce this area, the channel was designed with a height of 4.88 mm and a width of 44.5 mm for the entire length of the aft block measuring 82.6 mm. Though this design modification was thought to be simple, it turned out to be a difficult feature to machine without special equipment. While most of the modifications to the main block were made by the AFRL model shop, the task of machining the bypass slot was left to a specialty machine shop. To make the slot to design specifications, the part was sent to Trifecta Tool & Engineering where they used sinker electrical discharge machining (EDM) to bore out the slot. The fully modified block is shown in Figure 31.

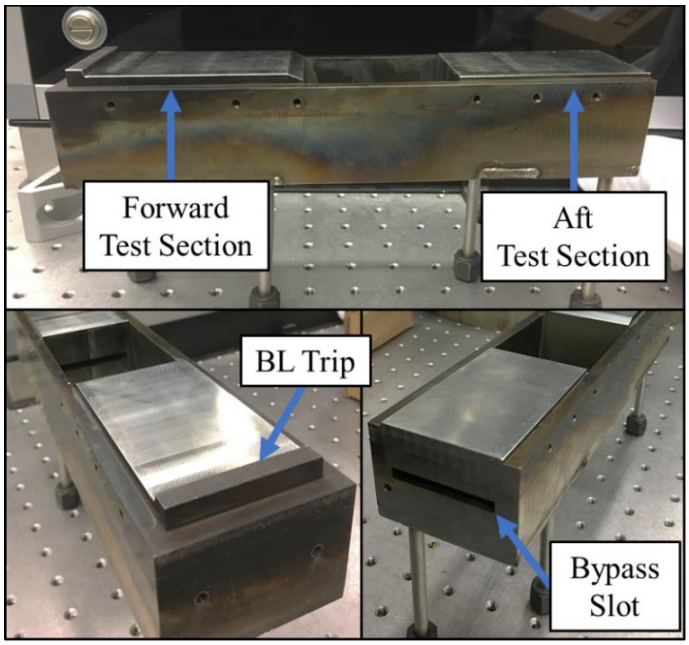

Figure 31. Modified main test section block.

The final main flow was a new variation of the upper bracket component which connected the main block and the viewport assembly and also included the exit channel for the FCR. The bypass blockage adjustor, shown in Figure 32, also serves as the exit for the bypass channel and includes a blockage gate to adjust the area of the bypass channel exit. The blockage gates position was adjusted via a set screw which gives fine control of the position of the gate but does not currently indicate the positioning of the gate. Ultimately, the purpose of the bypass blockage adjustor was to give some control over the stagnation point by adjusting the amount of air that passed through the bypass.

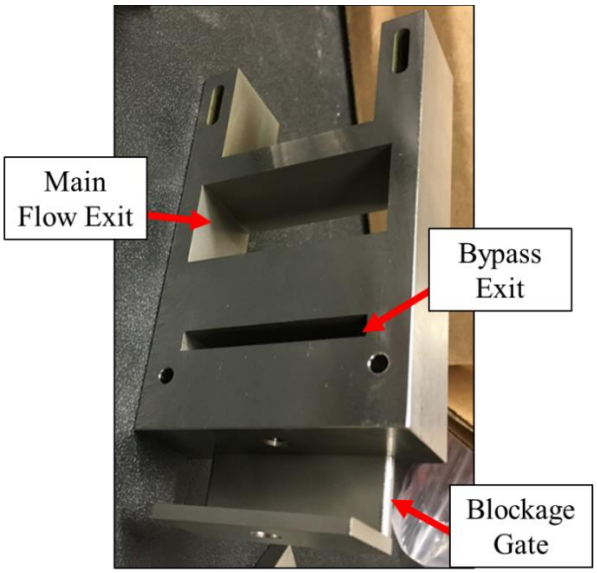

Figure 32. Bypass blockage adjustor.

3.2.2. Test Block Changes

With the freestream flow configured to create the proper constriction, the following will discuss the changes made to the test block. First, the changes made to the test airfoil are outlined. Next, a discussion on how the new coolant delivery block supplies coolant to the test airfoil as well as some of its other new features, including the integration of the new bypass channel. Finally, the details on the impingement plate used to modify the internal cooling configuration are covered.

Previous experiments conducted in the FCR by Vorgert [34] and Ashby [16] each used quarter-cylinder leading edge models with varied numbers and locations of film cooling holes. Before them, Shewhart [39] and Lynch [43] used flat plate specimens with varied hole patterns. For this thesis, one of the main objectives was to examine the effect of geometric scaling on film cooling results. As such, design work focused on scaling down the large scale model used by Bryant [11] so that data obtained from both models could be compared.

Figure 33 highlights the dimensions important to matching and scaling the geometry of the semi-cylinder leading edge model used by Bryant, including the full coverage, showerhead film cooling scheme. In order to fit Bryant's model design into the FCR test section, the dimensions of the large scale model needed to be scaled down by a factor of 9. The resulting scaled leading edge diameter, D_{LE}, was 0.988 cm with a constant wall thickness, t_{LE}, of 0.215 cm and a width, W_{LE}, of 5.08 cm, which is the standard width used in the FCR and not a scaled value. The full coverage showerhead film cooling scheme used by Bryant was also matched and scaled for this experiment. The scheme consisted of seven staggered rows of six holes each along the span of the leading edge with the middle row placed on the expected stagnation point. Scaling the coolant holes by a factor of nine required that the diameter, d_{LE}, be 0.533 mm; however, due to manufacturing limitations, the coolant holes were made slightly larger. The actual diameter of the holes varied between 0.584 mm at the inner radius of the leading edge to 0.622 mm at the outer radius of the leading edge which resulted in a 17% miss in the target coolant hole diameter. This taper was unplanned but was a result of some shaking that occurred during the manufacturing process because the bit was unconventionally small. The ratio of the leading edge to coolant hole diameter, D_{LE}/d_{LE}, was 15.88 which was also about a 17% mismatch with Bryant's model. The film cooling holes were spanwise oriented with an injection angle, γ, of 20˚ angle producing a hole length, L, of 0.624 cm. The length to diameter of the coolant hole ratio, L/d_{LE}, was 10.03 which is also a 17% mismatch with Bryant's model. The angular spacing between the rows, β_{LE}, was 21.5˚ while the spacing between holes in the same row, P, was 0.422 cm. Internally, the leading edge was designed to accept an impingement plate (discussed in more detail later) and ensures a constant gap height, g, of 0.711 mm, which is the distance between the

impingement plate and the inner radius of the leading edge. The parameters of Bryant's design and the design used for this work is summarized in Table 1.

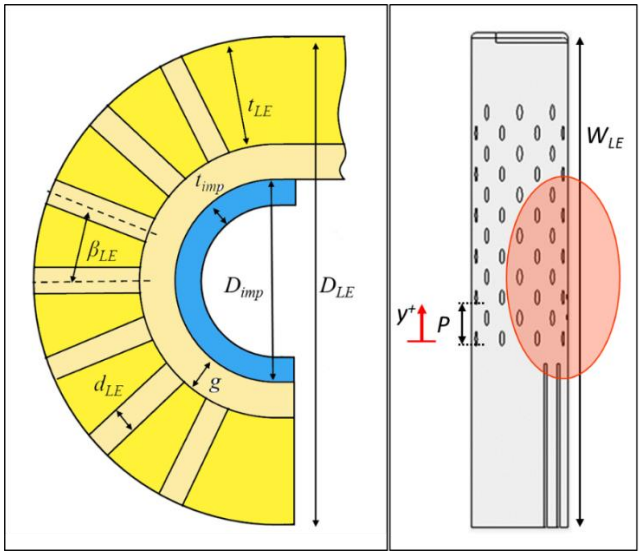

Figure 33. Leading Edge Design Views.

Table 1. Summary of leading edge dimensions

Parameter	Large Scale	Target Scaled Value	Actual Value	Actual Scaling Factor
β	21.5˚	21.5˚	21.5˚	N/A
γ	20˚	20˚	20˚	N/A
d_{LE}	0.48 cm	0.533 mm	0.622 mm	7.7
D_{LE}	8.89 cm	0.988 cm	0.988 cm	9.0
D_{LE}/d_{LE}	18.52	18.54	15.88	N/A
L_{CH}	5.61 cm	0.623 cm	0.624 cm	9.0
L_{CH}/d_{LE}	11.63	11.69	10.03	N/A
P_{LE}	3.78 cm	0.42 cm	0.422 cm	9.0
t_{LE}	1.93 cm	0.214 cm	0.214 cm	9.0
g	0.64 cm	0.71 mm	0.71 mm	9.0

The positioning of the coolant holes on the leading edge was influenced by the achievable view of the IR setup, indicated by the red oval region in Figure 33 and discussed further in Section 3.3.2. Therefore, the coolant holes were drilled such that the first hole of each observable row could be viewed by the IR camera. While this was the main consideration for the spanwise positioning of the coolant holes, the location of the hole termination on the inside of the leading edge also needed to be considered. If the holes were

placed too far to the right of the model, the coolant holes would pass through the side wall of the leading edge.

The model was manufactured by the Mound Manufacturing Center using Inconel 718, which was a departure from previous experiments that used Hastelloy® X for the models. The reason for switching materials was motivated by the thermal scaling work of Stewart and Dyson [3]. By making the switch of materials, these experiments hoped to further examine the thermal scaling behavior of Inconel 718 between low and high temperatures. In their investigation, Stewart and Dyson were able to show analytically and experimentally that a test article made of Inconel 718 could be used to enable approximate *Bi* matching between low and high temperature tests.

As emphasized earlier, a main objective of this thesis was to scale down the experimental setup used by Bryant [11]. This included matching the manor of delivering coolant to the model. Bryant's coolant delivery setup is shown in Figure 34. Initially, a simply scaled down version of Bryant's soaker hose coolant delivery system was envisioned; however, the FCR does not have nearly the same access to the test block as Bryant had in her rig. Additionally, the introduction of the bypass channel (discussed previously in Section 3.2.1) further limited the ability to simply scale her design. The final design of the assembly is shown in Figure 35.

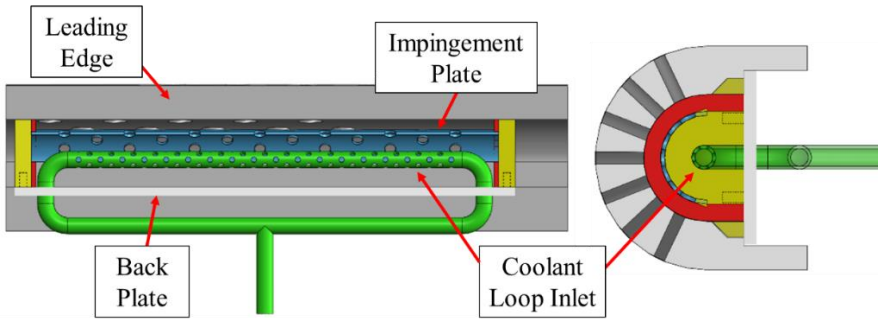

Figure 34. Bryant coolant delivery setup.

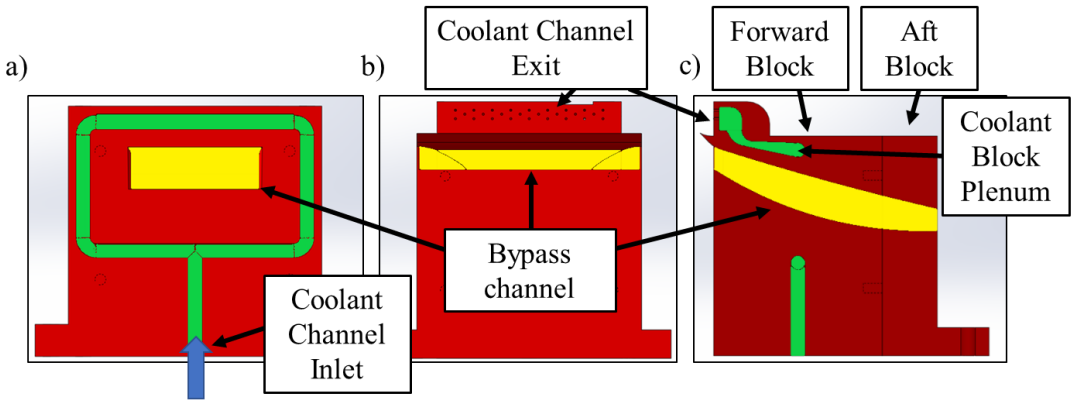

Figure 35. Views of coolant delivery assembly.

The coolant block assembly was comprised of two pieces, a forward and an aft piece. The coolant enters the rig through the forward block through a passage on the bottom of the block as shown in Figure 33a. As the coolant progresses through the block, the passage splits into two which then wraps around the bypass channel to feed a plenum shown in Figure 33c. This plenum then feeds a second plenum between the coolant block and the leading edge, similarly to what was shown in Bryant's setup. A series of 26 holes with a diameter of 0.51 mm was established to distribute the coolant out of this plenum in similar fashion to the holes seen exiting the green tube in Figure 34. Though not an exact scaled replica of Bryant's coolant delivery system, this design is believed to fulfill the same purpose which is to evenly distribute coolant to the leading edge plenum.

Besides just delivering coolant to the model, the coolant delivery assembly was designed with a few more purposes in mind. First, the assembly was designed in two pieces so that instrumentation channels could be easily accessed when the blocks were disassembled. Additionally, each piece was designed with a constant area channel, which matched the area of the channel in the main block, to support the new bypass channel. The assembly also served as the mount for the test airfoil and contained holes through which rods attached so the leading edge model could pass.

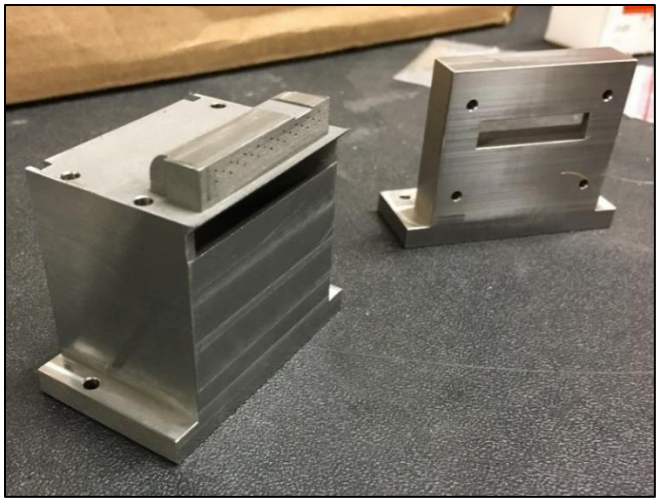

Figure 36. Printed forward and aft coolant delivery blocks.

The final test block component is the impingement plate. As previously discussed in Section 2.4.2, impingement cooling is a form of internal cooling commonly employed on turbine components. In Bryant's experiments [11], an objective was to examine the contributions of the different forms of cooling: internal, external, and hole cooling. She attempted to understand the effect of internal cooling on her test article by testing multiple internal cooling configurations and comparing the resulting overall effectiveness distributions. This was accomplished by using a series of thin semi-cylinder plates with different hole arrays placed between the leading edge and the coolant supply to create impingement jets of different strengths and acting in different locations.

For this experiment, a scaled down version of Bryant's 46-hole impingement plate configuration was attempted, shown in Figure 37. While Bryant provided all the necessary dimensions in her work to scale down this component, the diameter of the impingement plate and the diameter the impingement holes were misreported. It would later be discovered that the actual diameters were two times the reported diameters, which were reported as 1.94 cm for the plate diameter and 0.32 cm for the hole diameter. The correct values were later

discovered to be 3.88 cm for the impingement plate diameter and 0.64 cm for the impingement hole diameter. Table 2 summarizes the actual dimensions of Bryant's impingement plate design and the final dimensions of the small scale rig's impingement plate.

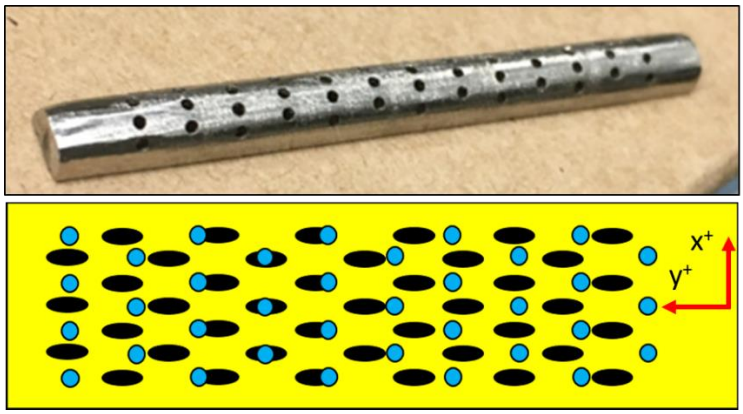

Figure 37. Printed impingement plate (Top) and hole alignment (Bottom).

Table 2. Summary of impingement plate dimensions

Parameter	Large Scale	Target Scaled Value	Actual Value	Actual Scaling Factor
d_{imp}	0.64 cm	0.71 mm	0.71 mm	9.0
d_{LE}/d_{imp}	0.73	0.73	0.875	0.86
D_{imp}	3.88 cm	4.3 mm	4.2 mm	9.2
g	0.64 cm	0.71 mm	0.71 mm	9.0
t_{imp}	0.05 cm	0.5 mm	0.5 mm	1
β_{imp}	21.5˚	21.5˚	21.5˚	1
P_{imp}	3.78 cm	0.42 cm	0.54 cm	7

Initially, the reported values of Bryant's model were used to create a $1/9^{th}$ scaled impingement plate. The exception was the thickness of the impingement plate, t_{imp}, which was not scaled down and remained at 0.5 mm to ensure that the component could retain its shape while being installed. The misreporting of the plate diameter led to a scaled design that was obviously wrong with the diameter of the impingement plate being much smaller than expected. Despite being unsure why the scaled model was smaller than expected, the intent in the initial design was understood. Therefore, the impingement plate diameter, D_{imp}, was

altered to ensure a scaled gap distance, g, of 0.71 mm between the impingement plate and the leading edge, which was a scaled value anchored by its inclusion in the design of the leading edge. The value determined for D_{imp} through this method was 4.2 mm which had a scaled value of 4.6 of the reported diameter. Using the true diameter from the actual large scale D_{imp}, this resulted in a 9.2 scaled value.

The scaled impingement hole diameter, d_{imp}, was 0.36 mm based on the reported diameter, also creating a scaling issue. From the d_{imp}, the hole spacing was derived using the reported ratio of hole spacing to impingement hole diameter. The result of this produced holes that were laterally spaced too far. Another attempt was made to alter the design by reducing the lateral hole spacing to ensure that the impingement holes lined up between the coolant hole entries. A pitch spacing, P_{imp}, of 0.54 cm was used with an angular hole spacing, β_{imp}, of 21.5˚. During the data analysis, it was discovered that the pitch spacing was still slightly larger than desired which caused some partial overlapping of holes are seen in Figure 37. The coolant hole entries are represented by the black holes while the impingement holes are colored blue.

By the time the scaling error was realized, the impingement plate had already been made according the dimensions in Table 2. A comparison of the diameters showed that the outer plate diameter was close to what it should have been but the impingement holes were smaller than they should have been. At the time, it was believed that expanding the impingement holes would bring the scaled impingement plate to within the correct dimensions. Therefore, the holes were expanded to the correct diameter of 0.71 mm by drilling out the remaining material. The final ratio of leading edge coolant hole diameter to

impingement plate diameter, d_{LE}/d_{imp}, was 0.87. However, this did not account for the improper pitch spacing.

3.2.2.1. Prediction of Internal HTC

Bryant [11] used jet correlations developed for different nozzle size and arrays to estimate the average internal convective heat transfer coefficient based on the average Nusselt number. The correlation, shown in Equation 32, was for a staggered jet array like shown in Figure 38 where *K* and *G* are functions of the relative nozzle area, A_r, and the ratio of the gap spacing to the jet diameter, *H/D*.

$$\frac{\overline{Nu}}{Pr^{0.42}} = 0.5 * K\left(A_r, \frac{H}{D}\right) * \mathrm{G}\left(A_r, \frac{H}{D}\right) * Re^{2/3} \tag{32}$$

where

$$K = \left[1 + \left(\frac{H/D}{0.6/A_r^{1/2}}\right)^6\right]^{-0.05} \tag{33}$$

$$G = 2A_r^{1/2}\frac{1 - 2.2A_r^{1/2}}{1 + 0.2\left({}^{H}/_{D} - 6\right)A_r^{1/2}} \tag{34}$$

$$A_r = \frac{\pi D^2}{2\sqrt{3}S^2} \tag{35}$$

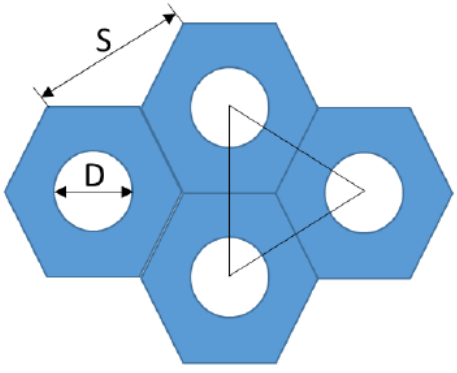

Figure 38. Impingement plate geometry for a staggered array of holes [11].

Using the same approach, the predicted average internal heat transfer coefficients (HTC) for this investigation were calculated for the planned testing conditions summarized in Table 8 of Section 4.2. Figure 39 shows the predictions at different blowing ratios according to the planned freestream Reynolds number and coolant temperature. The figure shows that the HTC increases with increasing blowing ratio in all cases. Additionally, the results show that despite some of the cases having matched freestream Reynolds number, the temperature difference in the freestream, and also the increase in coolant mass flow to achieve *M*, cause these lines to have an offset. Figure 40 compares the predicted HTCs and confirms that there is an offset for the cases with matched freestream Reynolds number and different coolant temperatures. The maximum observed difference was for the high freestream Reynolds number case which peaked at about 60 W/m^2-K. Figure 40 also compares HTCs produced by cases using the same coolant temperature but different freestream Reynolds number. The observed differences for these cases are much greater than the matched freestream Reynolds number cases. The maximum observed difference overall was for the high temperature case with mismatched Reynolds number at about 155 W/m^2-K.

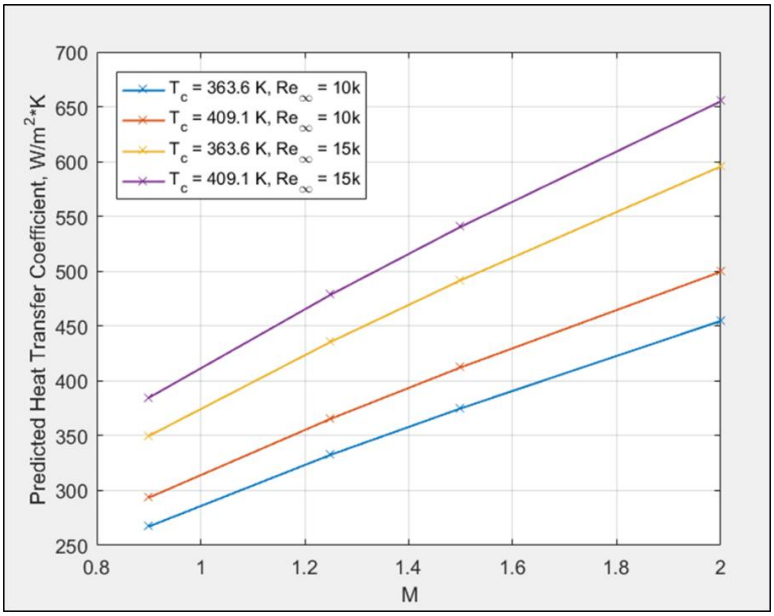

Figure 39. Predicted internal HTC using impingement plate.

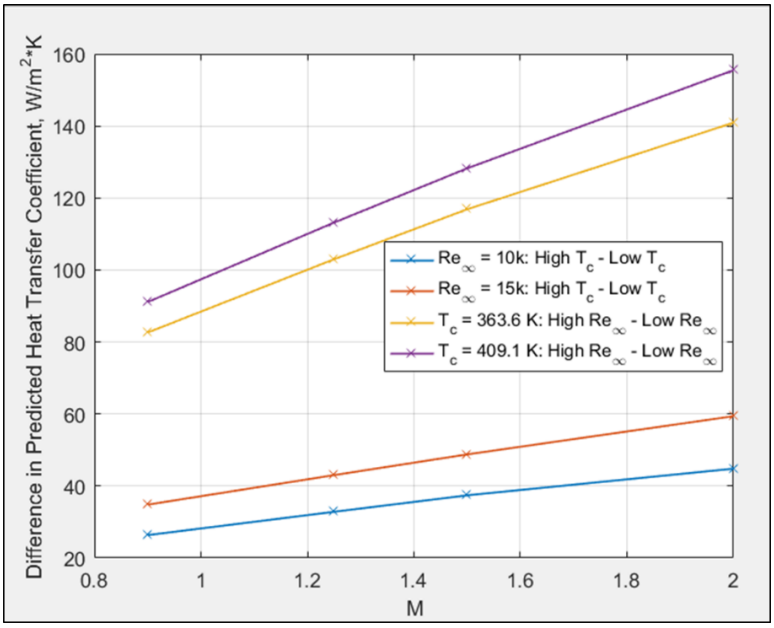

Figure 40. Comparison of predicted internal HTC using impingement plate.

3.2.2.2. Manufacturing and assembling

For this experiment, there were many updates to the rig which required many parts to be modified or newly manufactured. As such, several entities assisted with the making and fabrication of parts. Overall, the AFIT model shop served as the primary integrator of the rig

and assisted in design verification. The test airfoil was manufactured by the Mound Manufacturing Center using Inconel 718. They manufactured some of the features into the model such as the notches in the bottom to accommodate routing of the leads out through the coolant block, the rod holes, and the heat flux passage as shown in Figure 41. The remaining features such as the coolant holes, the thermocouple holes, and the thermocouple trenches were fabricated by the AFIT model shop.

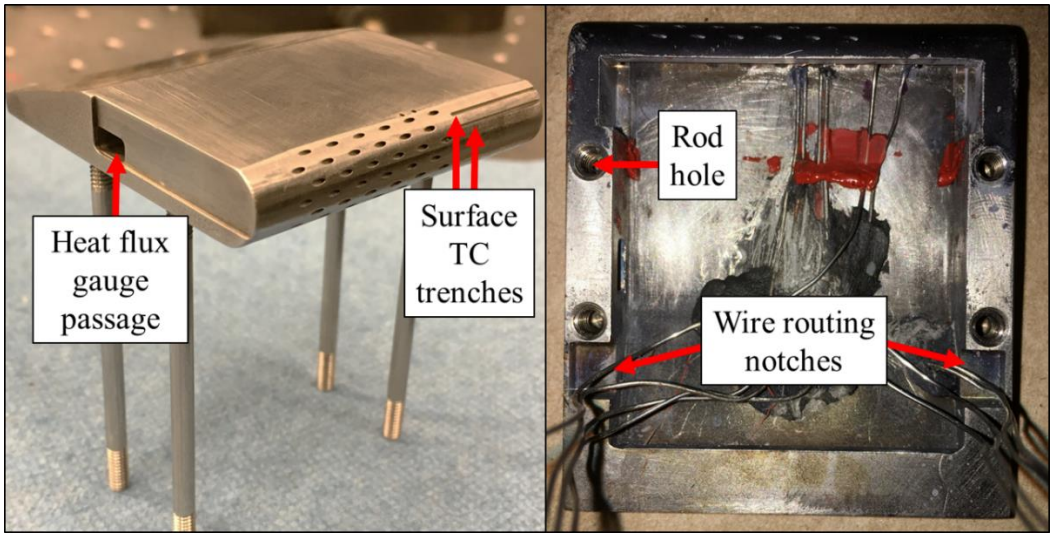

Figure 41. Test airfoil features.

The coolant blocks were 3D printed by Bastech Inc. out of 17-4 stainless steel. The blocks were created using direct metal printing, which is a process that uses lasers to melt powdered metal fusing the molten metal into a solid part one layer at a time. The decision to print the parts was mainly due to the complexity of the forward coolant delivery block as discussed in Section 3.2.2. Once the blocks were printed, the AFIT model shop machined them to fit properly together and within the main block. The impingement plate was also 3D printed out of Inconel 718 at AFIT. As discussed earlier in Section 3.2.2, the holes also needed to be expanded which was done by the AFIT model shop.

While the manufacturing of the leading edge model and printed coolant delivery block progressed well, dimensions in this project were so small that a slight imperfection in manufacturing led to a partial obstruction of film cooling holes as shown in Figure 42. After assembling the test section, it was discovered that the last row of film cooling holes on the bottom side of the model was partially blocked by the lip of the coolant delivery block. Using a combination of a rotary tool and a metal file, the lip was shaved down to unblock the holes. In the process of unblocking the holes, an attempt was made to understand how this blockage affected the coolant distribution by collecting data with and without the holes blocked; however, the tests were inconclusive.

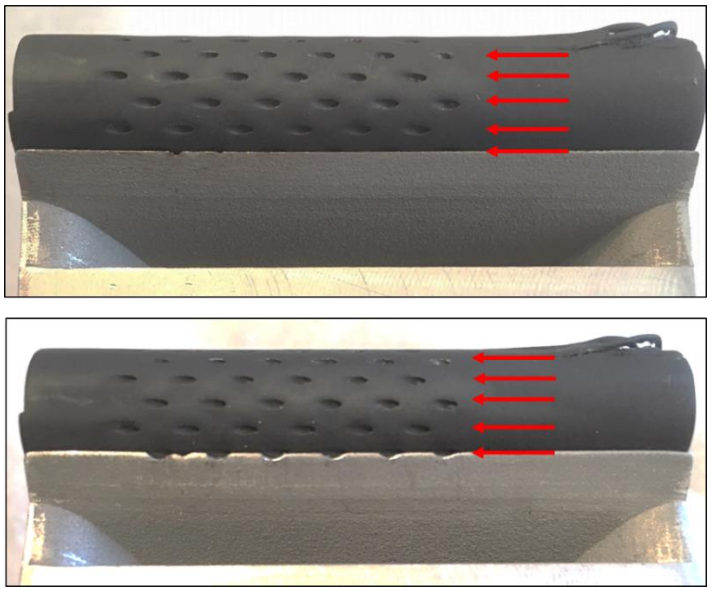

Figure 42. Leading with holes block (Top) and with holes unblocked (Bottom).

During the period when the new components were being made, plastic versions of the coolant delivery assembly and the test airfoil were printed using AFIT resources. The components can be seen in Figure 43. This was done to aid in planning the layout of the instrumentation and to get a better sense of the actual size of the components. Through this initial work, the routing pathways for instrumentation were established. Additionally, the

plastic parts were also used to aid with IR shakedown testing which enabled planning for where the IR camera needed to be positioned. The plastic parts also aided in identifying that transition wedge component was initially manufactured incorrectly. Fortunately, the issue was discovered before all the components were finished and had no impact on the testing schedule.

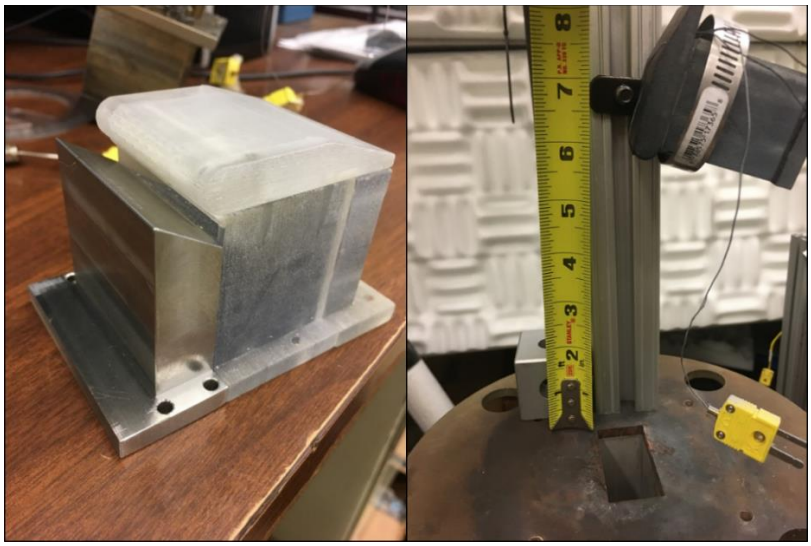

Figure 43. Printed plastic components used for initial experimental setup planning and testing.

3.2.3. Viewport Changes

The final component changes for the FCR were modifications to the viewport. The viewport gave optical and IR access to the test airfoil through a circular window, which could be made of a number of materials including sapphire, quartz, or even silicon. For the purposes of this work, the viewport was used to view the leading edge of the model to perform thermal imaging with an IR camera and therefore required the integration with a sapphire window. The main driver for the redesign of the viewport assembly was an issue identified early in the setup of these experiments. While examining the viewport, it was discovered that the previous design had a large void directly above the test article, as shown in Figure 44. This

void measured 9.5 mm deep by 25.4 mm wide by 63.5 mm long. While previous works do not comment specifically on why the void was so large, it is believed that the depth resulted from both installing a sliding mechanism to hold the window while needing to protect the window while testing in the high temperature regimes. The width corresponded to the diameter of the window which was 25 mm. The length allowed the window to be easily shifted to obtain the correct view needed. However, this void also changed the contraction ratio of the flow over the model. The importance of setting this properly was understood leading to a need to reduce the void. However, any new design still needed to allow the correct viewing of the leading edge model.

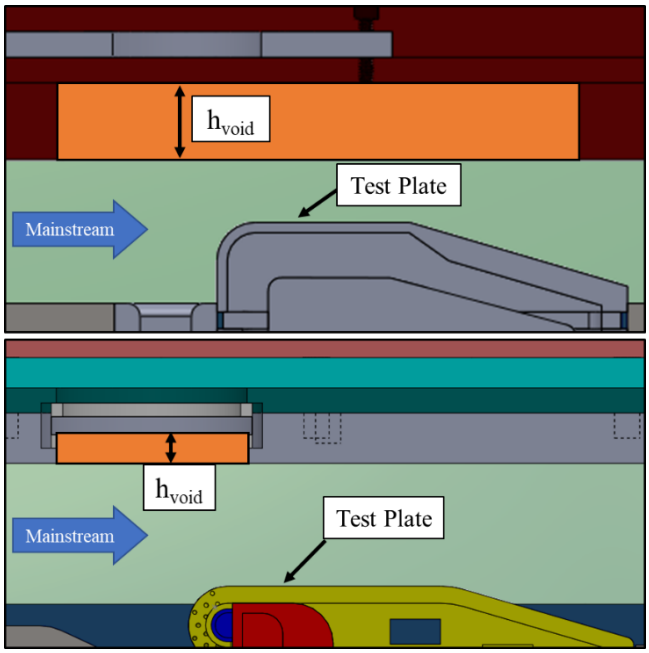

Figure 44. Original (Top) and new (Bottom) void cross sectional views.

While unable to completely remove the unaccounted for region, the new IR viewport assembly reduced the region from a 9.5 mm deep rectangular region to 3.6 mm deep circular region (diameter of 24.1 mm), shown in Figure 44. The void was also moved forward to not impact the flow over the model as significantly. In the FCR, experimental flow calculations

rely on knowing the cross-sectional areas of the flow path along with the mass flow and temperatures to fully define the flow. While the exact velocity profiles in the rig have never been determined, these calculations have relied on knowing the bulk velocity. However, the impact of this additional flow region above the test article has not been accounted for in past experiments. While this may not have caused a large impact on previous results, this investigation's desire to match the flow distribution over the model to that of Bryant [11], makes reducing this region's volume important.

Overall, a reduction from 15.3 cm^3 to 1.7 cm^3 was accomplished by modifying the previous design which used a sliding plate to obtain the different views required. For the new modified viewport, a clamping design was implemented and shown in Figure 45. This was accomplished by introducing three new parts and salvaging part of the old viewport assembly. The first new part, referred to as the bottom plate, was designed to fit on the bottom side of the main viewing block, or the side facing the test article. This part was the actual component used to minimize the void above the test section and contained the circular hole for a window to achieve line-of-sight access. The second new part, referred to as the window plate, was designed to hold and sandwich the 25 mm diameter sapphire window against the bottom plate. When assembling these components, a bead of high temperature RTV was used to seal the window. Finally, the third new part, referred to as the sealing plate, ensures that viewport assembly does not allow flow to leak out of the front of the rig and helps to secure the bottom plate into place. The components used in this investigation are shown in Figure 46.

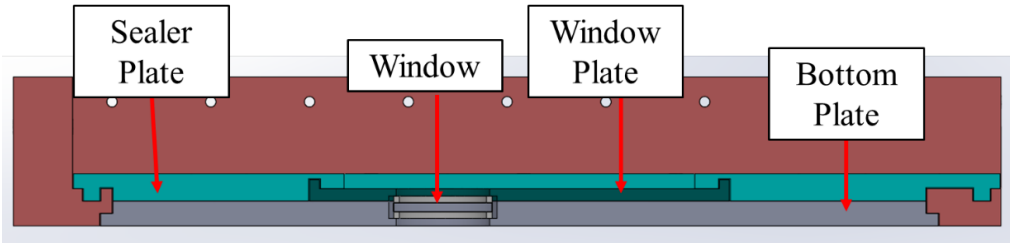

Figure 45. IR viewport assembly.

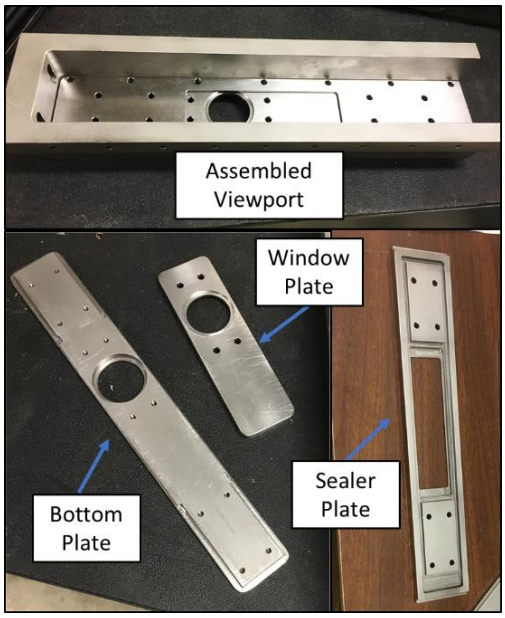

Figure 46. IR viewport components.

Because this new design is a clamping design, the location of the window cannot be adjusted without switching both the bottom plate and the window plate, and potentially the sealer plate as well. Therefore, three window configurations, shown in Figure 47, were designed for use in this assembly. The first design was a blank bottom plate design. This design completely rids the void created by the viewport but blocks optical access from the front of the rig. This would be ideal for any testing where front viewing of the test article was not needed. The second design provides an 85˚ view of the flat afterbody. The location of the window is shifted downstream to enable viewing of the downstream section. The angle was set to reduce the likelihood of the IR camera seeing its reflection off the window. The third design, which was the window configuration used in these experiments, was designed

to give a 45˚ view of the leading edge. To obtain a better view of the stagnation line,the camera had to be repositioned to about a 65˚ angle as shown in Figure 48.

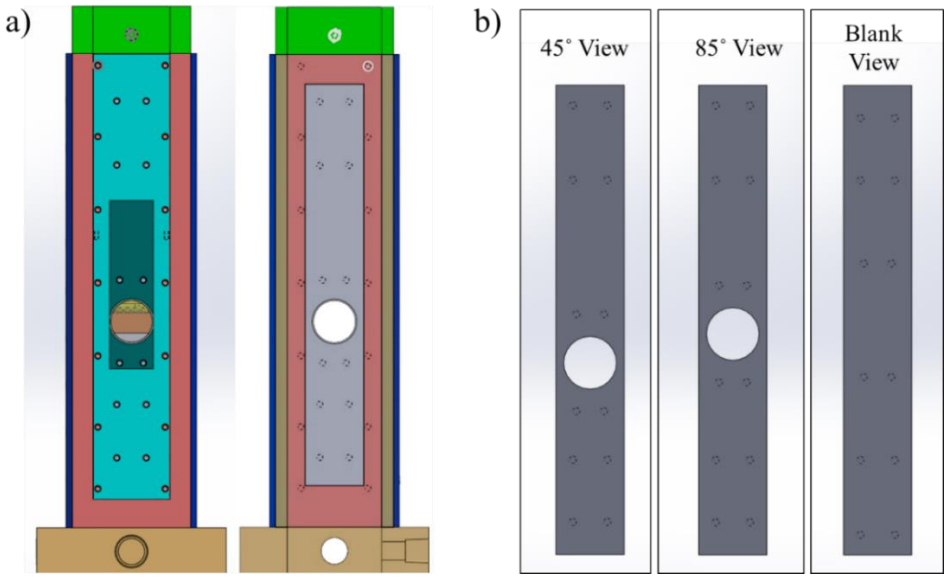

Figure 47. a) Assembled IR viewport (front and back) b) Bottom plate designs viewport designs.

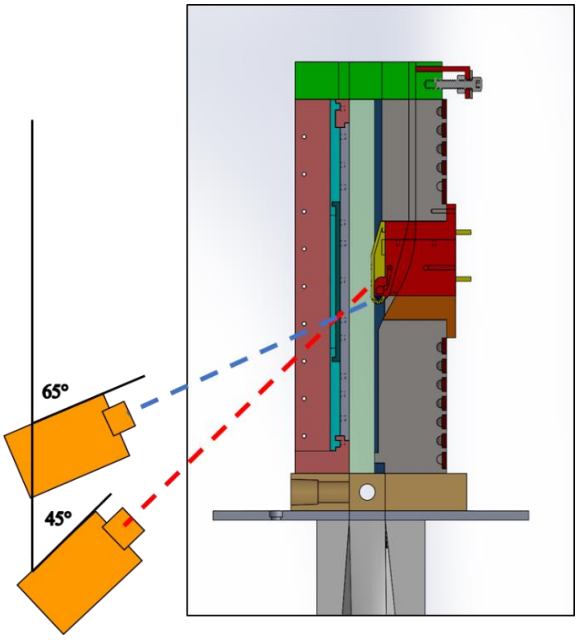

Figure 48. Notional IR camera setups to get views of the flat afterbody (45˚ view) and the leading edge (65˚).

3.3. Test Setup

The following will review the measurement equipment and techniques used to conduct this thesis work. Section 3.3.1 will briefly discuss how the mass flow controllers (discussed earlier in Section 3.1.1) were used to set the desired mainstream and coolant flow rates. The thermocouple layout and the IR thermography setup used to perform thermal measurements will be discussed in Section 3.3.2. Finally, the work towards implementing double-sided heat flux gauges will be discussed in Section 3.3.3.

3.3.1. Mass Flow

There were two flows to manage in order to produce the correct testing conditions. The first was the mainstream flow, which was controlled and recorded via the modified LabVIEW program used by Vorgert [34]. The control inputs were based on a percentage of the full scale output of the controller. During preliminary testing, it was determined that the maximum flow rate that could be sustained was around 3.7 kg/min which was limited by the air source and not the mass flow controller. As mentioned, this was the limit determined for the AFIT shared air source. This flow rate was 0.1 kg/min short of the needed flow to hit a target freestream Reynolds number of 20,000 with the air heated to 600 K. For this examination, the highest setting used was 13.3% which provided a freestream mass flow of about 2.4 kg/min corresponding to a freestream Reynolds number of 15,000.

The second flow that was controlled was the coolant flow. A MKS MC20A, which was managed by a MKS Model 647 C multi gas controller, regulated this flow. The MC20A had the ability to command flow rates up to 50 SLPM. For the tests conducted in this investigation, this range was sufficient; however, tests conducted at higher freestream

conditions could require larger coolant mass flows which would require using a mass flow controller with a larger range. The factory reported accuracies for each mass flow controller are summarized in Table 3 which will be used for the uncertainty analysis in Section. 3.4.

Table 3. Summary of mass flow controller factory reported accuracies

Flow Path	**Controller Brand**	**Controller Model**	**Full Scale Flow Rate (SLPM)**	**Accuracy (% of reading)**
Coolant Supply	MKS	MC20A	50	± 1%
Freestream	Fox Thermal Instruments, Inc.	FT2	3400	± 1%

The mass flows were set according to the desired nondimensional parameters and temperatures targeted for each test. The freestream mass flow rate was dictated by the freestream Reynolds number based on the leading edge diameter and the temperature of the freestream flow. Recalling the definition of the mass flow rate (Equation 35), the Reynolds number can be rewritten in terms of the freestream mass flow rate, $\dot{m}_\infty$, the freestream dynamic viscosity, μ_∞, the leading edge diameter, D_{LE}, and the cross-sectional area of the test section just prior to reaching the transition wedge, A_{TS}. Since D_{LE} and A_{TS} are fixed geometric features, the only two variable inputs are the mass flow rate and the viscosity. Therefore, to determine the correct mass flow rate to use for a test, the freestream Reynolds number and viscosity, which was a function of temperature, must first be set. Once chosen, the target freestream flow rates were determined in this manner.

$$\dot{m}_\infty = \rho_\infty V_\infty A_{TS} \tag{36}$$

$$Re = \frac{\dot{m}_\infty D_{LE}}{\mu_\infty A_{TS}} \tag{37}$$

Once the freestream temperature and mass flow rates were determined, the coolant temperature and mass flow rate could be calculated. The coolant temperature was chosen to achieve the target density ratio. Invoking the ideal gas law, the density ratio can be rewritten in terms of pressures, temperatures, and gas constants. Assuming that the gases used are the same, which is the case in this investigation, and that they are at the same pressure, the density ratio becomes a function of the ratio of the gas temperatures as shown in Equation 38. With a chosen *DR* and freestream temperature, the coolant temperature is therefore set.

$$DR = \frac{\rho_c}{\rho_\infty} = \frac{P_c}{R_c T_c}\frac{R_\infty T_\infty}{P_\infty} = \frac{T_\infty}{T_c} \tag{38}$$

Finally, with the freestream temperature, the freestream mass flow rate, and the coolant temperature set, the coolant mass flow rate is the last quantity to be determined. For this investigation, the mass flow rate was set by the desired mass flux ratio. Again, recalling the definition of the mass flow rate, the density and the velocity can be replaced by the ratio of the mass flow rate and the flow path cross-sectional geometry shown in Equation 38. For the freestream flow, the cross-sectional area is still A_{TS}. The cross-sectional area for the coolant is the sum total of the coolant cross-sectional areas, A_c. The rewritten mass flux ratio is shown in Equation 39.

$$M = \frac{\rho_c V_c}{\rho_\infty V_\infty} = \frac{\dot{m}_c}{A_c}\frac{A_\infty}{\dot{m}_\infty} \tag{39}$$

3.3.2. Thermocouple and IR Thermography setup

This work used a combination of thermocouples and IR imaging to obtain thermal measurements within the test section. A series of thermocouples were installed to measure the temperatures of the freestream flow, the coolant flow, and the metal surface temperature. The freestream temperature was measured by a single 1.59 mm diameter Omega K-type

thermocouple at the entrance of the FCR test section, about 12.5 cm upstream of the test model, while internal coolant temperatures were measured using two 0.51 mm diameter K-type thermocouples as shown in Figure 49. These temperatures were used to set the desired *DR* and to determine the mass flows required for each test point based on the desired freestream *Re* and *M*. An additional 0.5 mm diameter thermocouple measured the coolant gas temperature before entering the leading edge plenum and was used to aid in understanding how the coolant gas temperature changed through the coolant block. Six 0.5 mm k-type thermocouples were used to measure the metal wall temperature of the leading edge and were anchored to the surface by Omega OB-200, which is a high temperature, high thermally conductive epoxy. Four thermocouples measured the external wall temperature of the leading edge which were used as reference temperatures for the IR calibration. Additionally, two of the surface thermocouples' locations corresponded to the location of the two internal leading edge thermocouples.

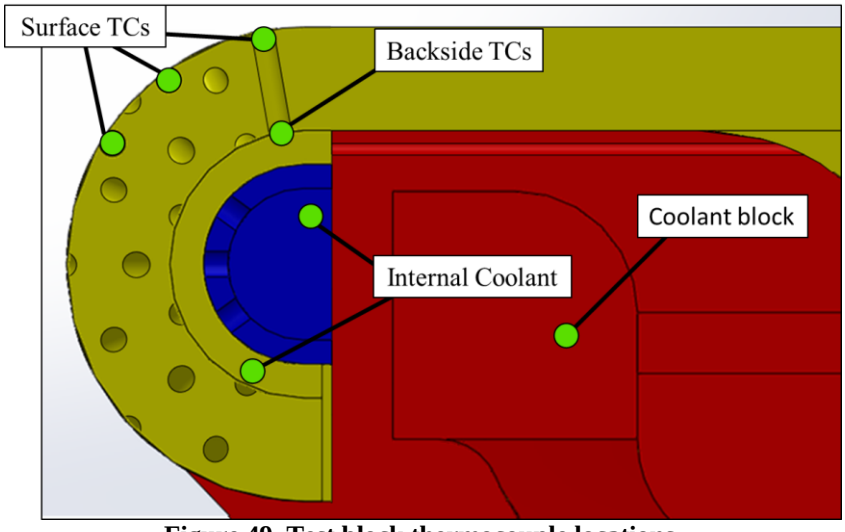

Figure 49. Test block thermocouple locations.

In addition to thermocouple measurements, thermal measurements of the test surface were made using a FLIR SC6700 mid-wave infrared thermal imager in conjunction with

FLIR's Examine IR software. Figure 50 shows the view of the leading edge obtained by the SC6700 through the sapphire window used in the FCR viewport. This setup allowed for the collection of radiative intensity data off of the model's surface while also keeping the four surface thermocouples referenced earlier in view (green dots in Figure 50**).** Keeping the four thermocouples in view was important for performing an in-situ calibration where both IR intensity values and surface temperatures were collected simultaneously. Additionally, the model was painted with high-temperature flat black paint to ensure a uniform emissivity and to reduce reflections off of the shiny metal surface.

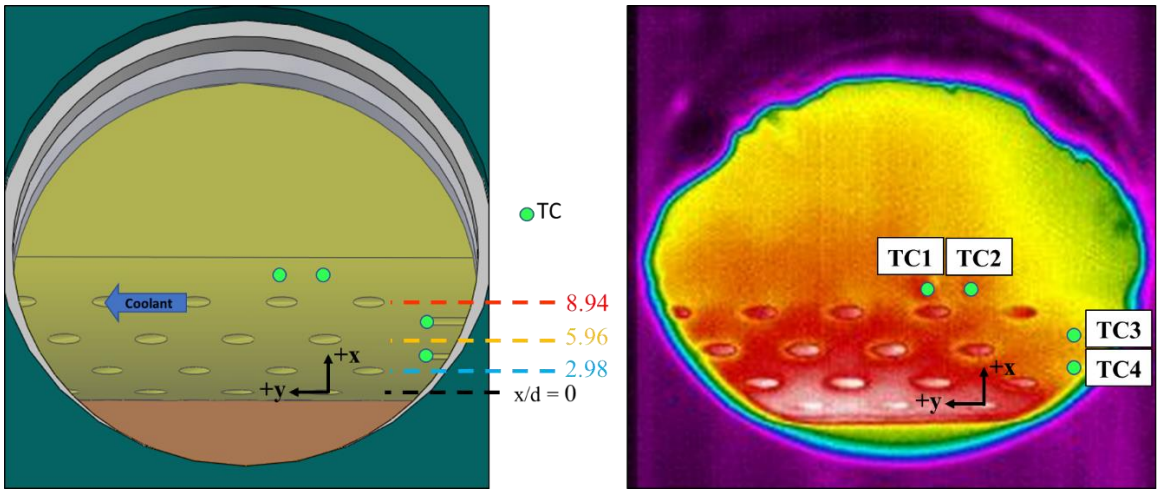

Figure 50. View of film cooling holes through IR viewport at 67°.

As was done in past experiments conducted by Ashby [16] and Vorgert [34] using the FCR, in-situ calibrations were performed to provide a means of converting IR intensity data to temperatures. IR intensities were collected with the SC6700 at a rate of 60 Hz for 2 seconds resulting in 119 thermal images. The intensity values for the 119 images were then averaged to produce a single frame. From that frame, intensity data from a box of pixels that spanned 2 pixels in either direction from the center of the thermocouple location were used to produce intensity data points for use in the calibration. In total, 25 intensity values were

averaged into a single value for each thermocouple location. This was done to ensure that a single value could not severely skew the data. Surface temperatures were also measured via the surface thermocouples at the same time of the IR intensity collection. During a single collection event, five temperature samples were made with the thermocouples via the LabVIEW program used to conduct the tests. The five samples were then also averaged to yield temperatures that corresponded to the IR points produced in the same collection. The four surface temperatures could then be related to IR intensities at their corresponding positions in the IR images, via the relationship discussed in Chapter 2 and shown in Equation 30, to produce a calibration curve like shown in Figure 51. Several surface temperature measurements were collected to create a curve with half of the temperatures taken in ascending order while the other half taken while the plate cooled to detect hysteresis. The RMS for the sample data was 1.16 K but accounting for the number of data points in the calibration curve resulted in an uncertainty of 2.34 K in the IR surface temperature measurements with a 95% confidence interval. A similar calibration was performed for each day of testing to ensure that changes around the lab would be captured in the calibration and be less likely to dramatically impact the data.

$$T = a\mathcal{J}_{rad}^{1/4} + b \tag{30}$$

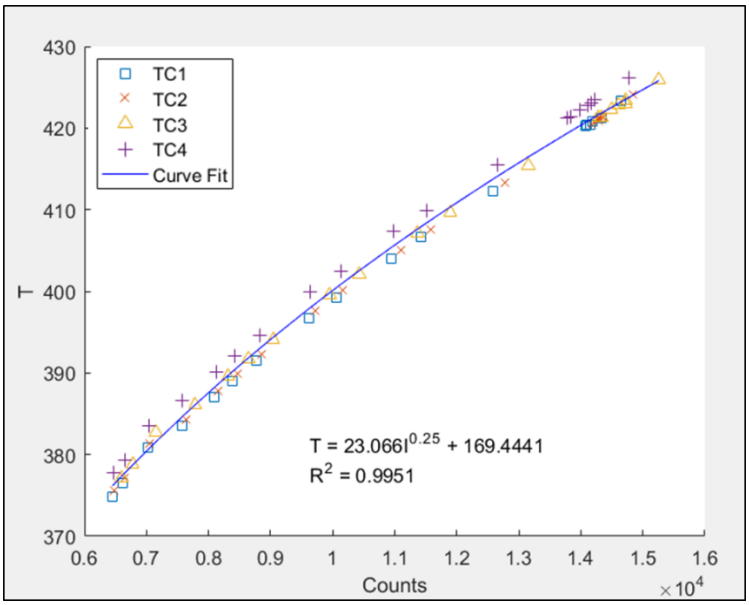

Figure 51. Original in-situ calibration curve example.

After several days of testing, it was noticed that the data for the fourth surface thermocouple, which was located closest to the stagnation row and near the edge of the viewing window, was consistently offset from the other data. Figure 51 shows an example of this observed offset. Though no actual cause was confirmed, it was the thermocouple's position in the viewing window that may have impacted the intensities collected in this region. Unfortunately, it was difficult to simultaneously view the leading edge while also keeping the fourth surface thermocouple sufficiently far away from the window's edge. As such, the data from the fourth thermocouple was dropped from the calibration. Figure 52 shows the resulting calibration from the same data used in the prior example. With this change, the uncertainty from the calibration was reduced to 1.06 K at 95% confidence.

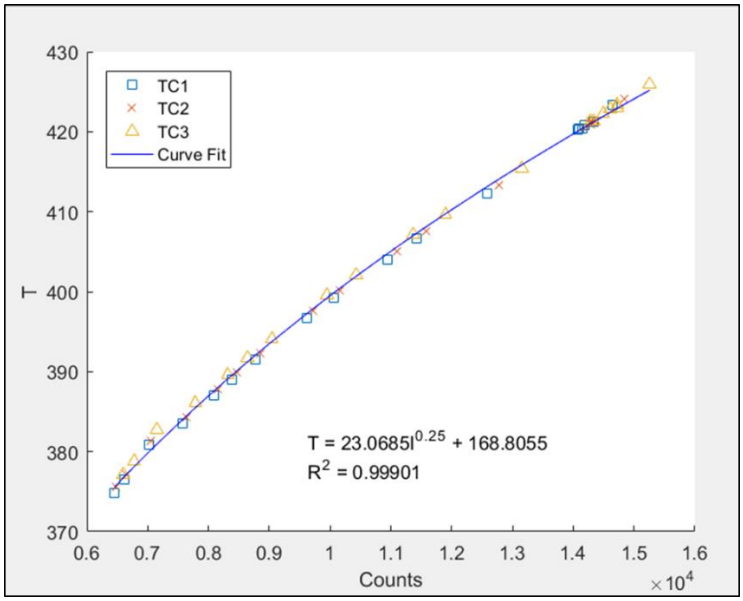

Figure 52. In-situ calibration curve without TC4.

While performing calibrations, it also became apparent that the camera shook during the tests. Prior to this investigation, past researchers used an automated calibration script that only required thermocouple pixel locations to perform the IR intensity averaging around the thermocouple. During this investigation, the script was modified to enable users to view the actual location of the averaging like shown in Figure 53. With this ability, the script could be modified to choose different pixel locations for each IR frame to use for the intensity averaging. Using this technique further increased the accuracy of the calibration curve as shown in Figure 54. For the same example data, the uncertainty in the curve was reduced to 0.89 K. While this magnitude of change was not observed for each calibration, the resulting calibrations were fairly consistent and relatively low. Table 4 summarizes the uncertainty calculated for each calibration curve used in this investigation.

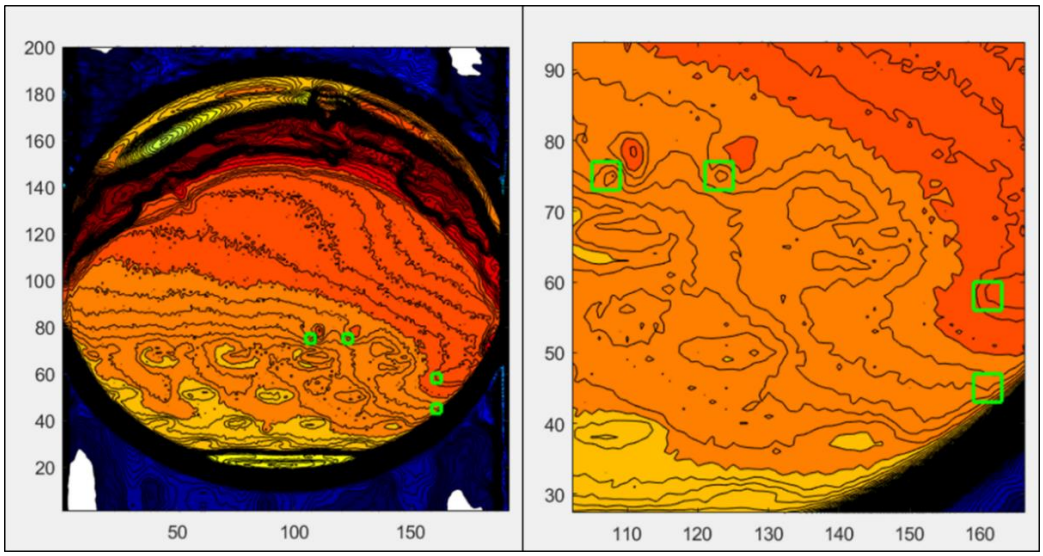

Figure 53. Calibration aid.

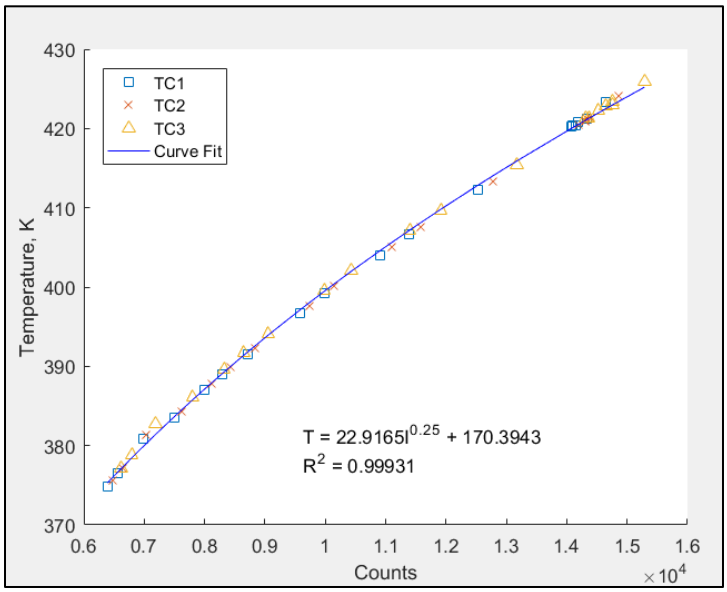

Figure 54. Pixel adjusted calibration.

Table 4. IR Calibration Uncertainty

Date	**Re_∞**	**$T_{\infty,max}$**	**Uncertainty**
20171227	10000	400 K	0.7334 K
20171229	9300	450 K	0.8884 K
20180105	10000	450 K	0.9435 K
20180115	15000	400 K	1.0932 K
20180118	15000	450 K	1.0986 K
20180124	10000	400 K	0.6300 K
20180126	10000	450 K	0.8464 K
20180128	15000	400 K	1.4058 K
20180129	15000	450 K	1.0992 K

While previous work with the FCR did include the use of leading edge models, the main region of focus for thermal measurements and performance quantification was on the flat portion of the test airfoil. An objective for this research was to quantify overall effectiveness on the leading edge where the test surface curved. Therefore, a new spatial calibration technique was required to orient the data taken by the IR camera. The final technique used was inspired by the spatial calibrations performed by Bryant [11] and Wiese [44]. For her spatial calibration, she used a tape with pins in it to mark locations when attached to her model. Since the model used for this investigation was much smaller, another method for marking locations was needed. The solution was to instead use a metallic pen to create a grid. This calibration grid was made by carefully tracing the lines of an existing 1/16" grid. A sample of the grid used is shown in Figure 55.

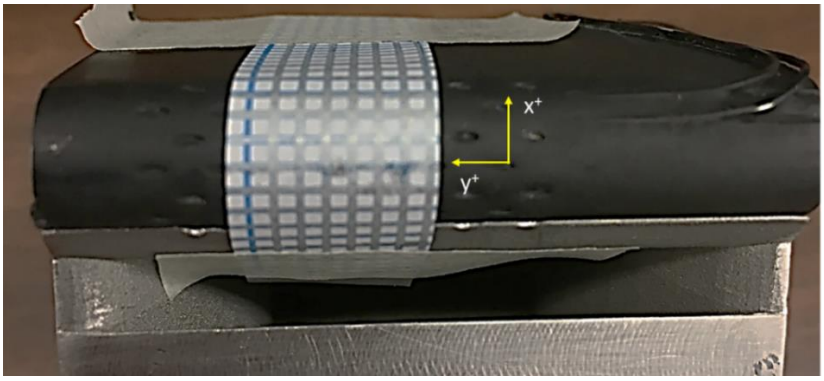

Figure 55. Fine spatial calibration grid.

Using this grid, a fourth-order polynomial was used to curve fit the spatial data in the x-direction. Figure 56 shows two curve fits created in this manner. The difference in the curves is that one was generated with the zero point defined while the other was created without a zero point. For this discussion, the zero point refers to the location of the stagnation row. Excluding zero produced a calibration curve with a higher R^2 but including the zero

produced a calibration curve that more closely predicted the location of the stagnation row. Ultimately, both of the spatial calibrations performed in this investigation used the method of including the zero point because it appeared to better position the coolant holes at the correct normalized position as shown in Figure 57.

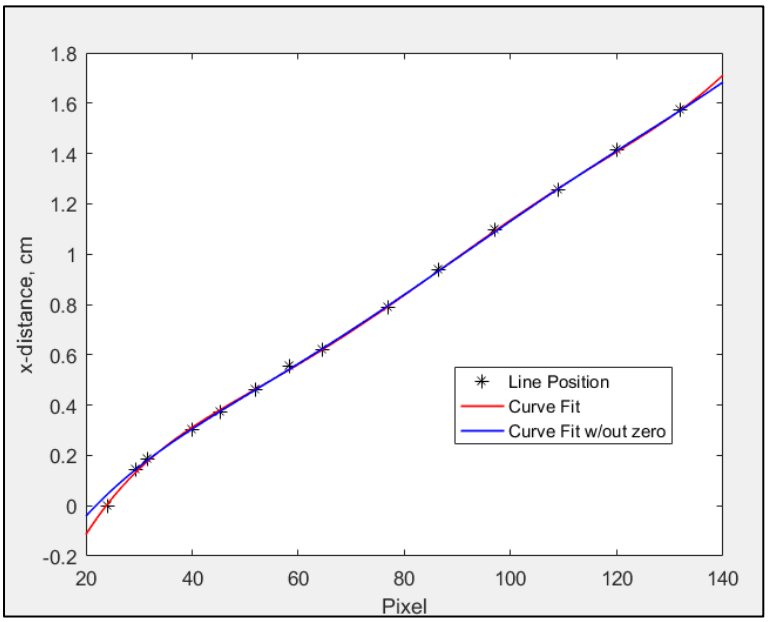

Figure 56. Spatial calibration curve comparison.

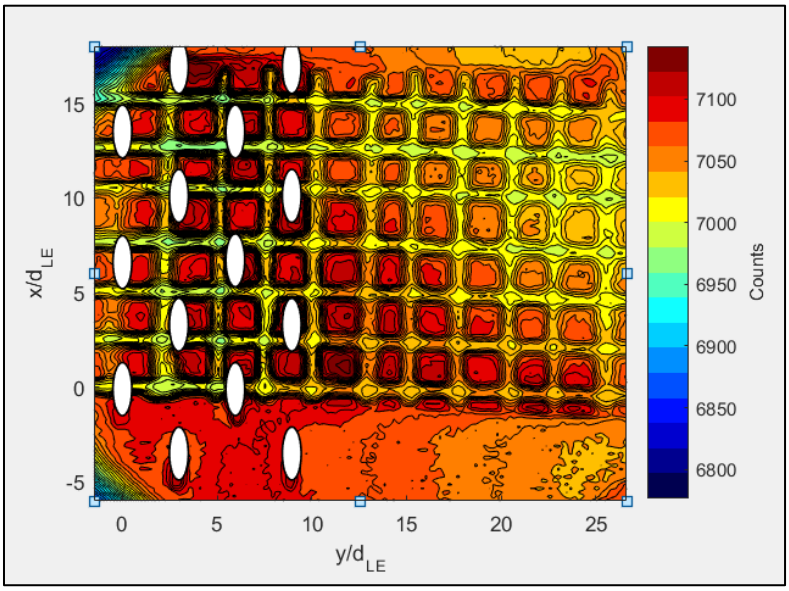

Figure 57. Spatially calibrated image.

A final concern about imaging the leading edge of the model was whether the surface curvature significantly impacted the radiant intensity received by the IR camera. As Bergman et al. [13] point out, the radiant intensity from real surfaces have directional dependence like shown in Figure 58. The concern was that as the leading edge surface curves away from normal to the IR camera the radiant intensity, because of directional dependence, may read artificially low. For this experiment, this would have the effect of measuring lower temperatures where the surface curved away from the camera which would create regions of artificially high overall effectiveness if the data was processed further.

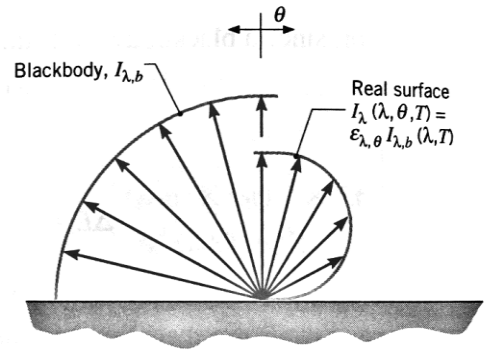

Figure 58. Examples of directional distributions [13]**.**

To ensure that the measurements for this experiment were not significantly impacted by this effect, a simple experiment was conducted to investigate how the surface radiated when the surface temperature was uniform. To generate a uniform surface temperature, the model was first heated by the hot freestream flow for a sufficient amount of time to allow the rig to become thermally soaked. The freestream and coolant flows were then shut off allowing conduction to redistribute heat through the model. With an approximately uniform test surface temperature of about 345 K, Figure 59 shows the IR count distribution. The uniform temperature case showed great uniformity which was backed up by the thermocouples which all read within 1 K of each other. In contrast, the intensity distribution

observed in the frame with film cooling, also shown in Figure 59, is more diverse. Therefore, there does not seem to be any evidence that intensities recorded near the stagnation were affected by a non-perpendicular viewing angle.

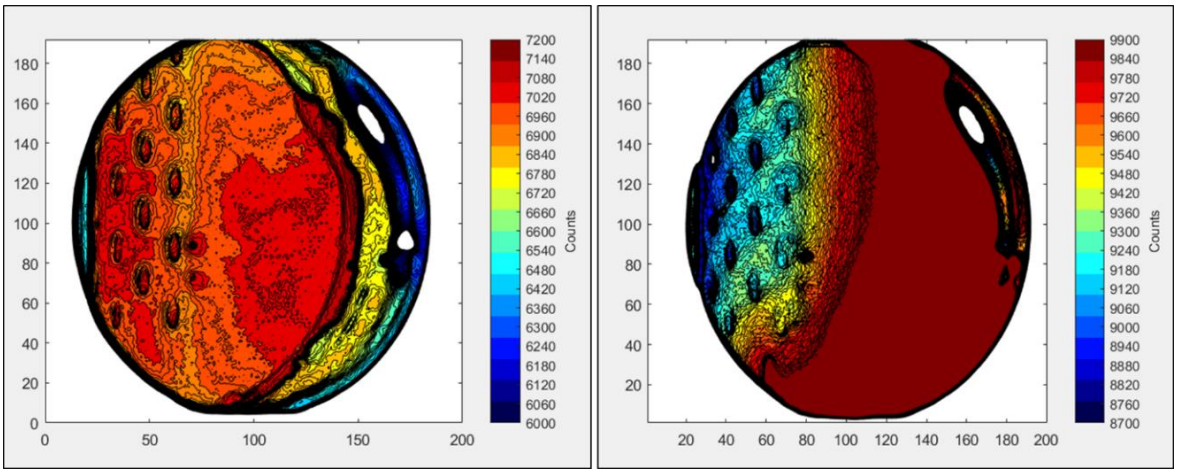

Figure 59. (Left) Leading edge at near uniform temp and (right) leading edge at test conditions.

To be certain, data starting from around the stagnation row to a location just past the last row of holes were pulled from the uniform temperature image, as shown by the blue line in the left graphic of Figure 60. Finding the maximum and minimum intensity count, the maximum difference in counts along the line was 107 counts. Translating these counts using the calibration curve produced on the same day found that the maximum temperature along the line was 344.6 K while the minimum temperature was 343.9 K. This represented a small difference in perceived surface temperature and further indicated that the measurements were not being significantly impacted by the surface curvature. An additional analysis was performed at a higher temperature case of 398 K. Figure 61 reveals that the maximum difference in count data was 195. This translated to a temperature difference of 1.16 K. The key being that the intensities do not drop near the stagnation row where the viewing angle was the steepest.

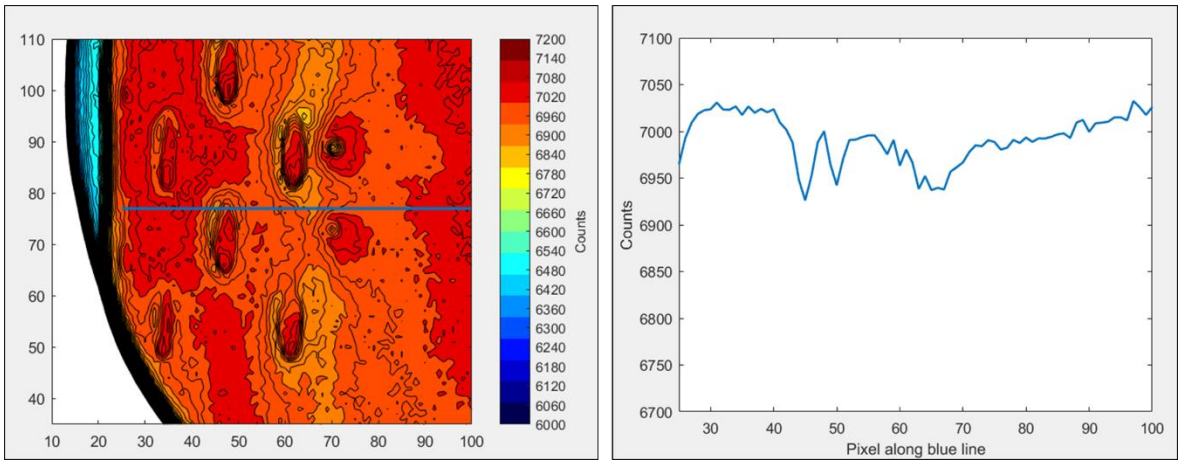

Figure 60. Low temperature intensity data.

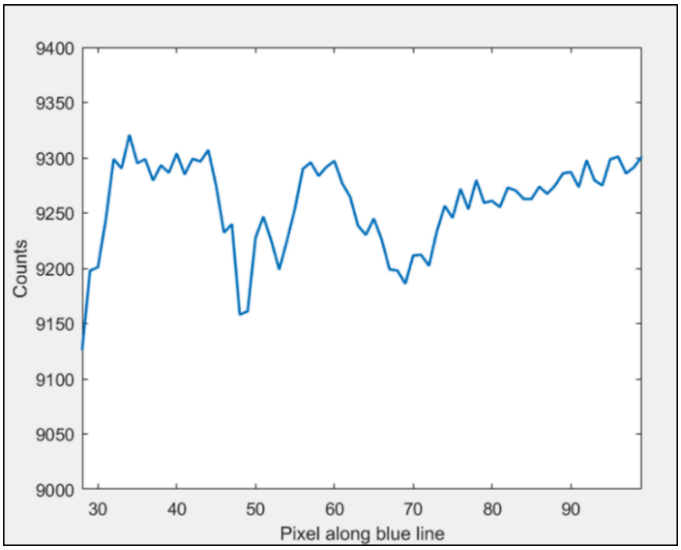

Figure 61. High temperature intensity data.

While both of these cases showed a relatively small variance for the data sampled, there was some decrease for the first couple of pixels. This could be a result of the steep viewing angle. Another possibility is that the data was influenced by the wall directly behind the model. Finally, the data may indicate that the data line was drawn through a hole. For the high temperature case, several drops in intensity data were observed that correlated with the position of the coolant hole row locations. While there was not a significant gradient in IR irradiation with viewing angle, it was acknowledged that obtaining accurate intensities right

at the leading edge was difficult and the first couple of pixel intensities were often ignored in the IR data processing.

Finally, on a few occasions it was suspected that the external temperature of the rig may have impacted some limited thermal measurements. Figure 62 shows data from a test that attempted to vary the density ratio during the test. For this test, the density ratio was varied by changing the coolant temperature while keeping the freestream temperature the same. The figure shows that as the density ratio increased the temperature and IR counts at the thermocouple decreased. The data shows that the decrease in the IR counts did not follow the previous trend exhibited by the rig earlier in the test where the freestream, and presumably the outside wall of the rig, was lower. It was believed that the calibration would account for this possible environmental effect; however, the trend here does not support this assertion. This issue along with a coolant heating issue forced an investigation of the density ratio effects to be delayed for a future investigation.

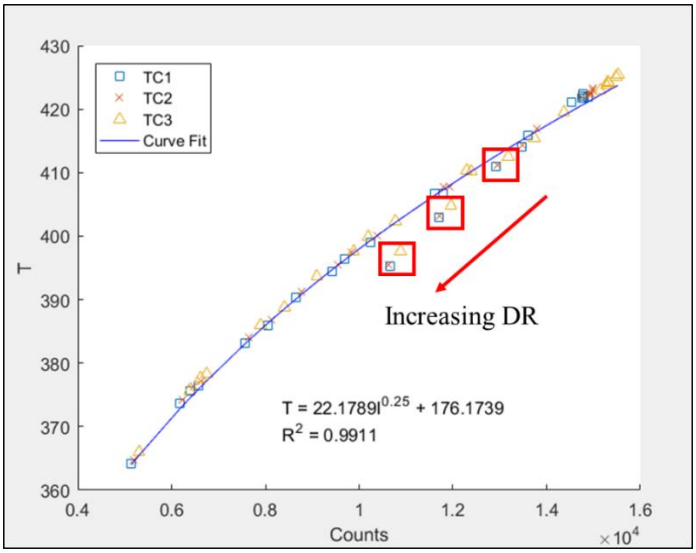

Figure 62. Changing DR issue.

3.3.3. Heat Flux Gauge

In any film cooling experiment, accurately determining the local heat flux on a model becomes extremely difficult because of the interaction of the freestream and coolant flows. Attempts have been made to acquire this value on models through various methods ranging in difficulty from extremely complicated and cumbersome to overly simplistic (and inaccurate). Double sided-heat flux gauges have been shown to be extremely responsive and fairly uncomplicated to employ. A drawback to this approach is that the sensors are limited to relatively low temperatures and can only make measurements at discreet locations where they are placed.

During this investigation, efforts were made to implement the double-sided heat flux gauges previously employed by the AFRL [4] to determine localized heat flux on the leading edge model. Once measured, these values could then be used to determine the localized convective heat transfer coefficient and the localized Biot number. Unfortunately, the heat flux gauges were not integrated into the experimental setup. However, this effort began to accrue the equipment necessary these heat flux gauges in the future. Of note, the COAL lab is now in possession of a several double-sided heat flux gauges, shown in Figure 63. Additionally, a new NI 9235 Compact Data Acquisition (CDAQ) module was purchased and installed in the COAL lab's data acquisition cabinet. The NI 9235 is one of National Instrument's C Series Strain/Bridge Input Module. It is meant to be used with a 120 Ω quarter-bridge sensor which will work with the existing heat flux gauges.

Figure 63. Doubled-sided heat flux gauges.

3.4. Experimental Uncertainty

This experimental uncertainty analysis examines the uncertainty obtained for two cases chosen because they were believed to have a combination of the best and worst IR calibration uncertainties. Table 5 summarizes the measurements important to this analysis as well as the factory reported measurement uncertainties and the calibration uncertainties used for this analysis.

Table 5. Uncertainty Analysis Representative Values

Measurement	**Low T/ Low M/ Low Re**	**Low T/ High M/ High Re**	**Uncertainty**
$\dot{m}_\infty$ **(kg/min)**	1.486	2.18	± 1%
$\dot{m}_c$ **(kg/min)**	0.016	0.053	± 1%
T_∞ **(K)**	400	400.1	± 0.75%
T_c **(K)**	366.1	363.6	± 0.75%
T_s **(K)**	374	372.7	0.73K/1.41K

Using these values, the uncertainty was assessed for *M*, *DR*, and ϕ using the constant odds, root-sum-square method described by Moffat [45].

$$\delta Z = \left[\sum_{i=1}^{N}\left(\frac{\partial Z}{\partial X_i}\delta X_i\right)^2\right]^{\frac{1}{2}} \tag{40}$$

where Z is the parameter of interest, X is a variable of the parameter Z, and δ represents the uncertainty of the variable or parameter of interest. The uncertainty for M and DR were assessed using their alternative forms shown in Equations 34 and 35. The results for each case are summarized in Table 6.

Table 6. Uncertainty Anaysis Results

	Case 1		Case 2	
Parameter	**Value**	**Uncertainty**	**Value**	**Uncertainty**
M	0.88	0.013	1.98	0.028
DR	1.09	0.012	1.1	0.012
ϕ	0.766	0.069	0.750	0.071

In both cases, the coolant temperature is the parameter driving the uncertainty in overall effectiveness. The product of the sensitivity coefficient and the instrument uncertainty for the coolant temperature was 0.062 for Case 1 and 0.056 for Case 2 accounting for most of the calculated uncertainty in overall effectiveness. Therefore, the uncertainty in overall effectiveness could best be improved by reducing the measurement uncertainty of the coolant.

3.5. Repeatability

To establish the reliability of the experimental results, the exact same target case was tested twice every day that data was collected. This case used T_∞ = 400 K, Re = 10,000, DR = 1.1, and M = 0.9. The test point was collected twice each day of testing for nine days total. The internal configuration changed on the sixth day with the addition of the impingement plate and remained in this configuration for the rest of the tests. Therefore, the repeatability was assessed for both internal configurations. Table 7 summarizes the mean, the standard deviation, and the 95% confidence interval for each set of measurements and results. The

overall effectiveness data for this analysis was sampled from the third streamwise line shown in Figure 72 (discussed further in Section 4.2) and averaged.

The analysis showed that both sets of data displayed fairly good repeatability for most of the measures. In the first set of the results, the standard deviation for the coolant temperature was much larger than the standard deviation for the freestream temperature indicating that there may have been some issues with setting the coolant temperature. The second set of data shows that the standard deviation for the coolant temperature improved and is likely attributable to increased operator experience for the second half of testing. The first data set showed better repeatability in overall effectiveness; however, both results fell within the calculated uncertainty.

Table 7. Repeatability Analysis Results

	$\mathbf{Re}_\infty$	$\dot{\mathbf{m}}_\infty$, kg/min	DR	M	$\mathbf{T}_\infty$, K	$\mathbf{T}_c$, K	$\bar{\phi}$
Mean 1	10182	1.478	1.092	0.884	400.12	366.55	0.775
Stdev 1	121	0.017	0.003	0.010	0.19	0.99	0.011
95% CI	279	0.04	0.007	0.024	0.44	2.29	0.025
Mean 2	10180	1.477	1.089	0.884	400.03	367.42	0.794
Stdev 2	130	0.019	0.001	0.011	0.04	0.30	0.015
95% CI	308	0.045	0.002	0.027	0.10	0.71	0.036

4. Analysis and Results

As outlined in Chapter 1, the objectives of this investigation included redesigning of the FCR to better match AFIT's large scale rig, continue the work of investigating the impact of different nondimensional parameters on the scaling of film cooling effectiveness, and examining the thermal scaling behavior of Inconel 718. Section 4.1 discusses the results of matching the engine scale rig to the large scale rig. This section includes a discussion of the difficulty of creating matched conditions despite the changes made to the rig as well as an investigation conducted on the ability to set the stagnation point with the new components discussed in Chapter 3. Section 4.2 discusses the data collected supporting the scaling investigations. For this investigation, tests were conducted for a single density ratio over two temperature regimes, at two different Reynolds numbers, and at four different blowing ratios. Additionally, the impact of using different internal cooling schemes was studied. Section 4.3 discusses the Inconel 718 thermal scaling investigation. Using the best and worst cases of the scaled tests from Section 4.2, this section examines how the scaling of the thermal conductivity ratio impacts the scaling of the overall effectiveness according to the analytical method devised by Stewart and Dyson [3].

4.1. Geometric scaling

With all the changes to the FCR, the first major task after re-assembling was to determine the operational capability of the rig. The following will discuss how the inlet Reynolds number was set and why the small scale rig could not achieve the same testing conditions used in the large scale rig. Additionally, the discussion will also consider the limitations of setting the density ratio and the blowing ratio.

To begin this analysis, the target freestream Reynolds number and temperature must first be established as discussed in Section 3.3.1. For this analysis, the target Reynolds number from the large scale rig was 60,000 [11] and the target freestream temperature was 600 K. Using these conditions, the freestream mass flux was determined via Equation 35. The experiment would need a freestream flow of about 11.5 kg/min, which translates to 320 m/s through the test section. As discussed in Section 3.3.1, however, the rig could only sustain a mass flow rate of only 3.7 kg/min. Additionally, it is unlikely that 600 K could be reached with current setup at this mass flow rate. Repeating the exercise with an assumed freestream temperature of 450 K decreases the mass flow requirement to 9.46 kg/min which still exceeds the rig's mass flow capability. Reducing the target Reynolds number to 20,000 for a freestream temperature of 450 K brings the mass flow requirement down to 3.15 kg/min, which falls within the capability of the rig.

In addition to the freestream flow considerations, the coolant flow requirements must also be considered. For the case of Re = 20,000 and T_∞ = 450 K, a blowing ratio of 2 requires 60 SLPM of coolant. As discussed in Section 3.3.1, the limit for the current rig setup is 50 SLPM. An additional issue to consider is whether the density ratio is achievable. An original goal was to perform tests at multiple *DR*s; however, it was discovered during the course of testing that the coolant temperature was still coupled to mass flow rate, as was observed in Vorgert's experiments [34]. This made it difficult at low coolant mass flow rates to create large temperatures differences between the coolant and the freestream temperature because the coolant temperature would rise significantly as it traveled through the coolant block.

Figure 64 contains two plots showing how the coolant warmed while traveling through the coolant delivery system during some of the tests conducted in this investigation.

The data shown was derived from Condition 1 (low *Re*, low T_∞) testing with and without the impingement plate installed, as discussed later in Section 4.2. The coolant gas temperature was measured in multiple locations as reviewed in Section 3.3.2. The first temperature recorded occurred at the exit of the coolant heaters, $T_{h,exit,}$ which was positioned about 178 mm from the entry of the coolant delivery block and was about 260 mm from the next thermocouple, which measured the temperature inside of the coolant delivery block, T_{IC}, and was positioned just before the coolant delivery block exit as shown in Figure 49. The next two thermocouples were located in the coolant plenum located inside of the leading edge, also shown in Figure 49, and were separated from the coolant block thermocouple by about 2.5 mm. These thermocouples provided temperature measurements of the coolant, $T_{c,1}$ and $T_{c,2}$, just prior to exiting the coolant holes in the leading edge. During tests with the impingement plate installed, the two thermocouples in the coolant plenum were positioned on either side of the impingement plate where $T_{c,1}$ measured the coolant temperature before the impingement plate and $T_{c,2}$ measured the coolant temperature after the impingement plate.

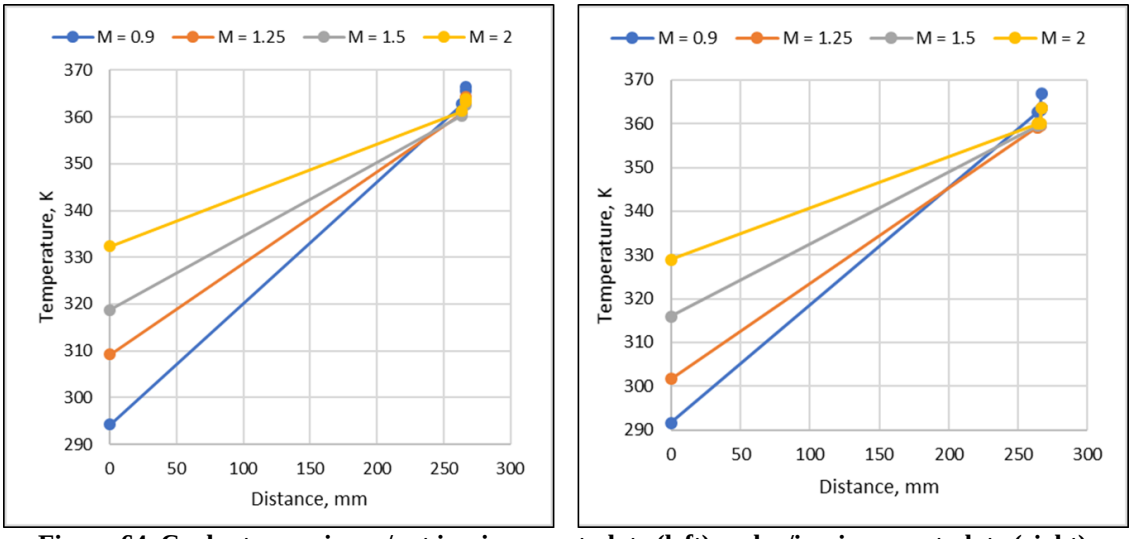

Figure 64. Coolant warming w/out impingement plate (left) and w/impingement plate (right).

Both plots in Figure 64 show that the coolant warmed the most as it traversed through the coolant delivery block (i.e. between the measurement locations of $T_{h,exit}$ and T_{IC}). For the lowest blowing ratio case, the coolant warmed by 68.5 K and 72.3 K between the first and second thermocouples for the cases without and with the impingement plate installed, respectively. For the highest blowing ratio case, the coolant warmed by 31.5 K and 32.8 K, again, for the cases without and with the impingement plate installed. For the blowing ratios above M = 0.9, the coolant had to be heated before entering the block to ensure the correct density ratio based on the temperature of the coolant inside of the coolant plenum. Both plots show that a majority of the tests ended at the correct temperature (T_c = 363.6 K) based on the density ratio, however, the M = 0.9 cases resulted in slightly elevated coolant temperatures which meant that the density ratio was also slightly off. This trend did not occur in all tests but did affect a few low coolant mass flow test points.

Figure 64 also shows that the coolant temperature in the coolant plenum warmed differently for the different internal cooling configurations (i.e. with and without the impingement plate installed). For the tests without the impingement plate installed, the two thermocouples in the coolant plenum measured similar gas temperatures. For the data plotted, the maximum difference between $T_{c,1}$ and $T_{c,2}$ was 0.9 K without the impingement plate installed. With the impingement plate installed, the maximum difference between $T_{c,1}$ and $T_{c,2}$ was 3.9 K.

Figure 65 shows how much the temperature rose as a function of the coolant mass flow rate. The data shown comes from Condition 1 (low *Re*, low T_∞) and Condition 4 (low *Re*, low T_∞) testing for both internal cooling configurations. This figure confirms the trend noted earlier that the coolant warms less at higher mass flow rates. Additionally, the figure

confirms that the tests with the impingement plate installed showed slightly higher warming compared to the cases without the impingement plate. This warming prevented the use of lower blowing ratios which would have caused the density ratio to severely deviate from the target density ratio.

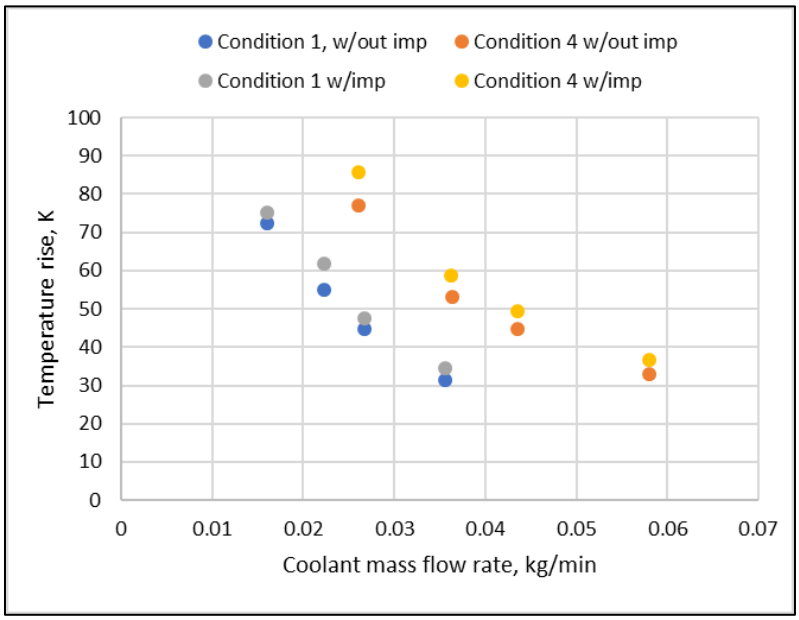

Figure 65. Coolant warming from heater exit to coolant plenum as a function of the mass flow rate.

Creating like conditions did not fall solely on the small scale rig, however. Since the FCR was unable to match the Reynolds number used in Bryant's experiments [11], the question was whether the large scale rig could perform tests a lower Reynolds numbers that the small scale rig could achieve. Through some coordination with Bryant, it was discovered that the large scale rig could conduct reduced Reynolds number tests. Therefore, Bryant conducted additional testing using the same nondimensional parameters summarized in Table 8 in Section 4.2. The testing with the large scale rig used the same methodology described in Ref. 11. Figure 66 shows an example of results produced by both rigs at Reynolds numbers of 10,000, density ratios of 1.1, and blowing ratios of 1.25 without the impingement plate installed. Both plots show contours of overall effectiveness with the

freestream flowing from left to right. The coolant injection directions are flipped but this does influence the results. The results are presented with axes that are nondimensionalized by the leading edge diameter rather than the coolant hole diameter because of the manufacturing issues with the small scale rig. Additionally, the regions examined are slightly different due to the different IR thermography setups for each rig. The regions enclosed by the dashed boxes in Figure 66 represent the overlapping portion of the leading edge models observed.

Comparing the overall effectiveness results within the dashed boxes, the small scale results showed higher effectiveness throughout the entire surface compared to the large scale results. Another trend observed was that the overall effectiveness was highest near the first row of holes for the small scale results while the overall effectiveness for the large scale results in the same region was lowest. It was initially believed that the low effectiveness near the first row of holes for the large scale results was indicative of the freestream impinging on this row and meant that the small scale rig did not have the stagnation point set correctly. However, previous work conducted by Dyson et al. [46] and Ravelli et al. [26] on a similar experimental setup showed similar overall effectiveness trends to the small scale results. In their testing, they employed internal impingement cooling to produce these trends. Although the coolant delivery method employed by the small scale rig was meant to emulate the method used by the large scale rig, the results suggest that the coolant delivery block exit of the small scale rig more closely emulated the impingement plates used by Dyson et al. and Ravelli et al. rather than Bryant's [11] coolant delivery loop. Finally, the large scale model was intended to nominally match the *Bi* of an engine component at engine conditions using the experimental conditions outlined in Bryant's work. However, both tests were conducted

at significantly reduced freestream conditions which is believed to contribute to a mismatch of their *Bi*'s which means that the relative importance of conduction and convection was different between the two setups. The thermal conductivity for the large scale Corian model was reported to be around 1.009 W/m-K while the thermal conductivity for the small scale Inconel 718 model varied between 12.5 and 13.2 W/m-K during this investigation.

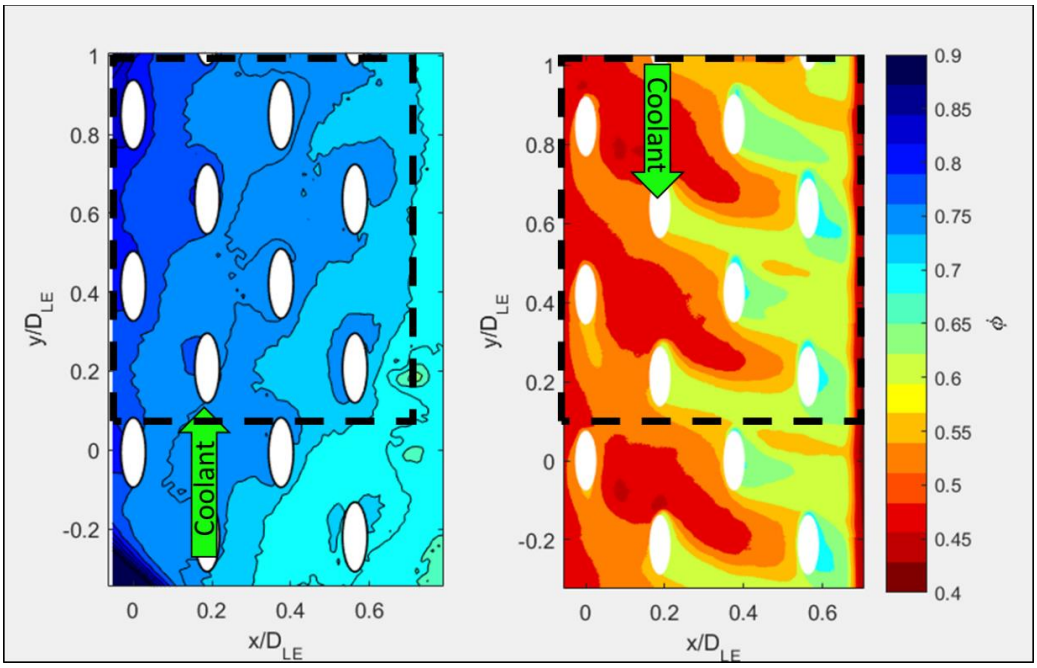

Figure 66. Small (Left) and Large (Right) scale results for Re_∞=10k, *DR*=1.1, *M*=1.25 without impingement.

While the slight geometry mismatches were expected to have an impact on the overall effectiveness distributions, it appears that there was something else fundamentally different between the two test setups that has caused opposite trends in the overall effectiveness. A possible contributor is believed to be the different coolant delivery methods employed by each rig. The coolant delivery block exit for the small rig does not exactly emulate the coolant delivery loop employed by the large scale rig. Rather than distribute coolant in a circular pattern around the diameter of a coolant loop, the small scale coolant delivery block ejects in only one direction, directly toward the leading edge and acts more line an impingement

plate. Further, the results were likely collected on models with mismatched *Bi* because the large scale model was designed to match results of engine components tested in higher *Re* and higher temperature conditions. Finally, the whereabouts of the stagnation line on the small scale model during testing was unknown. The following section discusses an effort to establish the location of the stagnation location.

4.1.1. Determining Effect of Bypass Channel on Stagnation Location

As previously discussed in Chapter 3, there were significant changes to the main flow path. As such, it was desired to begin characterizing how the main flow interacted with the test airfoil and determine how much control the experimental setup enabled over the freestream flow. Specifically, it was important to determine where the stagnation point occurred on the test airfoil and how much control the new bypass channel adjustor allowed. In an initial attempt to visualize the flow in the test section, smoke was funneled to the rig from a smoke generator. However, because the smoke generator relied on buoyancy differences to drive the flow of smoke and was not pressure driven, even modest freestream flow rates driven by a high pressure source upstream caused the smoke to backtrack and blow out of the venting in the generator. Therefore, another technique was sought to perform this analysis.

While reviewing Bryant's experiment [11], it was noticed that the coolant plumes were visible in the results and the direction of the coolant flow was apparent. Additionally, she showed that the coolant hole rows ingested at low overall blowing ratios. The stagnation row's critical blowing ratio, or the blowing ratio at which the row of holes stopped blowing, was $M = 0.64$ while the next row's critical blowing ratio was $M = 0.32$. With this knowledge,

a second attempt was made to identify the location of the stagnation point by using IR thermography to visualize the coolant flow exiting the holes at a low blowing ratio. An experiment was conducted at conditions close to T_∞=400K, *Re* =10,000, *DR*=1.1, and *M*=0.5 with the impingement plate installed. Several measurements were taken at blockage gate positions of full open, ¼ closed, ½ closed, ¾ closed, and fully closed. Both IR images and thermocouple measurements were taken during this experiment. Using this data coupled with a calibration curve, the data was turned into effectiveness plots. Using Rutledge's $\Delta\phi$ method [10] which was discussed in Section 2.2.3, the effectiveness distributions were compared to determine if the coolant plume changed positions when changing the gate position. The results for the full open case, shown in Figure 67, served as the baseline against which all the other results were compared.

Examining the results in Figure 67, the fourth row of coolant holes appeared to issue coolant up and to the right as expected. The third row also showed signs of coolant flowing up and to the right. The second row appeared to have coolant flowing to the left. Finally, the first row also appeared to have coolant flowing left; however, the results around this row, especially to the left of the coolant holes, are suspect due to the steep viewing angle of the leading edge. The measured freestream and coolant temperatures during this test were 397.3 K and 367.9 K, respectively.

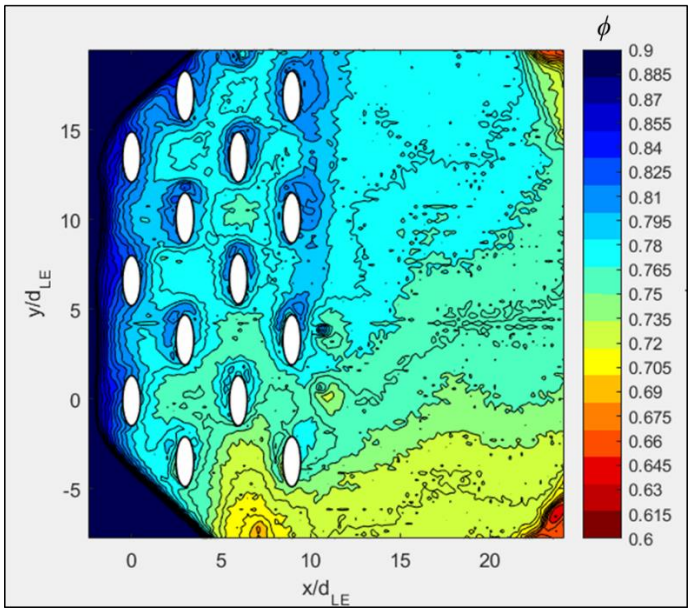

Figure 67. Results from fully open channel case (*Re* = 10k, *M* = 0.5, $T_\infty \approx 400$ K).

Figure 68 shows the $\Delta\phi$ and ϕ distributions for the ¼ closed case. In the ¼ closed case, there appears to be a small amount of warming that occurred near the leading edge, indicated by the negative $\Delta\phi$ in the left plot. Again, it must be reiterated that at the actual leading edge there is some uncertainty with results due to the steep viewing angle. The rest of the chart is white indicating that the surface did not warm due to the closing of the gate. Examining the ϕ distribution, the results confirmed that the cooling pattern did not change significantly with the coolant flow appearing to flow in the same manner as described previously. The measured freestream temperature for this test was 397.1 K, which compared well with the baseline, while the coolant temperature increased by about 0.5 K to 368.4 K.

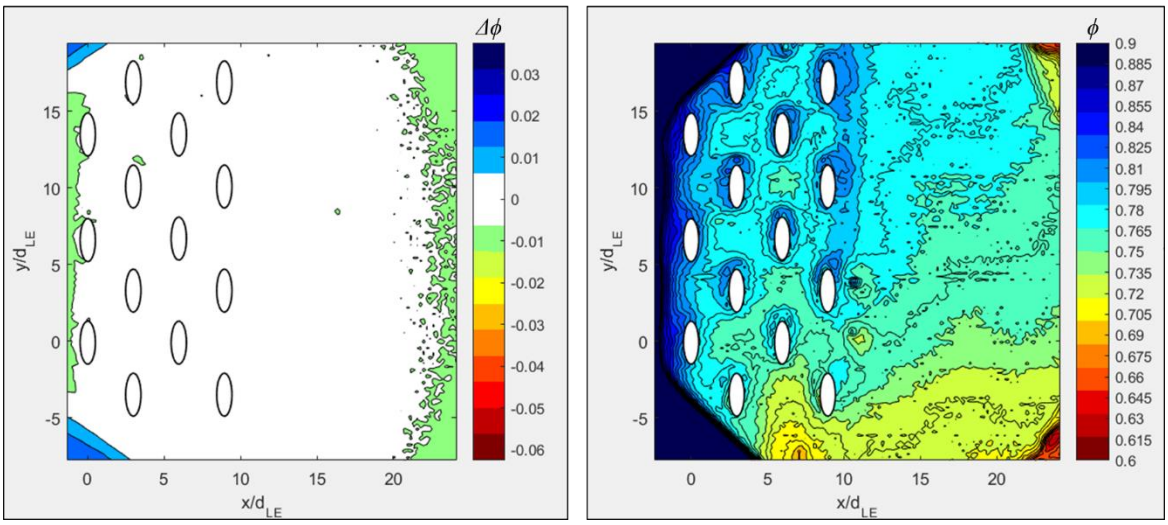

Figure 68. $\phi_{[1/4\ closed]}$ - $\phi_{[open]}$ (left) and $\phi_{[1/4\ closed]}$ (right).

Figure 69 shows the $\Delta\phi$ and ϕ distributions for the ½ closed case. $\Delta\phi$ shows that warming occurred throughout the entire test surface. Again, the leading edge appears to warm more than the rest of the model's surface. Despite the rest of the surface showing some change, the features that can be made out with the contours do not seem to yield any information about the stagnation location on the airfoil as there no distinct movement of the coolant plumes. The measured freestream temperature for this test cooled slightly by 0.5 K to 396.8 K while the coolant temperature warmed by 0.7 K to 368.6 K compared to the baseline, which increased the difference between the freestream and coolant temperature by 1.2 K. This may be the reason why the effectiveness dropped by 0.01 for tests at this gate position. Examining the ϕ distribution plot, the coolant from the fourth row still appeared to flow up and to the right but appeared to provide even less cooling, possibly an effect of the changed the freestream and coolant temperature. The third row showed signs of coolant flow up to the right and also to the left. Coolant from the second row appeared to be flowing mostly to the left but also appeared to have some coolant flowing up and to the right for at least one hole. Finally, the first row appeared to also have coolant flowing left still.

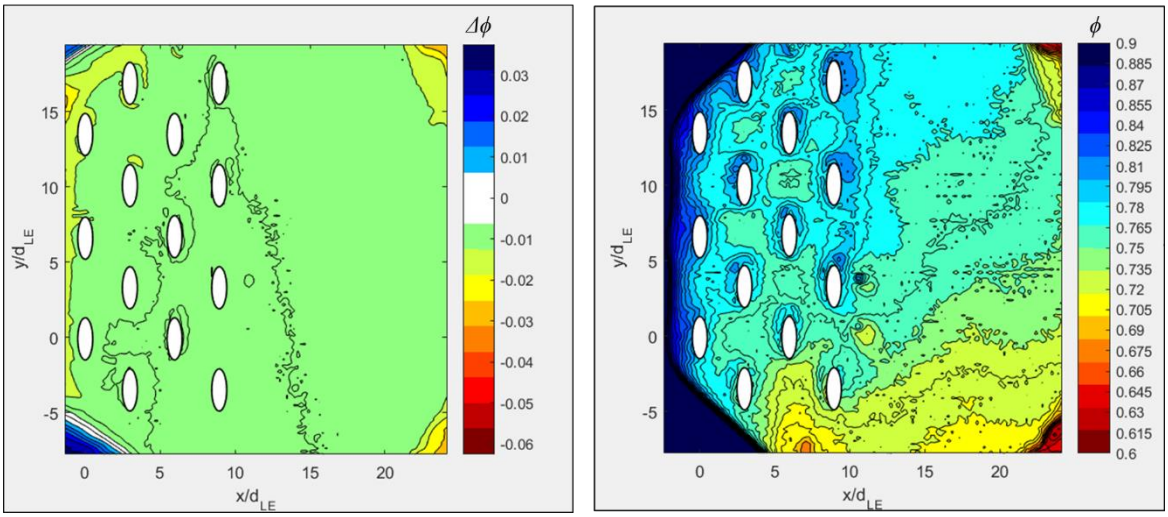

Figure 69. $\phi_{[1/2\ closed]}$ - $\phi_{[open]}$ (left) and $\phi_{[1/2\ closed]}$ (right).

Figure 70 shows the $\Delta\phi$ and ϕ distributions produced by the ¾ closed bypass. For the $\Delta\phi$, the surface had warmed further and showed more distinct features than the previous cases. Specifically, the leading edge had warmed further and a region appeared around the third and fourth row of holes of locally cooler surface temperatures. This region did not produce positive $\Delta\phi$ values but were cooler than the surrounding surfaces. Besides this development, the second row of holes showed significant warming possibly indicating that the freestream was impinging in that region. However, it is still difficult to tell if that is the case. Examining the measured gas temperatures, the freestream temperature for this test decreased from the baseline by 0.4 K to 396.9 K while the coolant temperature increased from the baseline by 0.4 to 368.3 K increasing the difference between the freestream and coolant temperature by 0.8 K compared to the base line, which was a smaller change than observed in the previous comparison. This indicates that if this change in the delta between the gas temperatures has an effect on the overall effectiveness, the effect would be slightly diminished for this case meaning that the observed increase in $\Delta\phi$ is due the changing of the

blockage. In the ϕ distribution plot, the cooling patterns appear very similar to the previous trends except that the third row showed signs of decreased coolant flow.

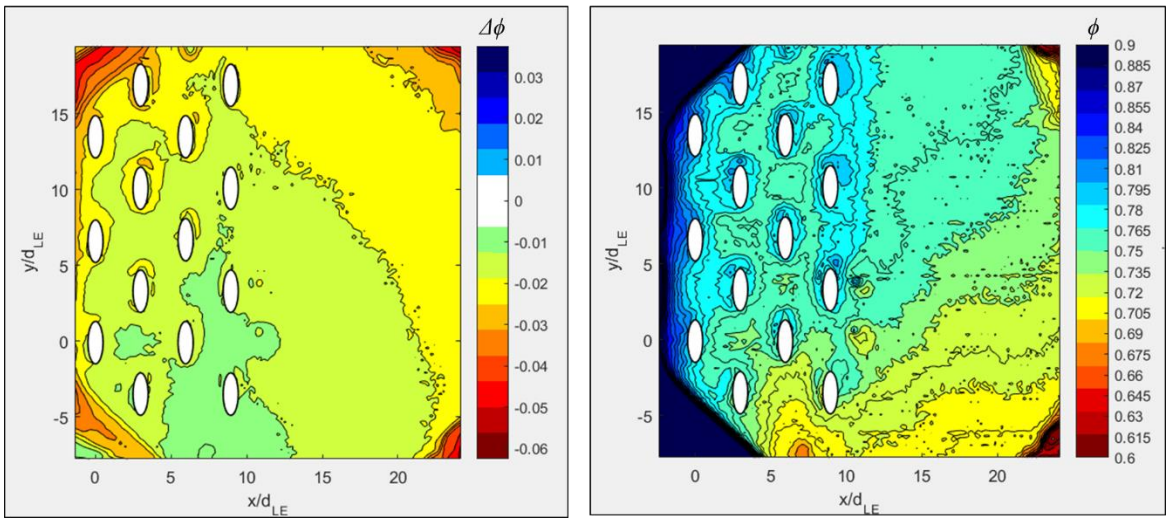

Figure 70. $\phi_{[3/4\ closed]}$ - $\phi_{[open]}$ (left) and $\phi_{[3/4\ closed]}$ (right).

Examining the fully closed bypass results in Figure 71, the model has heated throughout most of the frame. More features have appeared and the locally "cool" region near row three appears to have warmed compared to the ¾ closed case. More specifically, the third and fourth row of holes show significant warming while the first and second row of holes appear to have generated islands around the coolant holes compared to the previous frame. Like with the previous results, the warming of the third and fourth rows might indicate that the freestream is impinging in this region. If that were the case, however, it is expected that the stagnation region (the first row) would be cooled due to coolant from row two and maybe three now flowing in the -x/d direction. The absence of this occurring could be a result of picking a baseline that did not impinge on the stagnation row and had more coolant blowing out of the holes. If this is the case, then it is possible that the stagnation point moved as described but this region was not as cool as occurred for the fully open case. Examining the gas temperatures found that freestream warmed by 0.1 K to 397.2 K while the coolant

temperature cooled by about 1.4 K to 366.5 K increasing the difference in freestream and coolant temperatures by 1.5 K compared to the baseline case. Again, this may have contributed to the magnitude of the $\Delta\phi$'s observed; however, the patterns indicate that a shift of the freestream. Inspecting the ϕ distribution, the major development appears to reduced coolant from the third and fourth rows. The third row showed appeared to be on the verge ingestion.

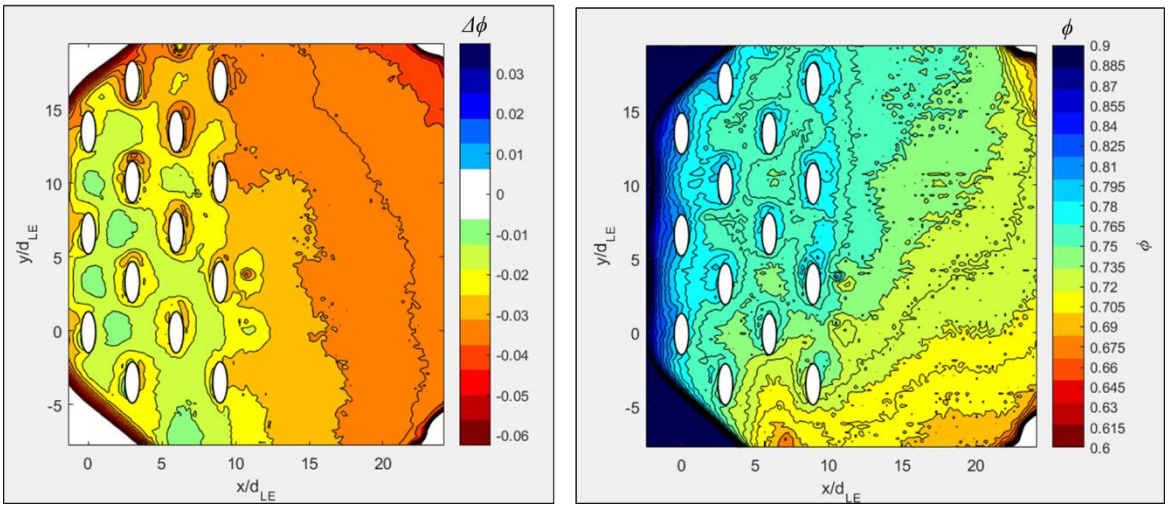

Figure 71. $\phi_{[\text{fully closed}]}$ - $\phi_{[\text{open}]}$ (left) and $\phi_{[\text{fully closed}]}$ - $\phi_{[\text{open}]}$ (right).

With the data collected, it was difficult to be certain of the exact effect of the bypass blockage adjustor, especially with the small changes in effectiveness that were measured. Complicating matters further, the surface temperature and the overall effectiveness are functions of the inside coolant temperatures which fluctuated throughout the tests; however, the exact reasons for the changing of the coolant temperature were unknown. The current belief is that the temperatures were affected by a combination of the shifting of the impingement location on the model and the shifting of the portion of the freestream passing through the bypass. Because uncertainty still surrounded the exact location of the stagnation point, the remaining tests were conducted using the full open channel to reduce the variability

of the freestream conditions between each test. Also, because it appeared that in the full open condition, the coolant was stagnating closer to the leading edge.

4.2. Impact of nondimensional parameters

For this work, the objective was to examine the impact of the various nondimensional parameters on overall effectiveness. A summary of the test matrix is shown in Table 8. With the FCR now a scaled version of Bryant's rig [11], it was desired to examine some of the same parameters. In Bryant's work, she showed that the model ingested at the lower blowing ratios. For this examination, cases of ingestion were undesirable so the decision was made to test the highest blowing ratio used (M = 0.9) in addition to examining three additional higher blowing ratios. The initial goal was to also use the same Reynolds number of 60,000; however, this proved to be too large of a Reynolds number for the FCR. Therefore, the goal was readjusted to conduct tests at two lower Reynolds numbers. As another goal was to conduct a scaling investigation between temperature regimes, tests were conducted at two different freestream temperatures. The original goal was to use freestream temperatures of 450 K and 600 K; however, issues with getting the new freestream heaters installed prohibited using 600 K as one of the freestream temperatures. Therefore, it was decided to use 400 K and 450 K as the two freestream temperatures.

Table 8. Summary of test matrix

Condition	DR	M	T_∞, K	T_c, K	Re	Internal Configurations
1	1.1	0.9, 1.25, 1.5, 2	400	363.6	10k	Empty/ Imp plate
2	1.1	0.9, 1.25, 1.5, 2	450	409.1	10k	Empty/ Imp plate
3	1.1	0.9, 1.25, 1.5, 2	400	363.6	15k	Empty/ Imp plate
4	1.1	0.9, 1.25, 1.5, 2	450	409.1	15k	Empty/ Imp plate

In total, nine days of testing were conducted in support of the scaling investigations.

Table 9 summarizes the conditions attained for each of the main test points that will be discussed throughout this section. Of the nine days of testing completed, eight days produced data that fit the purposes of this investigation. In general, the tests were conducted at two freestream Reynolds numbers: a low *Re* of 10,000 or a high *Re* of 15,000 and. There were also two freestream temperatures used in these tests: a low T_∞ of 400 K or a high T_∞ of 450 K. At these conditions, the coolant temperature and flow were adjusted to achieve a *DR* of 1.1 and *M's* of 0.9, 1.25, 1.5, and 2.0. Additionally, the internal cooling was changed for the second half of testing by installing the impingement plate into the leading edge as discussed in Section 3.2.2.

Table 9. Summary of data points collected

Date	Re	DR	M	T_∞, K	T_c, K	Impingement Plate?
27-Dec-17	10245	1.093	0.878	400.0	366.1	No
27-Dec-17	10361	1.100	1.206	400.2	363.8	No
27-Dec-17	10151	1.102	1.478	400.0	363.1	No
27-Dec-17	10190	1.100	1.962	400.0	363.5	No
05-Jan-18	9817	1.100	0.917	449.9	409.0	No
05-Jan-18	10064	1.100	1.242	450.0	408.9	No
05-Jan-18	9808	1.100	1.529	450.0	409.0	No
05-Jan-18	9946	1.100	2.011	449.9	408.9	No
15-Jan-18	14974	1.102	0.902	400.0	363.0	No
15-Jan-18	15037	1.101	1.263	400.0	363.3	No
15-Jan-18	14986	1.101	1.501	400.0	363.4	No
15-Jan-18	14919	1.100	2.011	400.0	363.5	No
18-Jan-18	15077	1.099	0.896	449.8	409.4	No
18-Jan-18	15053	1.100	1.248	450.0	409.1	No
18-Jan-18	15264	1.100	1.474	450.0	409.2	No
18-Jan-18	15156	1.100	1.980	450.0	409.1	No
24-Jan-18	10246	1.090	0.878	400.0	367.0	Yes
24-Jan-18	10297	1.100	1.214	399.9	363.6	Yes
24-Jan-18	10185	1.100	1.472	400.0	363.6	Yes
24-Jan-18	10328	1.100	1.936	400.0	363.6	Yes
26-Jan-18	10096	1.100	0.891	450.0	408.9	Yes
26-Jan-18	9951	1.100	1.256	450.0	409.0	Yes
26-Jan-18	9983	1.100	1.502	450.1	409.0	Yes
26-Jan-18	10027	1.100	1.995	450.0	409.1	Yes
28-Jan-18	14995	1.093	0.900	400.1	366.0	Yes
28-Jan-18	14803	1.100	1.267	399.9	363.6	Yes
28-Jan-18	14778	1.100	1.522	400.1	363.6	Yes
28-Jan-18	15028	1.100	1.996	400.1	363.6	Yes
29-Jan-18	15241	1.100	0.886	450.1	409.1	Yes
29-Jan-18	15071	1.100	1.244	449.9	409.1	Yes
29-Jan-18	15242	1.100	1.476	449.9	409.1	Yes
29-Jan-18	15022	1.100	1.998	449.9	409.1	Yes

Much of the previous work done in the FCR focused on examining the flat afterbody where no coolant holes were located. This made examining the data uncomplicated. However, this investigation focused on a hole dense region of the model which had the potential of skewing the data if processed in a manner that included data from the holes.

Furthermore, a goal was to also compare effectiveness data produced with this test to the large scale results. The regions examined were different, however, due to the achievable view of the FCR discussed in Chapter 3. The coolant hole mismatch also forced the normalized distances to be mismatched. With that in mind, it was decided to first investigate a couple of methods that could be used to examine and compare the data.

The following discusses the two methods considered for use to view and compare the data. First, each image was processed and aligned using the grid and coolant hole ellipses as shown in Figure 72. The vertical lines were drawn at *x/d* = 1.5, 4.5, 7.5, and 10.5 while the streamwise (horizontal) lines were drawn at *y/d* = 1.6, 8.4, and 15.2. The spanwise (vertical) lines were broken down into two sections each representing one nondimensionalized hole pitch of y/d = 6.8. The first section spanned from *y/d* values 1.6 to 8.4 while the second section spanned form *y/d* values 8.4 to 15.2. These lines were then used to grab data from the images to create 2-D plots.

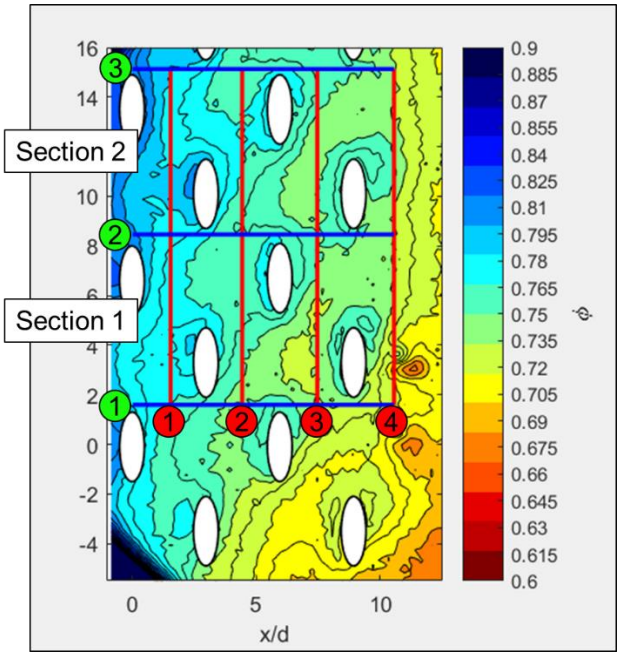

Figure 72. Data zoning example.

To better understand how effectiveness changes from Section 1 to Section 2, Figure 73 was produced by subtracting the spanwise averaged Section 1 data from the Section 2 data. The figure uses data from the test cases that experienced the smallest and largest $\Delta\phi$. The solid line represents the $\Delta\phi$ for Condition 3 (Re = 15,000, T_∞ = 400 K) without the impingement plate. The dashed line represents the $\Delta\phi$ for Condition 2 (Re = 10,000, T_∞ = 450 K) with the impingement plate installed. The figure indicates that effectiveness increases further into the showerhead cooling scheme for all cases as expected. Furthermore, this figure shows that the change in effectiveness between Section 1 and Section 2 data are all below 0.03, which means that the changes in effectiveness are fairly small and that the data demonstrates near pitch repeatability in this region.

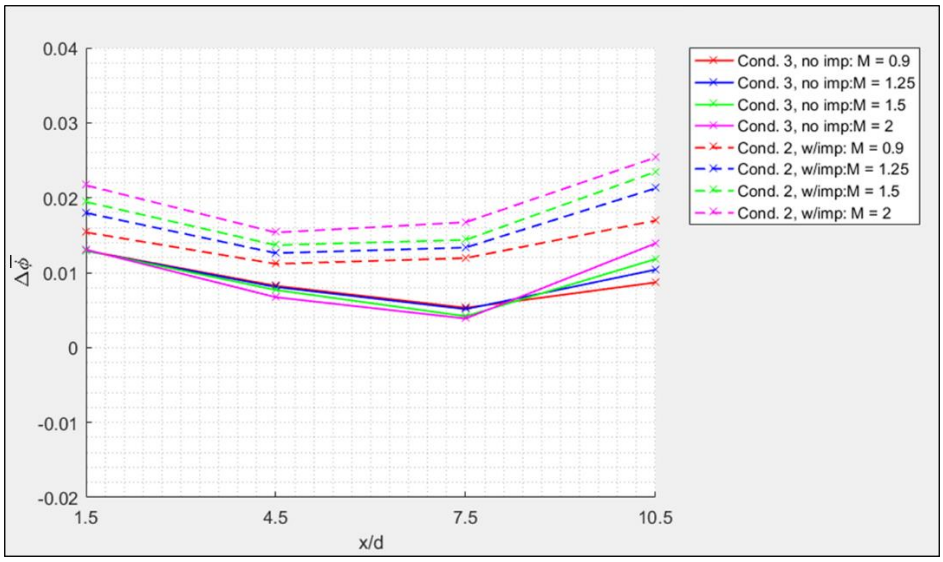

Figure 73. Spanwise-averaged $\Delta\phi$: $\overline{\phi}_{\text{[high Re, low T, empty, Sec. 2]}} - \overline{\phi}_{\text{[high Re, low T, empty, Sec. 1]}}$ (solid) and $\overline{\phi}_{\text{[low Re, high T, w/imp., Sec. 2]}} - \overline{\phi}_{\text{[low Re, high T, w/imp., Sec. 1]}}$ (dashed).

Next, the streamwise lines were used to determine the distribution was periodic. For this investigation, Condition 4 (Re = 15,000, T_∞ = 450 K) was interrogated as it experienced the largest $\Delta\phi$ between lines. The solid lines represent the $\Delta\phi$ between lines 1 and 2 shown in Figure 74, while the dashed lines represent the $\Delta\phi$ between lines 2 and 3. The data lines

are colored by blowing ratio. Overall, the difference in effectiveness between lines 2 and 3 was near zero indicating that the flow had fully developed spanwise. The peak $\Delta\phi$'s between Lines 2 and 3 occurred near the stagnation with a value around 0.021. Therefore, data in subsequent analyses will be pulled from Line 3 and the Section 2 spanwise lines.

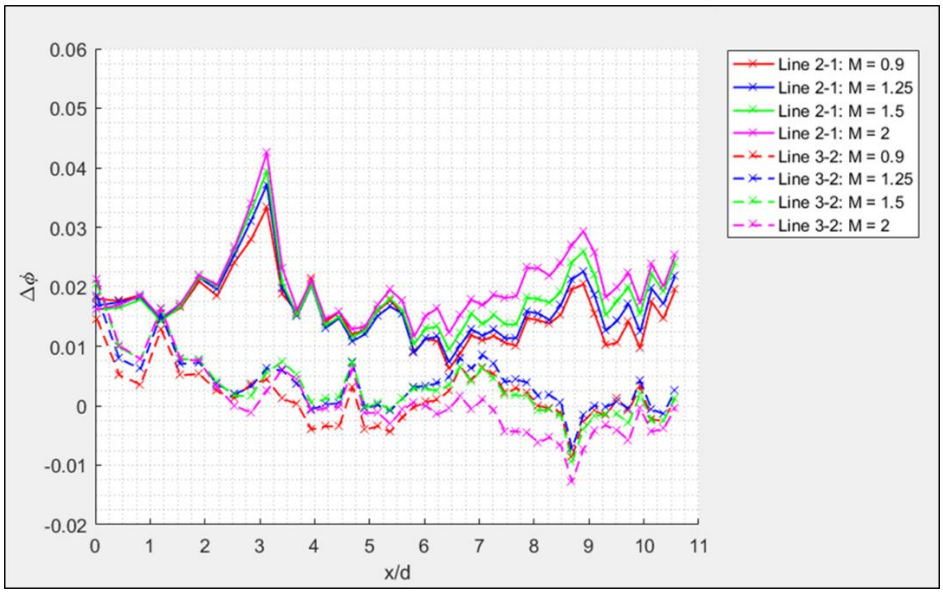

Figure 74. Streamwise $\Delta\phi$: $\phi_{[\text{high Re, high T, line 2}]} - \phi_{[\text{high Re, high T, line 1}]}$ (solid) and $\phi_{[\text{high Re, high T, line 3}]} - \phi_{[\text{high Re, high T, line 2}]}$ (dashed).

4.2.1. Overview of Small Scale Investigations

As explained in the Chapter 1, an objective of this thesis was to continue investigating the impact that nondimensional parameters have on scaling overall effectiveness. Additionally, the other objective of matching the configuration of the large scale rig also made for an interesting investigation of how the internal cooling configuration impacts the overall effectiveness. First, the overall effectiveness results produced by tests conducted with matched nondimensional parameters, including the Reynolds number, the blowing ratio, and the density ratio, will be compared. For these tests, the freestream temperature varied between 400 K and 450 K while matching the nondimensional parameters. As all the nondimensional parameters were matched, it was expected that the results from both

temperature regimes would match. Second, effectiveness data produced in the same temperature regime while varying only the Reynolds number will be compared. For these tests, the Reynolds number was varied from 10,000 to 15,000 while matching *DR* and several *M's*. *Nu* is a function of *Re*, *Pr*, and geometry; therefore, when *Re* changes, so too should *Nu*. By testing on the same geometry at the same freestream temperature, which means that the thermal conductivity of the freestream is the same, changing *Nu* should result in a different convective heat transfer coefficient. Therefore, it was expected that tests conducted with all nondimensional parameters matched except the *Re* would produce different effectiveness distributions. The tests performed will help determine the impact that changing *Re* has on the overall effectiveness. Finally, the results from the different internal configurations will be compared. As discussed previously, the impingement plate should increase internal cooling which is expected to improve the overall cooling. However, Bryant's [11] results showed that the addition of an impingement plate decreased overall effectiveness for most of the surface.

4.2.2. Matched nondimensional parameters

As discussed previously, the goal of scaling effectiveness results is to enable acquisition of measurements in safer and lower temperature environments and use those results to predict, with a high degree of accuracy, what the effectiveness results should be in a higher temperature environment. The following analysis was conducted to understand how well matching the Re_∞, *DR*, and *M* enables matching of the effectiveness produced at different temperature regimes. Figure 75 shows the difference in effectiveness produced by tests conducted with freestream temperatures of 400 K and 450 K while matching the

nondimensional parameters. A freestream Reynolds number of 10,000, a blowing ratio of 0.9, and a density ratio of 1.1 were targeted for each test. The figure shows that most of the data are bound between $\Delta\phi$'s of 0 and 0.01 which means that the data changed only a small amount between the two tests and is within the calculated uncertainty.

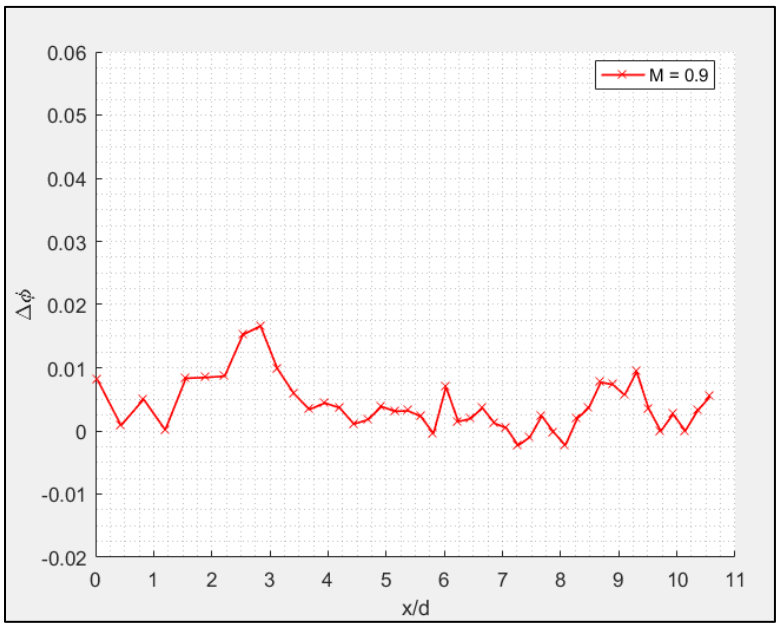

Figure 75. Streamwise $\Delta\phi$: $\phi_{[\text{low Re, high T}]}$ - $\phi_{[\text{low Re, low T}]}$ at M =0.9.

To further investigate how the overall effectiveness is impacted, Figure 76 shows the $\Delta\phi$ between Conditions 1 (Re = 10k, T_∞ = 400 K) and 2 (Re = 10k, T_∞ = 450 K) for additional blowing ratios. These results show similar trends to one another including spikes that occur at x/d locations of 3, 6, and 9 which are the locations of the coolant holes. The magnitude of the $\Delta\phi$'s of the three additional M cases show further increased effectiveness compared to the M = 0.9 case. The grouping of the $\Delta\phi$ lines does not reveal any obvious trend that relates M to $\Delta\phi$. However, looking at the data, the DR was equal to 1.093 for M = 0.9 at Condition 1 (Re = 10k, T_∞ = 400 K) and was lower than the target DR of 1.1 experienced for the other cases. This was attributed to a higher coolant temperature (366.1 K vs 363.6K).

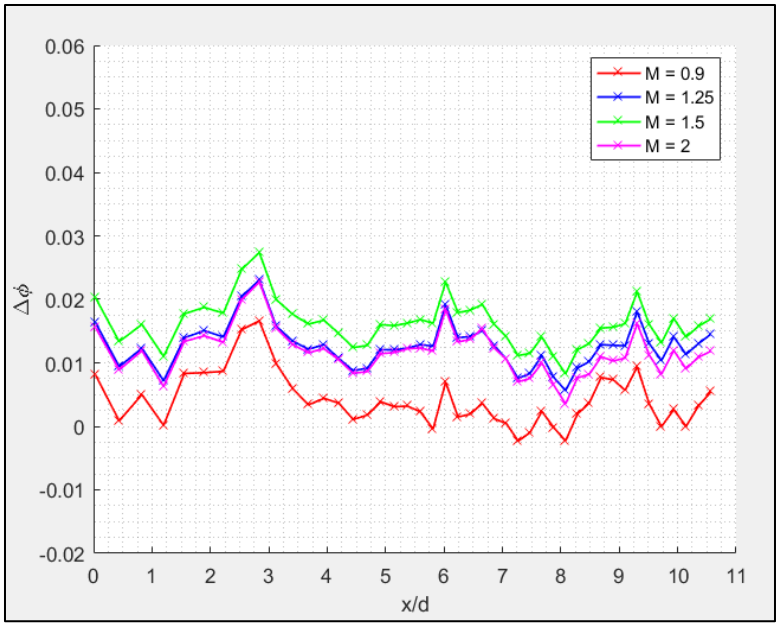

Figure 76. Streamwise $\Delta\phi$: $\phi_{\text{[low Re, high T]}}$ - $\phi_{\text{[low Re, low T]}}$.

Since the *M* = 0.9 test point for Condition 1 was used for the repeatability analysis and collected every day of testing, there was an opportunity to see if a better matched *DR* test point would cause the grouping to tighten. Figure 77 shows the repeatability results discussed in Section 3.5. Of this data, it was discovered that two tests better matched the *DR* with *DR*s of 1.095 each; though, they still did not achieve the target *DR* due to the coolant heating issue discussed earlier. These additional results were similarly compared against the Condition 2 data and plotted with the previous data in Figure 78. The new line produced from the results obtained on 5 January did not improve the line grouping but instead increased the spacing from the other data lines; however, the line produced from the results obtained on 29 December appeared to collapse the data and improve the grouping. Examining the test data further, both the 29 December test and the 5 January test appeared to use freestream temperatures of 400 K and coolant temperatures of about 365 K. Their Reynolds numbers

and blowing ratios were similarly matched making it difficult to determine the reason for the overall effectiveness discrepancies.

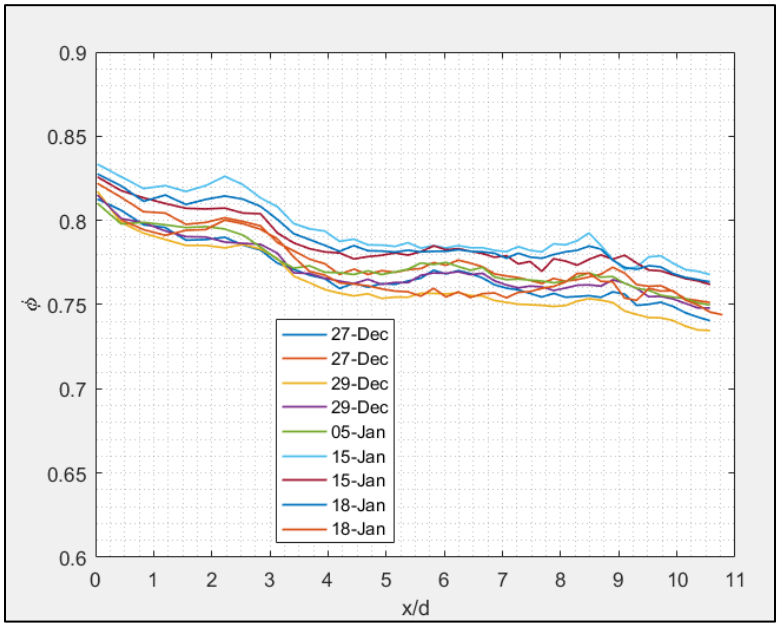

Figure 77. Streamwise ϕ: $\phi_{[\text{low Re, low T}]}$, M = 0.9 for tests from 27 Dec through 18 Jan.

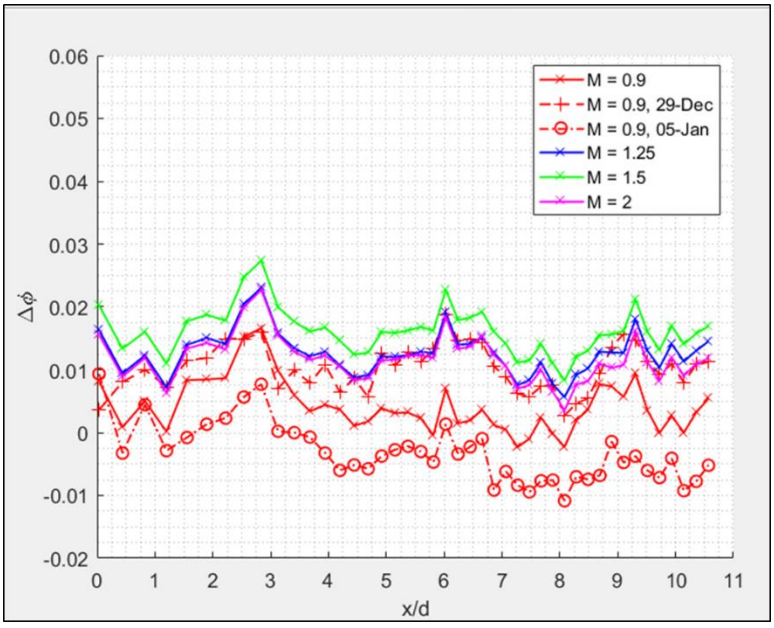

Figure 78. Streamwise $\Delta\phi$: $\phi_{[\text{low Re, high T}]}$ - $\phi_{[\text{low Re, low T}]}$ with additional M = 0.9s from 29 Dec & 5-Jan.

Figure 79 shows the difference in effectiveness produced for the higher *Re* (15,000) tests. Like with the previous comparison, the data shows small variations between the two

temperature regimes where higher effectiveness occurred at the higher freestream temperature. Though, the data for this comparison appears to be on average higher than the results for the lower *Re*. The only other noticeable difference was that the curve for $M = 0.9$ changed position with respect to the grouping of the other lines compared to the previous figure. Due to the apparent issues with the previous $M = 0.9$ cases, it is difficult to draw any conclusion from this comparison; however, the *DR*s did match better for these tests possibly indicating that the trend seen in Figure 79 was correct. For these tests, the *DR*'s were all within 0.002 of 1.1.

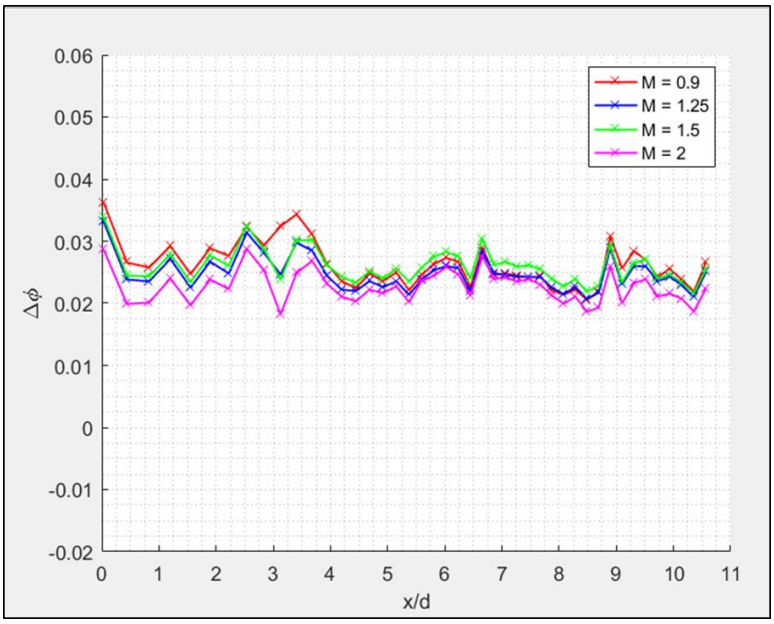

Figure 79. Streamwise $\Delta\phi$: $\phi_{[\text{high Re, high T}]} - \phi_{[\text{high Re, low T}]}$.

To attempt to gain more insight into the reason for the increased $\Delta\phi$'s, observed between higher *Re* tests, Figure 80 and

Figure **81** show the ϕ distributions on the model's surface at all Conditions for the single blowing ratio case of $M = 2$. In the region where the data is pulled, which is from around y/d = 15.2, the cooling pattern appears very similar for all results. In the low *Re* tests,

the overall effectiveness results are on average higher than those of the high *Re* tests. However, no noticeable shift in the cooling pattern was evident.

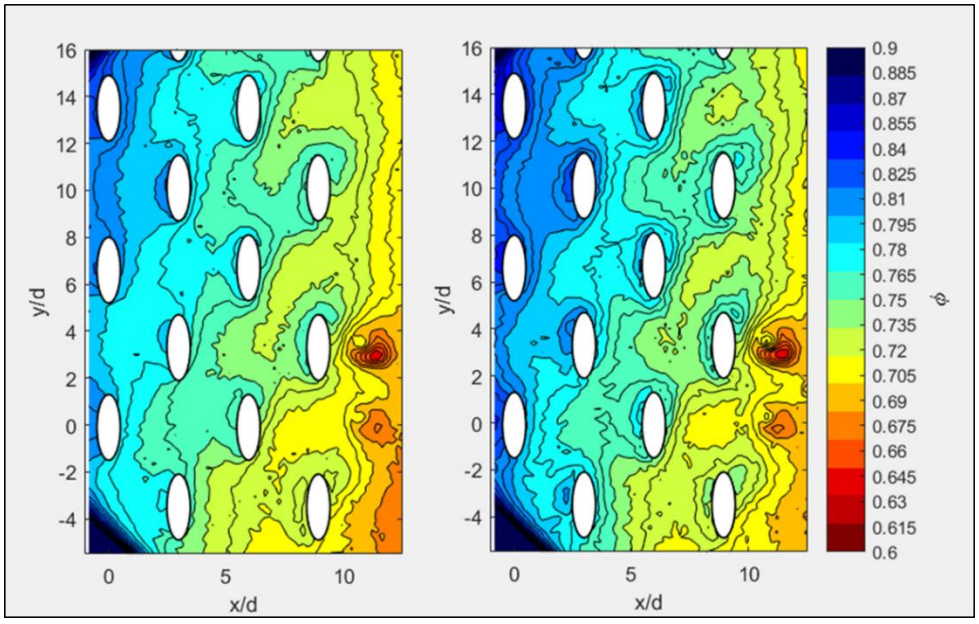

Figure 80. ϕ distribution: $\phi_{[\text{low Re, low T}]}$ (left) and $\phi_{[\text{low Re, high T}]}$ (right) for M = 2.

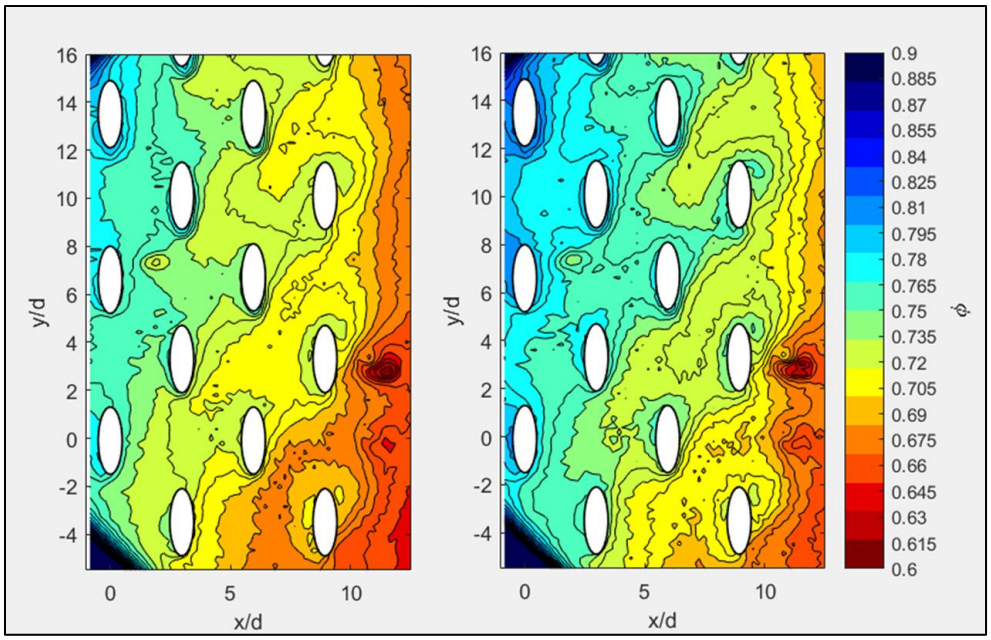

Figure 81. ϕ distribution: $\phi_{[\text{high Re, low T}]}$ (left) and $\phi_{[\text{high Re, high T}]}$ (right) for M = 2.

Figure 82 revisits the overall effectiveness results obtained at Condition 2 (low *Re*, high T_∞). In addition to testing conducted with the standard blowing ratios, two more blowing ratios were used during Condition 2 testing: M = 0.5 and M = 0.7. Comparing the results, all tests showed the same overall decrease in effectiveness with increasing streamwise distance. A trend of increased effectiveness with increased blowing ratio also seemed to be present with the exception of the M = 0.5 case. Reviewing the test data, the M = 0.5 case appeared to have experienced substantial coolant warming. The coolant temperature measured was 414 K which was about 5 K greater than the target coolant temperature. This resulted in a *DR* of 1.087 for this test point while the rest of the test points achieved *DR*'s of 1.1. This further highlights the importance of matching the *DR*. Examining the thermocouple ahead in the coolant delivery block also experienced warming which is more indicative of the coolant warming through the coolant block rather than coolant ingestion. Figure 83 shows the ϕ distribution for the M = 0.5 and 0.7 cases. The results do not show signs of ingestion.

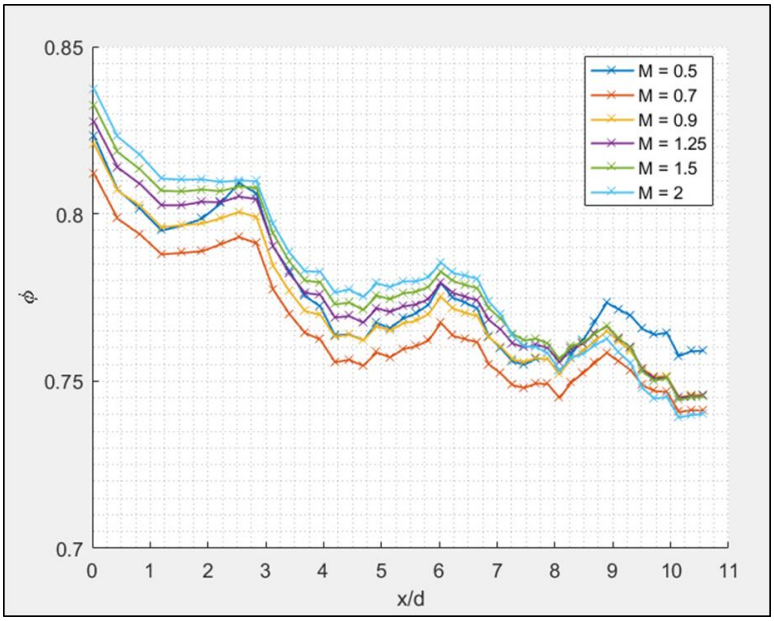

Figure 82. Streamwise ϕ: $\phi_{[\text{low Re, high T}]}$ with additional blowing ratios.

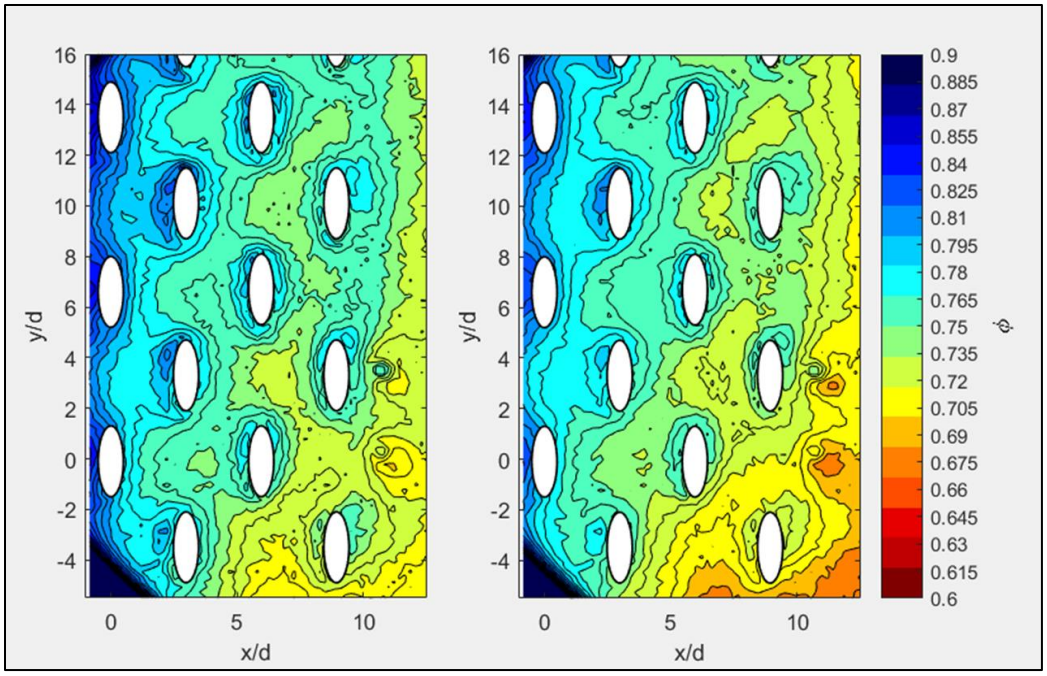

Figure 83. ϕ: Low *Re*, high *T* for *M* = 0.5 (left) and *M* = 0.7 (right).

Both low and high *Re* cases show good agreement between the different temperature regimes. As a scaling experiment, this is encouraging to see. Another observed trend was that the higher *Re* cases showed slightly higher $\Delta\phi$*'s* between the temperature regimes. Because *Re* is most related to flow effects, this trend may indicate that the flowfield setup by the higher *Re* is slightly different than the flowfield of the lower *Re* case. However, the flowfield through the test section has yet to be characterized so this hypothesis cannot be verified. Another thing to consider is that matching the coolant Reynolds number and the freestream Reynolds number at two different temperatures is impossible due to the nonlinear temperature dependence of air's fluid properties. For the low freestream Reynolds number cases, the maximum percent difference in the coolant Reynolds number was about 0.4% for the *M* = 0.9 case. For the high freestream Reynolds number cases, the maximum percent decrease in the coolant Reynolds number was about 0.5% for *M* = 0.9 case. Since the results

for both Reynolds numbers were matched fairly well, it was difficult to determine the reason for the slightly elevated $\Delta\phi$'s for the high freestream Reynolds number comparison.

4.2.3. Impact of Reynolds Number

To better understand the impact of varying *Re*, this investigation compared data from experiments that matched all parameters except the Reynolds number. Figure 84 shows the difference in effectiveness produced by tests run at a freestream temperature of 400 K, a *DR* of 1.1, and various *M's* while varying the *Re* between 10,000 and 15,000. The lines are colored by varying blowing ratios with there being two cases of $M = 0.9$. As was done in the previous section, the best matched *DR* case for $M = 0.9$ from the repeatability analysis was used to aid in this comparison and was drawn with the dashed line. The data shows an overall decline in effectiveness with higher *Re*. On average, the overall effectiveness data between the two Reynolds numbers varied by about 0.035. An additional trend observed was that most of the data was tightly packed except for the $M = 0.9$ cases. The original *DR* showed an average offset of about 0.02 from the other data while the better matched *DR* data moved slightly closer to the rest of the data. This result appears to indicate that the spacing of the $M = 0.9$ data can be partially attributed to the mismatch of *DR*.

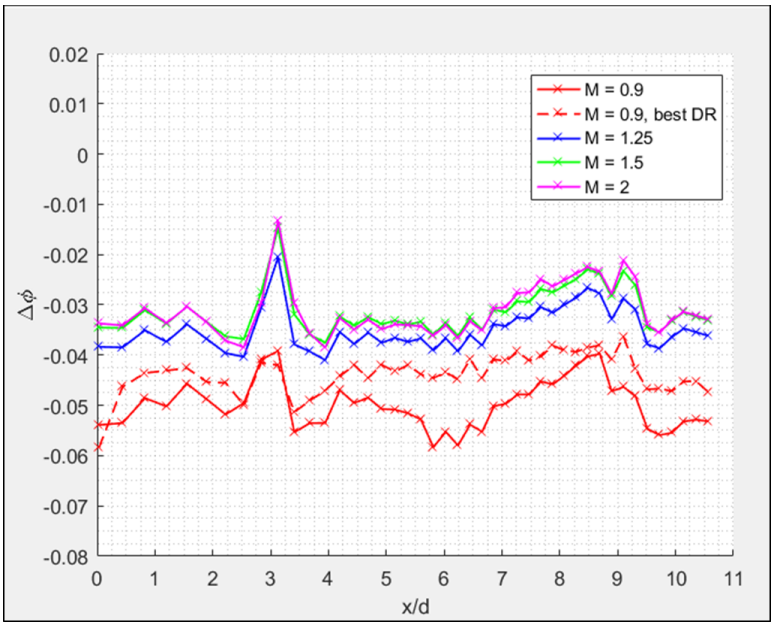

Figure 84. Streamwise $\Delta\phi$: $\phi_{[\text{high Re, low T}]} - \phi_{[\text{low Re, low T}]}$.

Figure 85 shows the difference in effectiveness produced by tests run at the high freestream temperature (450 K), the same *DR*, and the same *M's* while, again, varying the *Re* between 10,000 and 15,000. The lines are colored by varying blowing ratios. The data again showed an overall decline in effectiveness for the higher *Re* tests with the $\Delta\phi$ averaging around -0.02. The $\Delta\phi$ magnitudes for this comparison were slightly smaller than those of the lower temperature tests possibly indicating that the effect of Reynolds number is reduced with increased temperature. The data for this comparison was grouped tighter than in the previous comparison. Examining the test data revealed that the *DR*'s for all of these test points were well matched and might be the reason for the closer grouping of the data.

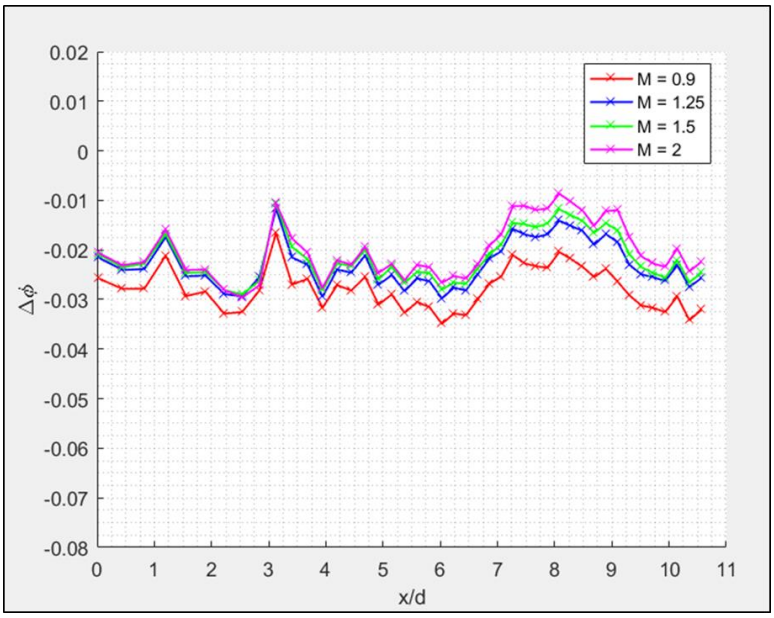

Figure 85. Streamwise $\Delta\phi$: $\phi_{[\text{high Re, high T}]} - \phi_{[\text{low Re, high T}]}$.

The data showed that the overall effectiveness was negatively impacted by increasing the Reynolds number in both temperature regimes. Similar Reynolds number effects were observed in the work performed by Chandran and Prasad [28] as discussed in Chapter 2. This trend was expected based on their results; however, the reduction in $\Delta\phi$ from the low temperature results to the high temperature results was unexpected. For this examination, increasing the freestream Reynolds number by 50% from 10,000 to 15,000 while matching the blowing ratios resulted in corresponding 50% increases in the coolant Reynolds numbers. Since the Nusselt number is typically a function of the Reynolds number, as well as the Prandtl number, it is expected that both the internal and external Nusselt numbers would change by the same amount between conditions using different freestream Reynolds numbers. Finally, because these tests were conducted with matched *DR* and freestream temperatures, the internal and external heat transfer coefficients would also be expected to change by the same amount as the Nusselt numbers. Therefore, it is difficult to justify the reduction in the $\Delta\phi$'s between the two different temperature regimes.

4.2.4. Effect of internal cooling configuration

As discussed in Chapter 2, component designers have a number of ways to augment the cooling inside of a component. To examine how internal cooling affected the overall effectiveness of her model, Bryant [11] varied backside internal cooling by using several different impingement plates with various hole and slot configurations. This work attempted a similar, more limited examination. Two internal cooling configurations were used: with an impingement plate and without an impingement plate. The design of the plate is detailed in Section 3.2.2. This examination compares the results obtained at all four conditions using both internal cooling configurations.

In the previous examination without the impingement plate present, two thermocouples were used to inform the temperature of the internal coolant. With the impingement in place, the thermocouples were placed on either side of the impingement plate as shown in Figure 86. In the coolant warming discussion of Section 4.1, it was shown that the temperatures measured in the empty plenum were always very close, usually within a degree of each other. With the impingement plate installed, the temperatures in the coolant plenum would vary around 4 K because of the thermocouples' positioning on either side of the plate. To understand the effect of using one temperature measurement location versus the other, multiple tests were conducted at the same freestream and coolant flow conditions except that the "coolant temperature" was set by one thermocouple measurement or the other. For example, a test was conducted at Re = 10,000, T_∞ = 400 K, M = 0.9, and DR = 1.1 where the $T_{c,1}$ measurement was used to set the DR. Another test was run using the same conditions except that $T_{c,2}$ set the DR. Figure 86 compares the results measured using the different thermocouple locations at different blowing ratios. Overall, the results showed that setting

the *DR* with $T_{c,1}$ resulted in lower overall effectiveness compared to the results produced by setting the *DR* with $T_{c,2}$. On average, the effectiveness results differed by around 0.052. Since the definition of ϕ requires the use of the coolant temperature at the coolant hole inlet, $T_{c,2}$ was the proper value to use. However, this study stressed the importance of capturing the change in temperature across the impingement plate for setting the coolant temperature. Failure to monitor this change can significantly impact the results. For further analysis, $T_{c,2}$ was used to set *DR*.

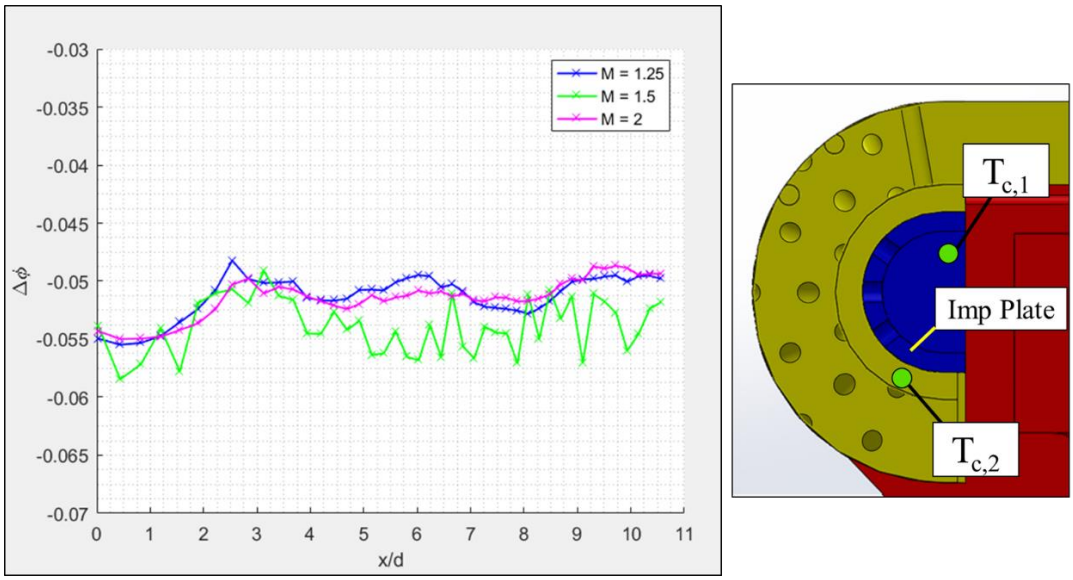

Figure 86. Streamwise $\Delta\phi$: $\phi_{[\text{low Re, low T, w/imp, } Tc2]}$ - $\phi_{[\text{low Re, low T, w/imp, } Tc1]}$ (left) and position of TC measurements (right).

Figure 87 shows overall effectiveness results for both internal configuration cases run at Condition 1 (*Re* = 10k, T_∞ = 400 K) and *M* = 0.9. A qualitative comparison can be made between the two frames which suggest that the impingement plate has increased effectiveness for most of the region observed. This is especially noticed in the area surrounding coolant hole Rows 3 and 4. Figure 88 shows the location of the impingement jets in relation to the coolant hole exits on the model's surface. The impingement holes are colored blue while the coolant hole exits are colored red. The green ellipse indicates the

region of the leading observed by the IR camera. While there does not appear to be any "cooler" spots that form due to internal impingement, the surface displays a much more uniform overall effectiveness distribution.

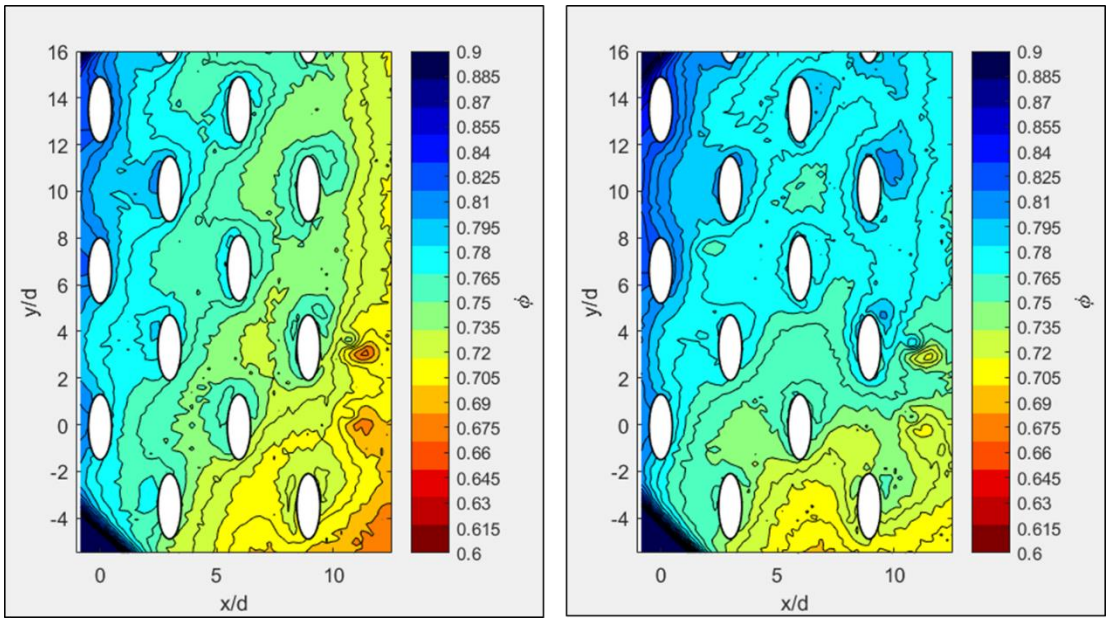

Figure 87. ϕ: Low *Re*, Low *T*, *M* = 0.9 without (left) and with (right) impingement plate

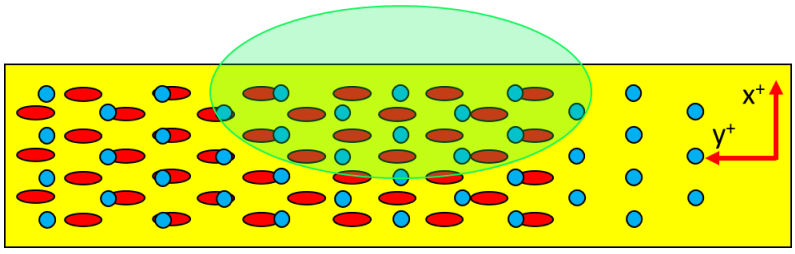

Figure 88. Impingement hole and coolant hole exit alignment.

Figure 89 shows the impact of the impingement plate at Condition 1 (*Re* = 10k, T_∞ = 400 K) while varying blowing ratios. The figure shows that there was an overall improvement when using the impingement plate. The bulk of the improvement is shown downstream of the row of holes at *y/d* = 3. Varying *M* appeared to have a small effect on the results but the *M* = 0.9 cases again indicate the mismatched *DR*'s are an issue. To understand if a trend exists for *M*, Figure 90 shows the spanwise averaged data were as a function

blowing ratio for the Condition 1 (Re = 10k, T_∞ = 400 K) results. The plot lines are colored by x/d position indicating which vertical data line is being examined. The solid lines indicate that the data was taken with the impingement plate while the dashed lines indicate that the data was collected without the impingement plate present. Both sets of lines indicate that the averaged overall effectiveness is relatively insensitive to blowing ratio as shown by the flat profile of each line. Instead, the presence of the impingement plate appears to be the driver of the increased effectiveness as evidenced by the large spacing between the solid and dashed lines of the same color. The tight spacing of the solid lines indicate that smaller temperature gradients existed on the plate when the impingement plate was used.

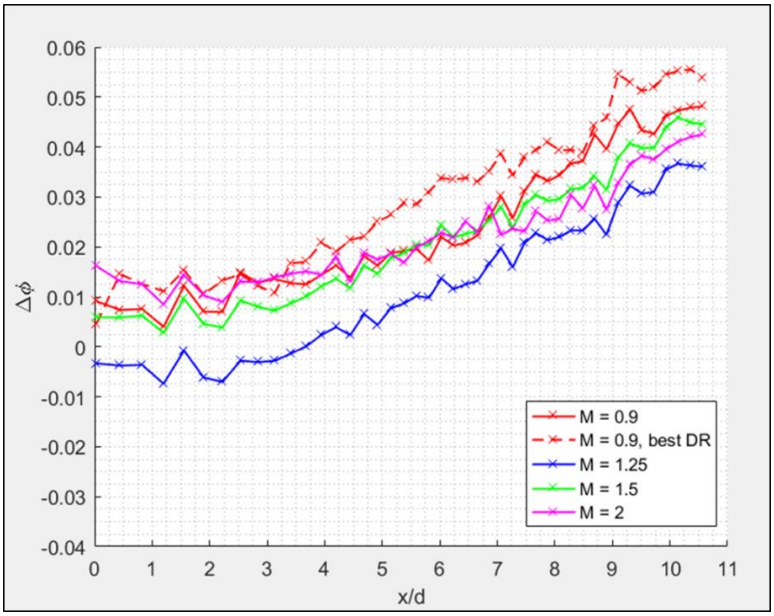

Figure 89. Streamwise $\Delta\phi$: $\phi_{[\text{low Re, low T, w/imp}]}$ - $\phi_{[\text{low Re, low T, empty}]}$.

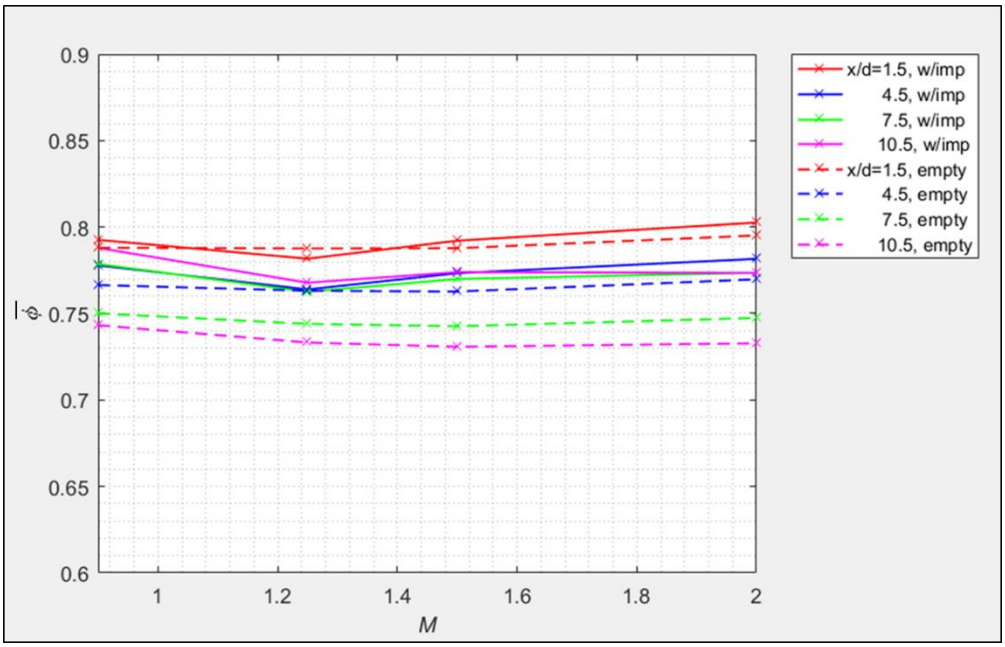

Figure 90. Spanwise averaged ϕ: $\phi_{[\text{low Re, low T, w/imp}]}$ (solid), $\phi_{[\text{low Re, low T, empty}]}$ (dashed).

Figure 91 shows the effect of the impingement plate at Condition 2 (Re = 10k, T_∞ = 450 K) while varying blowing ratios. These results show good agreement with the results from Condition 1 (Re = 10k, T_∞ = 400 K). The overall effectiveness improves in the streamwise direction with little variation between the different cases of M. A new development, however, were the large dips observed near x/d = 2.5. This same feature showed up in subsequent results but the reason was unknown. Figure 92 was created to investigate what the effectiveness was doing at that location and to determine if this feature was of any concern. The data plotted came from Condition 2 and M = 0.9 using the different internal cooling configurations. Examining the data in the location of the dip, the data did not appear to behave strangely. In fact, both data lines exhibited the same trend of creating small peaks along the length of the data. It is believed that the internal cooling at this location is just similar between the two internal configurations.

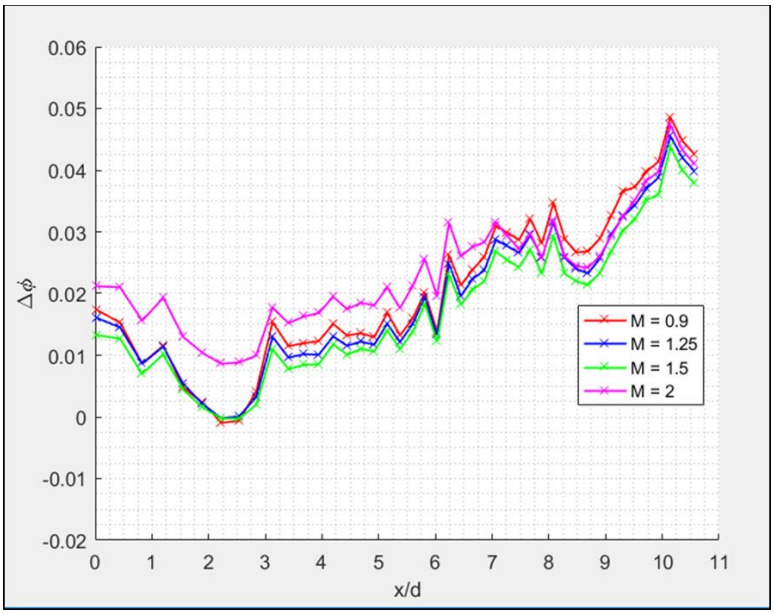

Figure 91. Streamwise $\Delta\phi$: $\phi_{\text{[low Re, high T, w/imp]}} - \phi_{\text{[low Re, high T, empty]}}$.

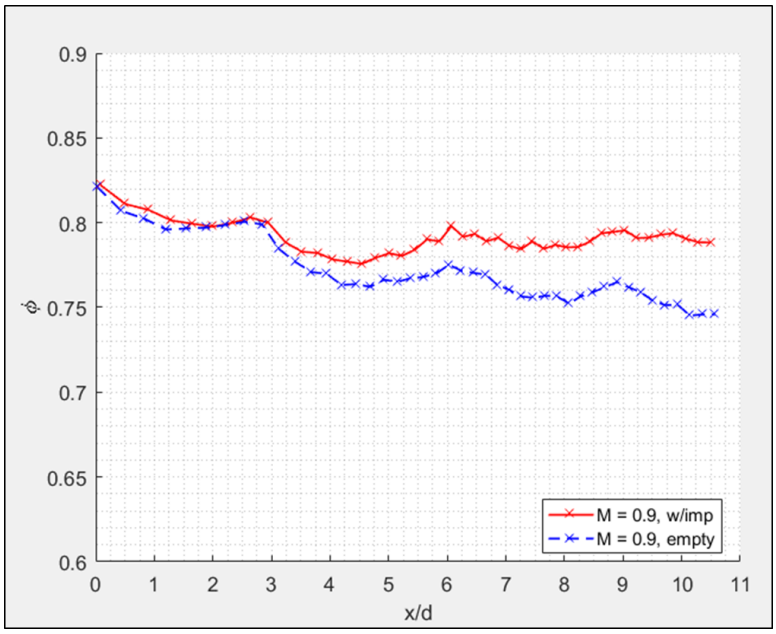

Figure 92. Streamwise ϕ: $\phi_{\text{[low Re, high T, w/imp]}}$ (solid), $\phi_{\text{[low Re, high T, empty]}}$ (dashed).

Figure 93 also showed improvement in effectiveness for Condition 3 (Re = 15k, T_∞ = 400 K) when using the impingement plate. The same trend of improvement downstream of the row of holes at x/d = 3 was shown. Again, varying M appeared to have an effect on the results; however, the M = 0.9 case appeared to be affected by some issue. Looking into

the data, the case with the impingement plate installed appeared to only achieve a *DR* of 1.093. Figure 94 shows the results from the tests run at Condition 4 (*Re* = 15k, T_∞ = 450 K). The results show good agreement with the previous results. The most noticeable difference is the tightness of the plotted lines. They are essentially line on until near the end and indicate low dependence on *M* for these conditions.

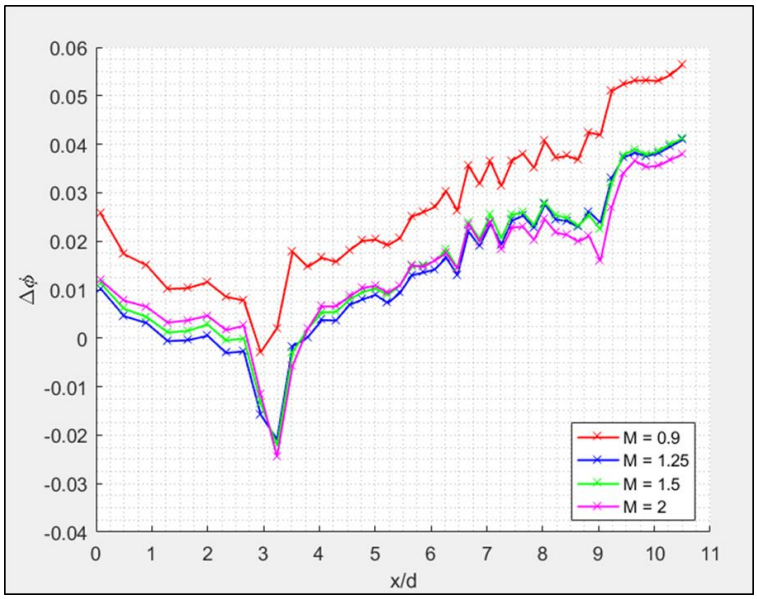

Figure 93. Streamwise $\Delta\phi$: $\phi_{\text{[high Re, low T, w/imp]}}$ - $\phi_{\text{[high Re, low T, empty]}}$.

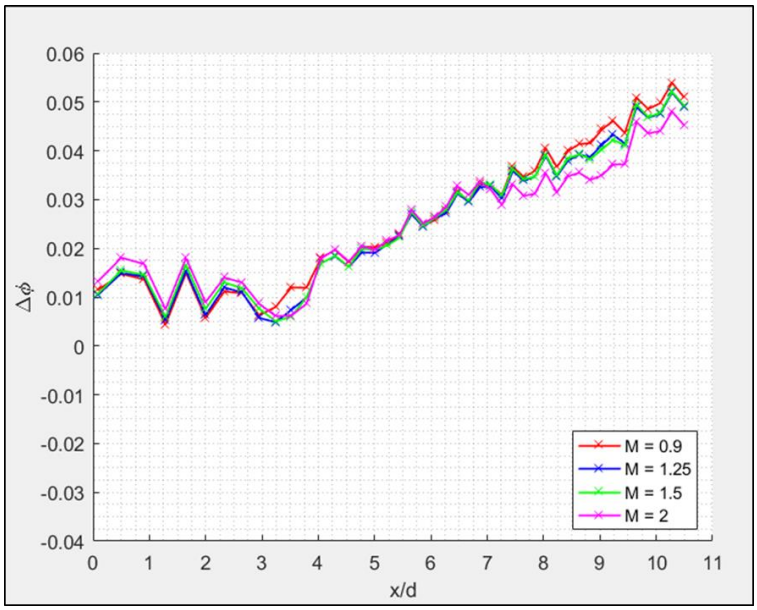

Figure 94. Streamwise $\Delta\phi$: $\phi_{\text{[high Re, high T, w/imp]}}$ - $\phi_{\text{[high Re, high T, empty]}}$.

In general, the results of this investigation showed that there was an overall improvement in effectiveness with increased downstream distance while using the impingement plate over the empty plenum cases. At times, there were indications that the blowing ratio affected the effectiveness. However, the trends varied greatly between all the conditions making it difficult to conclude a *M* trend. Further interrogating the did reveal that not matching the *DR* for some tests may have complicated matters further. The spanwise averaged results also indicated that *M* may not have been as important to the outcome of the results compared to the internal configuration. Overall, these results do not appear to follow any trends observed in the data presented by Bryant [11] which is likely due to the incongruities with the experimental setup, including different impingement hole spacing and the method of delivery coolant.

4.3. Thermal Scaling Investigation

In their investigation, Stewart and Dyson [3] performed a mathematical exercise showing that matching the Biot and Nusselt numbers for a scaled experiment to engine conditions, assuming the same geometry and Reynolds number, relied on matching the ratio of thermal conductivities of the freestream and the wall, as shown in Equation 41. This investigation sought to examine how well the thermal conductivities matched between the best and worst cases of scaled results examined in Section 4.2.2. Based on Stewart and Dyson's assessment, it was believed that thermal conductivities of the best scaled case would best match compared to the worst scaled case.

$$\frac{k_{air,eng}}{k_{wall,eng}} = \frac{k_{air,rig}}{k_{wall,rig}} \tag{41}$$

To begin this investigation, the thermal conductivity of Inconel 718 must be known. The data in Figure 95 was procured from a technical data sheet on Inconel 718 created by the Special Metals Corporation, a company that specializes in metallurgy [47]. The data sheet provided thermal conductivities at even temperature intervals and when plotted produced a linear trend. With these points, a curve fit was applied to produce a relationship between temperature and the thermal conductivity, as shown in Figure 95.

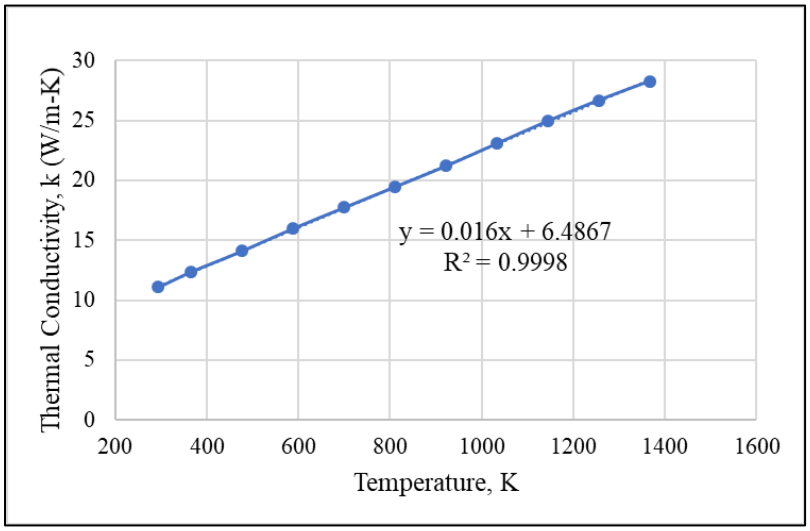

Figure 95. Thermal conductivity of Inconel 718 [47]**.**

From the previous analysis of overall effectiveness in Section 4.2.2, it was determined that the best case of matching occurred between Conditions 1 and 2 for $M = 0.9$; however, since there was clearly an issue with the $M = 0.9$ data for Condition 1, the second best case of matching was used, which was between Conditions 1 and 2 at $M = 2$. The worst case occurred between Conditions 3 and 4 for $M = 0.9$. Figure 96 shows the overall effectiveness results of each test case and how they compare. Using the freestream temperatures and measured metal temperatures, which were used to calculate overall effectiveness in Section 4.2.2, the thermal conductivity ratios of each test were calculated. The resulting thermal conductivity ratios are shown in Figure 97.

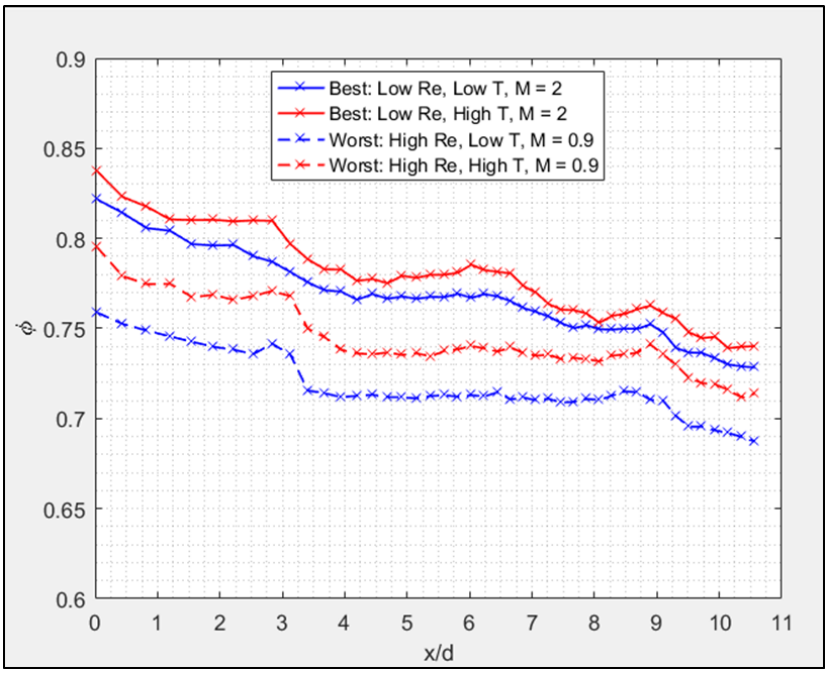

Figure 96. Streamwise ϕ for best and worst cases of thermal scaling.

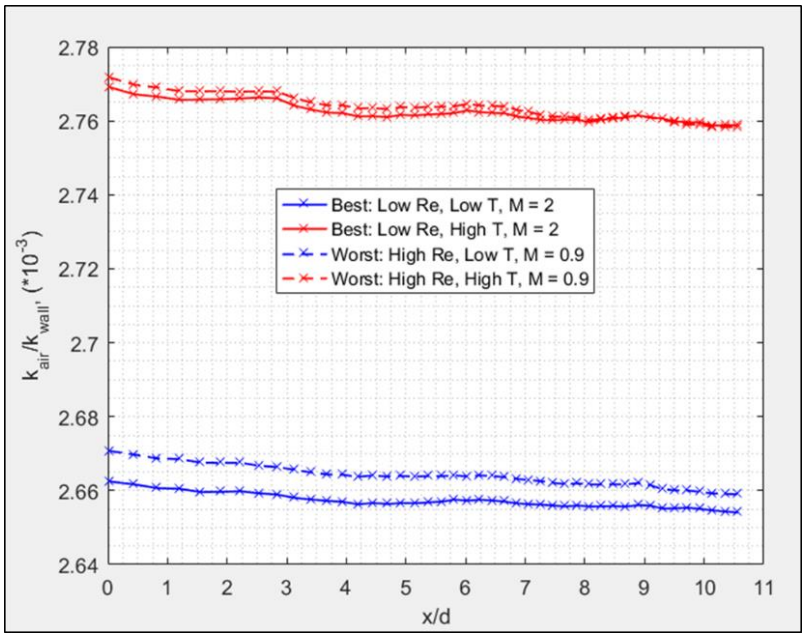

Figure 97. Thermal conductivity ratios for best and worst cases of matching.

For an easier comparison of the results, both the overall effectiveness results and the thermal conductivity ratios were averaged and summarized in Table 10. Comparing the averaged overall effectiveness data, the difference in averaged effectiveness between the Condition 1 and 2 results showed an increase of 0.012 and between the Condition 3 and 4

data showed an increase of 0.026. Comparing the ratio of thermal conductivities between matched cases, the data showed that the thermal conductivity ratio increased about 3.7% from the Condition 1 results to the Condition 2 results. The thermal conductivity ratio also increased about 3.7% from Condition 3 to 4. This outcome was unexpected due to the difference in the $\Delta\bar{\phi}$ results.

Table 10. Thermal scaling results

Comparison	Condition	DR	M	$\bar{\phi}$	$\Delta\bar{\phi}$	$(kair/kinc)_{avg}$	% Change
Best	1	1.1	1.96	0.766		0.00266	
	2	1.1	2.01	0.777	0.012	0.00276	3.7
Worst	3	1.1	0.90	0.716		0.00266	
	4	1.1	0.90	0.742	0.026	0.00276	3.7

These results are hard to interpret because of the small differences. As mentioned, it was expected that the best case of scaling would have had the closer pair of thermal conductivities; however, both comparisons of scaling showed that the thermal conductivity ratio scaled the same amount between the low high temperature results while producing only slightly different $\Delta\bar{\phi}$'s. While it is hard to judge how well the effectiveness results scaled based on the scaling of thermal conductivity ratio, it must be remembered that the overall effectiveness results were already deemed to have scaled well based on the observations made in Section 4.2.2 and that the larger point of Stewart and Dyson's investigation was that Inconel 718 is a good material for matched *Bi* testing. The results of this investigation support the latter point.

5. Conclusions and Recommendations

The objectives of this thesis included redesigning of the FCR to better match AFIT's large scale rig, continue investigating the impact of different nondimensional parameters on the scaling of film cooling effectiveness, and examine the thermal scaling behavior of Inconel 718. To enable a geometric scaling investigation, the experimental setup for the small scale rig was modified, including modifications to the support equipment in addition to the test section changes. With the update FCR, the impact of several nondimensional parameters on the scaling of overall effectiveness was investigated. Additionally, an investigation on the impact of internal cooling on overall effectiveness was also. Finally, a short investigation of the thermal scaling capability of Inconel 718 was conducted to confirm the results shown by Stewart and Dyson [3]. The experiments performed for this thesis were also partially diagnostic in nature while other aspects continued to pursue new lines of inquiry for the AFIT FCR. They provided valuable information about the operating capabilities of the rig considering the large overhaul. The following conclusions discuss the implications of the experimental results. Additionally, modifications made to the rig will be assessed and recommendations for possible future modifications are discussed.

5.1. Geometric Scaling investigation

There are advantages to large scale testing such as increased safety, model manufacturing benefits, and instrumentation advantages. However, there are still concerns with how accurate results produced on a large scale matched Biot number models translate to real component performance. To support future comparisons of data between AFIT's small and large scale rigs, necessary changes were made to the small scale rig to better match

the experimental setup of the large scale rig. This included the integration of a $1/9^{th}$ scaled version of the semi-cylinder leading edge model used by the large scale rig, which forced a redesign of the test section and the updating of the lab support equipment. Despite the changes made to the small scale rig, it was determined that conditions used in previous large scale work could not be achieved. This was shown through a detailed analysis of how the testing flow rates and temperatures were determined. Therefore, a compromise was reached where the large scale rig conducted tests at conditions that the small scale could reach. A qualitative analysis of results produced by each rig indicated that the small scale rig still did not match the large scale rig. It is believed that the differences in the methods of providing coolant to the leading edge account for the bulk of the differences in the results. Correcting this issue would enable a better comparison that would inform the true impact of geometric size differences.

With the new experimental setup, the location of the stagnation point was unknown. To gain understanding of its whereabouts, an experiment was conducted where the bypass channel exit area was adjusted using the bypass blockage gate to induce a change in the freestream impingement location. Thermal measurements were taken for five different gate positions, including gate positions that resulted in a fully open and a fully closed bypass channel. The $\Delta\phi$ and ϕ distributions were compared with the fully open case serving as the baseline from which the rest of the results were compared. The experiment showed that overall effectiveness changed in response to the bypass exit area changes. It is believed that this occurred because of a combination of surface and coolant temperature changes caused by the different gate positions. However, with the data collected, it was still difficult to determine the exact stagnation location even when comparing the contours of the ϕ

distributions. The technique used during this analysis showed promise for identifying the location of stagnation but requires some improvement including changing the view angle and the use of a smaller blowing ratio to ensure ingestion occurs and can be observed.

5.2. Nondimensional parameter and internal cooling configuration investigation

With the redesigned FCR, work on investigating the relative impact that nondimensional parameters have on overall effectiveness was continued. Additionally, the impact that internal cooling configuration had on overall effectiveness was also investigated. In these experiments, four parameters, the freestream temperature, the coolant temperature, the Reynolds number, and the blowing ratio, were varied so that their effect could be understood. Figure 98 summarizes the $\Delta\phi$ results obtained in different temperature regimes (marked by x's), using different Reynolds numbers (marked by +'s), and using different internal cooling configurations (marked by o's) for four different blowing ratios. For the figure, the Condition 1 (low *Re*, low T_∞) results without the impingement plate served as the baseline.

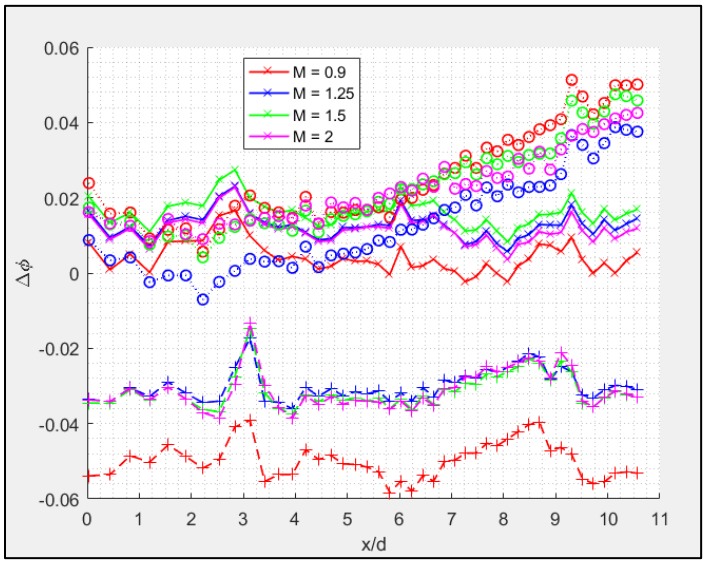

Figure 98. Combined results of the different variations.

The testing accomplished with different freestream temperatures while matching *DR*, *Re*, and *M* yielded results that were very close to one another as evidenced by their small *Δϕ's*. Since these were scaling tests, it was encouraging to see these results. An additional trend observed was that the higher *Re* cases showed slightly higher *Δϕ's* between the temperature regimes. It was initially believed that the coolant Reynolds number changes might contribute to the higher Δϕ's for the high Reynolds number tests, but it was found that the coolant Reynolds number changed by similar percentages for both comparisons. Ultimately, the reason for this trend was not discovered.

The comparisons made with tests conducted at different *Re* while matching *DR*, T_∞, and *M* confirmed that the overall effectiveness is affected by the *Re,* as was previously believed based on the work of Chandran and Prasad [28]. Despite matching *DR* and *M*'s, the results of the high *Re* cases were consistently lower than the low *Re* cases. It was found that a 50% increase in *Re* caused ϕ to drop by about 0.035 for the low temperature tests and by about 0.02 for the high temperature tests.

Finally, tests were conducted using different internal cooling configurations to determine that the internal cooling configuration has on overall effectiveness. In general, the results showed that overall effectiveness improved over the majority of the surface. For the data examined, overall effectiveness improved by an average of 0.022 due to the use of an impingement plate; but most interestingly, the resulting surface temperature distribution was fairly uniform in the region observed. Uniformity is a desired trait because it reduces thermal stresses due to temperature gradients. An additional trend observed, though it is currently not understood, was that the higher temperature tests saw the influence of the blowing ratio

reduced. This effect could be related to a change in another nondimensional parameter that was unaccounted for in this investigation. It was also noted that the results and trend in this data did not match well with the results of Bryant [11], which indicated that the impingement plate had a negligible effect on the overall effectiveness.

5.3. Thermal Scaling Investigation

This investigation, based on the thermal scaling work performed by Stewart and Dyson [46], attempted to examine the efficacy of using the ratio of thermal conductivities to predict if the Biot numbers and Nusselt numbers were matched for scaled tests. The assumption going into this investigation was that closer matched thermal conductivity ratios between low temperature and high temperature tests would correspond to better scaled overall effectiveness results. Using the scaled data produced in the matched nondimensional parameter investigation, the ratio of thermal conductivities of the best and worst scaled tests, determined by the $\Delta\phi$'s observed, were compared. Despite the best and worst scaled tests producing $\Delta\phi$'s of 0.012 and 0.026, respectively, the ratio of thermal changed by the same percentage from low to high temperature tests for each comparison. These results were difficult to interpret, especially given that uncertainty in the results was significant and much larger than differences that were trying to be resolved. Despite not seeing the trend expected, the fact that maximum difference between results was only 0.026 is believed to support Stewart and Dyson's main point, which was that Inconel 718 is a good material to use for scaled testing.

5.4. FCR Future Improvements

A large part of this effort was dedicated towards modifying the test setup of AFIT's small scale rig to enable comparisons of results garnered from both the large and small scale rigs. This section discusses future modifications needed to improve results and capability. The changes recommended cover instrumentation and technique updates.

As discussed previously, the coolant temperature uncertainty is a larger driver in the overall effectiveness uncertainty. To gain more confidence in the trends that are observed with the FCR, the coolant temperature uncertainty needs to be reduced. Some obstacles to this are finding a measurement method that can be integrated into the current data measurement infrastructure and keeping the form factor down. It is recommended a more accurate measurement instrument be obtained. This could be accomplished by calibrating the thermocouples currently used or by procuring a totally new, more accurate temperature measurement device.

Previous research also noted that the coolant temperature was affected greatly by the mass flow rate and was confirmed in this investigation. The coolant temperature rise experienced for the lower coolant mass flow rates made it difficult to test at higher density ratios with low blowing ratios. For this investigation, a *DR* of 1.1 was nearly attainable at all conditions tested with a few exceptions. The maximum coolant warming observed was around 85 K. Additional work should be done to reduce the heating of coolant as it passes through the coolant block to improve the ability to set higher density ratios. Vorgert [34] improved heating issues in his rig configuration by building an air gap between the main block and the test block. A similar solution might be employed in the future. One component to consider for modification is the transition wedge. Creating a void on the wall closest to

the coolant block could create a similar air gap and reduce heat transfer from the main block. Another potential solution is to separate the coolant inlet channel by removing material in the base of the forward coolant block around inlet and creating an air gap. This solution would also reduce the heat transfer but has potential mechanical and manufacturing problems. The mechanical issue would be a reduction in strength of the coolant channel that could led catastrophic failure. Very likely this could be mitigated by filling in the gap with a material that is less thermal conductive but adds some strength to the cantilever design of the coolant channel inlet. Alternatively, the coolant block could be redesigned with a different point of entry to reduce the distance that the coolant has to travel through the block. An idea would to be bring coolant from the side of the rig. A redesign of this kind could require additional modifications to adjoining components.

A final recommendation related to the coolant flow is to determine the flow requirements early. A potential issue forecasted with using a 600 K freestream was that the coolant flow rate required to match the higher blowing ratios, exceeded the capability of the mass flow controller used in these experiments. This would have required switching out the mass flow controller with another that could control a larger range of coolant flows. The COAL lab has mass flow controllers with larger ranges. The drawback to using them is that their reported uncertainty is higher than the one currently used.

The next two recommendations are related to the freestream flow. The first recommendation is to finish installing the new electric heaters. It is believed that they could reduce the testing work load and time while increasing the freestream temperature limits and stability. The electric heaters used in this investigation were simple to operate but did not give users fine control over the heat produced and, coupled with the fact that they were

located far upstream, made the task of staying on condition difficult. The new heater setup has an automated mode of operation that adjusts the heater power settings and are located closer to the rig. In this new setup, it is believed that the test section freestream temperature will be more easily controlled and stable. The other recommended change is to reintroduce a pressure measurement capability. Previous investigations were able to collect pressures from the test section, but over the years of testing, the capability had eroded. Making pressure measurements above and below the model could further inform experimenters how the flow field is setup and could aid in setting of the stagnation.

Another recommendation is to investigate the environmental impact on the thermal measurements. As discussed in Section 3.3.2, an investigation of the effect of the density ratio was hampered by an apparent thermal measurement issue experienced during testing. It was believed that the external rig temperature had a larger effect on the intensities observed, especially when varying the density ratio. A future study would attach a thermocouple to the viewport housing to track the outer wall rig temperatures throughout testing. This data could then be used investigate if and how this environmental factor impacts the thermal measurements.

Though the results of the large and small scale rigs did not match up well, it was believed that the main driver for the differences was an unmatched coolant delivery method. It is believed that modifying the small scale rig's coolant delivery block to better emulate Bryant's soaker hose design would improve the ability to compare data from both rig's in support of providing a better understanding of the geometric scaling effects. An additional goal would be to establish where the freestream impinges so that similar freestream conditions could be confirmed between the two rigs. It is believed that a better view of the

leading edge could improve the ability to observe the effect of the bypass adjustor which would improve the ability to set the stagnation. To obtain a better view, a new viewport window would need to be made lower than the one used in the present study. An additional benefit of shifting the window lower is that the view of the fourth thermocouple would be improved. Its inclusion in the IR calibration is expected to improve calibration accuracy.

The final recommendation is to install the double-sided heat flux gauges. This would enable the determination of local Biot numbers and local heat transfer coefficients which would further improve understanding of the data collected in the FCR. This could also enhance another thermal scaling investigation of Inconel 718 by providing actual *Bi* values.

References

[1] Bogard, D. G., and Thole, K. A., 2006, "Gas Turbine Film Cooling," *J. Propuls. Power,* **22**(2), pp. 249–270.

[2] Trimble, S., 2013, "Pratt & Whitney Raises Temperature as It Accelerates Growth Strategy for F135," Flight Int.

[3] Stewart, W. R., and Dyson, T. E., 2017, "Conjugate Heat Transfer Scaling For Inconel 718," *ASME Turbo Expo 2017*, ASME, Charlotte, NC, USA, GT2017-64873.

[4] Lawson, S. A., Straub, D. L., Beer, S., Casleton, K. H., and Sidwell, T., 2013, "Direct Measurements of Overall Effectiveness and Heat Flux on a Film Cooled Test Article at High Temperatures and Pressures," *ASME Turbo Expo 2013,* ASME, San Antonio, Texas, USA, GT2013-94685.

[5] Han, J. C., Dutta, S., and Ekkad, S. V., 2000, *Gas Turbine Heat Transfer and Cooling Technology*, Taylor & Francis, New York.

[6] Nathan, M. L., Dyson, T. E., Bogard, D. G., and Bradshaw, S. D., 2014, "Adiabatic and Overall Effectiveness for the Showerhead Film Cooling of a Turbine Vane," *J. Turbomach.*, **136**(3), pp. 310051–310059.

[7] Dees, J. E., Bogard, D. G., Ledezma, G. A., Laskowski, G. M., and Tolpadi, A. K., 2012, "Experimental Measurements and Computational Predictions for an Internally Cooled Simulated Turbine Vane," *J. Turbomach.*, **134**(6), pp. 61003–61009.

[8] Ekkad, S. V, Han, J. C., and Du, H., 1998, "Detailed Film Cooling Measurements on a Cylindrical Leading Edge Model: Effect of Free-Stream Turbulence and Coolant Density," *J. Turbomach.*, **120**(4), pp. 799–807.

[9] Williams, R. P., Dyson, T. E., Bogard, D. G., and Bradshaw, S. D., 2013, "Sensitivity of the Overall Effectiveness to Film Cooling and Internal Cooling on a Turbine Vane Suction Side," *J. Turbomach.*, **136**(3), pp. 31006-31006–7.

[10] Rutledge, J. L., Polanka, M. D., and Bogard, D. G., 2016, "The Delta Phi Method of Evaluating Overall Film Cooling Performance," *J. Turbomach.*, **138**(July), pp. 1–8.

[11] Bryant, C. E., 2017, "Relative Contributions to Overall Effectiveness in Gas Turbine Cooling," Master's Thesis, Air Force Institute of Technology, WPAFB, OH, AFIT-ENY-MS-17-M-248.

[12] Polanka, M. D., Rutledge, J. L., Bogard, D. G., and Anthony, R. J., 2017, "Determination of Cooling Parameters for a High-Speed, True-Scale, Metallic Turbine Vane," *J. Turbomach.*, **139**(1), pp. 11001–11009.

[13] Bergman, T. L., Lavine, A. S., and Incropera, F. P., 2011, *Fundamentals of Heat and Mass Transfer, 7th Edition*, John Wiley & Sons, Incorporated.

[14] Sweeney, P. C., and Rhodes, J. F., 1999, "An Infrared Technique for Evaluating Turbine Airfoil Cooling Designs," *J. Turbomach.*, **122**(1), pp. 170–177.

[15] Reagle, C. J., 2009, "Heat Transfer Measurements Using Thin Film Gauges and Infrared Thermography on a Film Cooled Transonic Vane," Master's Thesis,Virginia Polytechnic Institute and State University.

[16] Ashby, R. W., 2016, "Scaling Film Cooling Performance From Ambient To Near Engine," Master's Thesis, Air Force Institute of Technology, WPAFB, OH, AFIT-ENY-MS-16-D-036.

[17] Rutledge, J. L., and Polanka, M. D., 2014, "Computational Fluid Dynamics Evaluations of Unconventional Film Cooling Scaling Parameters on a Simulated

Turbine Blade Leading Edge," *J. Turbomach.*, **136**(10), pp. 101006–101009.

[18] Greiner, N. J., Polanka, M. D., Rutledge, J. L., and Shewhart, A. T., 2015, "Experimental Investigation of Net Heat Flux Reduction at Combustion Temperatures," *ASME Turbo Expo 2015*, ASME, Montreal Canada, GT2015-42988.

[19] Polanka, M. D., 1999, "Detailed Film Cooling Effectiveness and Three Component Velocity Field Measurements on a First Stage Turbine Vane Subject to High Freestream Turbulence," Ph.D. Dissertation, University of Texas at Austin.

[20] Greiner, N. J., Polanka, M. D., and Rutledge, J. L., 2015, "Scaling of Film Cooling Performance From Ambient to Engine Temperatures," *J. Turbomach.*, **137**(July), pp. 1–11.

[21] Eberly, M. K., and Thole, K. A., 2013, "Time-Resolved Film-Cooling Flows At High And Low Density Ratios," *ASME Turbo Expo 2013*, ASME, San Antonio, Texas, USA, GT2013-95031.

[22] Saumweber, C., Schulz, A., and Wittig, S., 2003, "Free-Stream Turbulence Effects on Film Cooling With Shaped Holes," *J. Turbomach.*, **125**(1), pp. 65–73.

[23] Gritsch, M., Schulz, A., and Wittig, S., 1998, "Adiabatic Wall Effectiveness Measurements of Film-Cooling Holes With Expanded Exits," *J. Turbomach.*, **120**(3), pp. 549–556.

[24] Gau, C., and Chung, C. M., 1991, "Surface Curvature Effect on Slot-Air-Jet Impingement Cooling Flow and Heat Transfer Process," *J. Heat Transfer*, **113**(4), pp. 858–864.

[25] Mayle, R. E., Blair, M. F., and Kopper, F. C., 1979, "Turbulent Boundary Layer Heat Transfer on Curved Surfaces," *J. Heat Transfer*, **101**(3), pp. 521–525.

[26] Ravelli, S., Dobrowolski, L., and Bogard, D. G., 2010, “Evaluating the Effects of Internal Impingement Cooling on a Film Cooled Turbine Blade Leading Edge,” *ASME Turbo Expo 2011*, ASME, Glasgow, UK, GT2010-23002.

[27] Mouzon, B. D., Terrell, E. J., Albert, J. E., and Bogard, D. G., 2005, “Net Heat Flux Reduction and Overall Effectiveness for a Turbine Blade Leading Edge,” *ASME Turbo Expo 2005*, ASME, Reno, Nevada, USA, GT2005-69002.

[28] Chandran, D., and Prasad, B., 2014, “Conjugate Heat Transfer Study of Combined Impingement and Showerhead Film Cooling Near NGV Leading Edge,” *Int. J. Rotating Mach.*, **2015**, pp. 1–13.

[29] Bohn, D. E., Becker, V. J., and Kusterer, K. A., 1999, “3-D Internal Flow and Conjugate Calculations of A Convective Cooled Turbine Blade with Serpentine-Shaped and Ribbed Channels,” *1999 International Gas Turbine & Aeroengine Congress & Exhibition*, ASME, Indianapolis, Indiana, USA, 99-GT-220.

[30] Omega®, 2017, “Thermocouples” [Online]. Available: https://www.omega.com/prodinfo/thermocouples.html. [Accessed: 20-Sep-2017].

[31] Ekkad, S. V., Ou, S., and Rivir, R. B., 2004, “A Transient Infrared Thermography Method for Simultaneous Film Cooling Effectiveness and Heat Transfer Coefficient Measurements From a Single Test,” *J. Turbomach.*, **126**(4), pp. 597–603.

[32] Martiny, M., Schiele, R., Gritsch, M., Schulz, A., and Wittig, S., 1996, “In Situ Calibration for Quantitative Infrared Thermography,” *3rd QIRT Conference*, Stuttgart, Germany, pp. 3–8.

[33] Ochs, M., Horbach, T., Schulz, a., Koch, R., and Bauer, H.-J., 2009, “A Novel Calibration Method for an Infrared Thermography System Applied to Heat Transfer

Experiments," *Meas. Sci. Technol.*, **20**(7), p. 75103.

[34] Vorgert, C. J., 2017, "Relating Film Cooling Performance Between Ambient and Near Engine Temperatures," Master's Thesis, Air Force Institute of Technology, WPAFB, OH, AFIT-ENY-MS-17-M-298.

[35] Jones, T. V, 1995, "The Thin Film Heat Transfer Gauge - a History and New Developments," *4th National UK Heat Transfer Conf., Manchester*, IMechE, pp. 1–12.

[36] Piccini, E., Guo, S., and Jones, T., 2000, "The Development of a New Direct-Heat-Flux- Gauge for Heat-Transfer Facilities," *Meas. Sci. Technol.*, **11**(4), pp. 342–349.

[37] Anthony, R. J., Clark, J. P., Kennedy, S. W., Finnegan, J. M., Johnson, D., Hendershot, J., and Downs, J., 2011, "Flexible Non-Intrusive Heat Flux Instrumentation On the AFRL Research Turbine," *ASME 2011 Turbo Expo*, ASME, Vancouver, Canada, GT2011-46853.

[38] Popp, O., Smith, D. E., Bubb, J. V, Iii, H. C. G., Diller, T. E., Schetz, J. a, and Ng, W. F., 2000, "Investigation of Heat Transfer in a Film Cooled Transonic Turbine Cascade , Part II: Unsteady Heat Transfer," *ASME Turbo Expo 2000*, ASME, Munich, Germany, 2000-GT-0203.

[39] Shewhart, A. T., 2014, "Minimization of the Effects of Secondary Reactions on Turbine Film Cooling in a Fuel Rich Environment," Master's Thesis, Air Force Institute of Technology, WPAFB, OH, AFIT-ENY-14-J-37.

[40] Damele, C. J., 2013, "Operational Characteristics of an Ultra Compact Combustor," Master's Thesis, Air Force Institute of Technology, WPAFB, OH, AFIT-ENY-14-M-13.

[41] Anderson, W. S., 2007, “Design, Construction, and Validation of the AFIT Small Scale Combustion Facility and Sectional Model of the Ultra-Compact Combustor,” Master’s Thesis, Air Force Institute of Technology, WPAFB, OH, AFIT/GAE/ENY/07-M01.

[42] Osram Sylvania, 2017, “Threaded Inline Heaters,” p. 2 [Online]. Available: https://www.gobigchief.com/pdf/heaters/Datasheet_Inline.94ccf796-6c64-498a-8b19-7cb120dc92bf.pdf.

[43] Lynch, A. J., 2015, “Overall Effectiveness Measurements at Engine Temperatures with Reactive Film Cooling and Surface Curvature,” Master’s Thesis, Air Force Institute of Technology, WPAFB, OH, AFIT-ENY-MS-15-M-244.

[44] Wiese, C. J., 2016, “Influence of Coolant Flow Rate Parameters in Scaling Gas Turbine Cooling Effectiveness,” Master’s Thesis, Air Force Institute of Technology, WPAFB, OH, AFIT-ENY-MS-16-M-245.

[45] Moffat, R. J., 1988, “Describing the Uncertainties in Experimental Results,” *Exp. Therm. Fluid Sci.*, **1**(1), pp. 3–17.

[46] Dyson, T. E., Bogard, D. G., Piggush, J. D., and Kohli, A., 2013, “Overall Effectiveness for a Film Cooled Turbine Blade Leading Edge With Varying Hole Pitch,” *J. Turbomach.*, **135**(3), pp. 31011–31018.

[47] Special Metals, 2007, “Inconel ® Alloy 718,” Publ. Number SMC-045, p. 28 [Online]. Available: http://www.specialmetals.com/assets/smc/documents/inconel_alloy_718.pdf. [Accessed: 08-Feb-2018].

REPORT DOCUMENTATION PAGE

Form Approved
OMB No. 074-0188

1. REPORT DATE *(DD-MM-YYYY)*	**2. REPORT TYPE**	**3. DATES COVERED** *(From – To)*
22-03-2018	Master's Thesis	March 2017 – March 2018

TITLE AND SUBTITLE

Investigation of Geometric and Thermal Scaling Effects on a Simulated Turbine Vane Leading Edge Model

5a. CONTRACT NUMBER

5b. GRANT NUMBER

5c. PROGRAM ELEMENT NUMBER

6. AUTHOR(S)

Tewaheftewa, James G., Captain, USAF

5d. PROJECT NUMBER

5e. TASK NUMBER

5f. WORK UNIT NUMBER

7. PERFORMING ORGANIZATION NAMES(S) AND ADDRESS(S)
Air Force Institute of Technology
Graduate School of Engineering and Management (AFIT/ENY)
2950 Hobson Way, Building 640
WPAFB OH 45433-8865

8. PERFORMING ORGANIZATION REPORT NUMBER

AFIT-ENY-MS-18-M-297

9. SPONSORING/MONITORING AGENCY NAME(S) AND ADDRESS(ES)
Dr. Randall Mathison
The Ohio State University
Gas Turbine Laboratory
Room 158 Aerospace Research Center
2300 West Case Rd., Columbus OH 43235

10. SPONSOR/MONITOR'S ACRONYM(S)

AFRL/RHIQ (example)

11. SPONSOR/MONITOR'S REPORT NUMBER(S)

12. DISTRIBUTION/AVAILABILITY STATEMENT
DISTRUBTION STATEMENT A. APPROVED FOR PUBLIC RELEASE; DISTRIBUTION UNLIMITED.

13. SUPPLEMENTARY NOTES
This material is declared a work of the U.S. Government and is not subject to copyright protection in the United States.

14. ABSTRACT

This thesis explores multiple topics, including the relative importance of nondimensional parameters that relate film cooling performance within different temperature regimes and the effects of different internal cooling configurations on overall film cooling effectiveness. Additionally, the effect on results from geometrically scaled experimental setups was also investigated. Numerous changes were to the FCR were implemented to improve testing performance and to enable the geometric scaling comparisons. An Inconel 718 leading edge model was used to gather thermal measurement data. Four main freestream conditions were used that varied freestream temperature and Reynolds number. Air coolant temperature and mass flow were adjusted to match different film cooling nondimensional parameters. Comparing the results found that effectiveness scaled well between different temperature regimes when the nondimensional parameters matched, increased freestream Reynolds number led to decreased effectiveness, and impingement cooling improved the overall effectiveness distribution.

15. SUBJECT TERMS
Film cooling

16. SECURITY CLASSIFICATION OF:			**17. LIMITATION OF ABSTRACT**	**18. NUMBER OF PAGES**	**19a. NAME OF RESPONSIBLE PERSON**
a. REPORT	**b. ABSTRACT**	**c. THIS PAGE**			Polanka, Marc D., USAF ADVISOR
U	**U**	**U**	**U**	172	**19b. TELEPHONE NUMBER** *(Include area code)* (937) 785-3636, ext 4714 (NOT DSN) (marc.polanka@afit.edu)

Standard Form 298 (Rev. 8-98)
Prescribed by ANSI Std. Z39-18